Università degli Studi di Milano
Università Cattolica del Sacro Cuore
Scuola di Dottorato in
Fisica, Astrofisica e Fisica Applicata

Dipartimento Matematica e Fisica
Dottorato di Ricerca in
Fisica, Astrofisica e Fisica Applicata
Ciclo XXIII

Wavelet transform analysis in thermally excited force spectroscopy

Settore Scientifico Disciplinare FIS/03

Tesi di Dottorato di:
Giovanna Malegori

Coordinatore: Prof. Marco Bersanelli
Tutore: Dott. Gabriele Ferrini

A.A. 2009-2010

Scuola di Dottorato in Fisica,
Astrofisica e Fisica Applicata

Ciclo XXIII

Universitá degli Studi di Milano
Facoltá di Scienze Matematiche, Fisiche e Naturali
Dipartimento di Fisica
Milano (Italy)

Universitá Cattolica del Sacro Cuore
Facoltá di Scienze Matematiche, Fisiche e Naturali
Dipartimento di Matematica e Fisica
Brescia (Italy) - Sede Consorziata

Prof. Marco Bersanelli *Director*
Dott. Gabriele Ferrini *Supervisor*
Prof. Fulvio Parmigiani *Promoter*

malegori@dmf.unicatt.it
http://www.dmf.unicatt.it/elphos

A Massimo, Luca, Stefano e Guido.

Contents

Chapter 1

Introduction

1.1 Overview

The atomic force microscopy is a powerful and versatile technique for atomic and nanometer-scale imaging of a wide variety of surfaces, both biological and non biological. Atomic force microscopy methods have found applications also for metrology and manipulation at the nanometre level. Therefore, the atomic force microscopy is seen as an essential tool for nanotechnology and is regarded as a window into the nano-world.

The principles of the atomic force microscopy relies on detecting the repulsive (hard sphere) or attractive (van der Waals) interaction forces between the atom(s) at the extremity of a sharp tip protruding from a cantilever and the atom(s) at the sample surface. Forces are measured trough the cantilever bending revealed by an optical lever detection system. The quantitative determination of the tip-sample long and short-range interaction forces is of fundamental importance in the characterization of various properties of materials surfaces and physics processes.

Atomic force microscopy has developed into a powerful technique, delivering not only topographical images but providing also sensitive force measurements on the nanometer and atomic scale. The use of the atomic force microscopy in

measuring tip-sample force is commonly referred to as *force spectroscopy*. Many force spectroscopy techniques suitable for nanoscale investigations are based on measuring the dynamical parameters of the cantilever excited at or near its resonant frequency while experiencing the force field of the sample surface. The interactions of the probing tip with the sample surface perturbs the amplitude, frequency, phase or damping of the cantilever oscillation. The measurement of these parameter modifications provides a sensitive estimation of the tip-sample interaction force.

The present work stems from this context and focuses on thermally excited force spectroscopy to probe the surface forces. In particular we introduce a new approach, the wavelet transform, to analyze the temporal traces of the cantilever Brownian motion collected while the tip moves toward the sample surface. The wavelet transform is a time-frequency analysis method which provides localized information in time and frequency domain simultaneously and it is able to characterize the instantaneous spectral content also of rapidly varying signals.

The wavelet transform in thermally excited force spectroscopy is a very promising tool to probe the tip-sample interaction since the analysis applies simultaneously to the flexural and torsional eigenmodes and can be carried out across the jump-to-contact transition without interruption. Force gradients, adhesion forces, elastic response and topography are provided in acquisition times compatible with practical dynamical force spectroscopy imaging.

1.2 Outline

This work is organized as follows: in Chapter 2 we review the background and advances on scanning force microscopy methods by describing the major dynamic atomic force microscopy operating modes and focusing on recent applications in probing the tip-sample interaction to characterize the sample surface. Moreover we draw the perspective of possible developments of dynamic force spectroscopy

measurements toward force imaging.

In Chapter 3 we present a theoretical framework to describe the dynamical response of an excited cantilever to the local environment energy exchanges. The thermally excited Brownian motion of the cantilever tip is connected to the local mechanical compliance via the fluctuation-dissipation theorem. The interaction potential can be reconstructed by the modification of the thermal motion of the cantilever due to the interaction of the tip with the sample forces.

In Chapter 4 we introduce the mathematical framework used to study signal's time and frequency properties, the wavelet transform analysis. The wavelet transform is a time-frequency analysis method which provides localized information in time and frequency domain simultaneously. This is particularly useful to study transitory regimes i.e. signals with a frequency spectrum rapidly changing during the data collection.

The experimental set-up, the data acquisition and the procedure to calibrate the cantilevers spring constant are described in Chapter 5.

In Chapter 6 we reconstruct the tip-sample interaction potential from the thermal motion of the cantilever when the tip experiences surface forces. The analysis is performed in stationary regime by applying three different approaches: frequency shift, Boltzmann distribution of the Brownian motion and thermal mean square displacement methods. Tip mass loading effect on the cantilever elastic behavior are estimated. The main limitation of the stationary regime analysis is that it requires long acquisition time.

We introduce thus an improvement of the experimental conditions and data analysis in order to shorten the acquisition time, the wavelet transform approach (Chapter 7). This analysis is applied to thermally excited force spectroscopy to get insights into fundamental thermodynamical properties of the cantilever Brownian motion. The time-frequency representation shows the viscous dynamics of the cantilever deflection activated by thermal fluctuations and provides a meaningful and intuitive representation of the cantilever dynamics in time and frequency caused by

the tip-sample interaction forces. The forces measurement applies simultaneously to the flexural and torsional eigenmodes, providing information on tip-sample van der Waals interaction, adhesion forces, friction and elastic response of the surface in approximately 100 ms.

Chapter 2

State of the art

Since their invention ([1, 2]) scanning tunneling (STM) and atomic force/scanning force microscopes (AFM) have emerged as powerful and versatile techniques for atomic and nanometer-scale imaging of a wide variety of surface, both biological and non biological [3, 4, 5, 6, 7, 8, 9]. Moreover, AFM methods have found applications also for metrology and manipulation at the nanometre level. In this Chapter, we review the background and advances on scanning force microscopy methods. We describe the major dynamic AFM modes, amplitude modulation atomic force microscopy (AM-AFM) and frequency modulation atomic force microscopy (FM-AFM), emphasizing their common points and their differences in experimental set-ups and operating conditions. Finally, we focus on recent AFM applications in probing the tip-sample interaction in order to characterize the sample surface. Moreover we draw the perspective of possible developments of tip-sample force measurements toward force imaging.

2.1 Introduction

The atomic force/scanning force microscopy (AFM) has been introduced in 1986 by Binnig, Quate and Gerber [2] as a method to study the surfaces on an atomic scale. Since its invention, the AFM has had a major impact on many areas of science and has found applications for imaging, metrology and manipulation at the nanometre level. Indeed the AFM is seen as an essential tool for nanotechnology and is regarded as a window into the nano-world. The principle of the AFM is based on the measurement of the repulsive (hard sphere) or attractive (van der Waals) interaction forces between the atom(s) at the extremity of a sharp tip and the atom(s) at the sample surface.

The AFM can operate in two modes, contact and oscillating modes. In the contact mode, the tip extremity is in contact with the sample and the repulsive force is probed point by point by moving the tip on the sample surface. The user fixes the value of the repulsive force between the tip and the sample which is kept constant during the scan, providing an isoforce image of the surface. In the oscillating mode, the tip oscillates at a high frequency, determined by the cantilever spring constant, and interacts with the surface only at the lower end of each cycle. When the interaction involves atomic repulsion the technique is usually called the tapping mode. The main advantage of this technique, as compared to the contact mode, resides in a marked reduction of the friction forces during scanning.

The atomic force microscopy can also be used for detecting the interaction forces between the outermost atom of a probing tip and the surface atoms in a variety of environments and scales (Dynamic Force Spectroscopy). The interaction of the AFM tip (Fig. 2.1) with the sample due to the various forces between them gives rise to effects that can affect an SPM image and hence the dimensional measurements inferred. Consequently, these interactions have to be investigated and understood if measurement uncertainties have to be improved. Moreover the quantitative determination of forces is of fundamental importance in the charac-

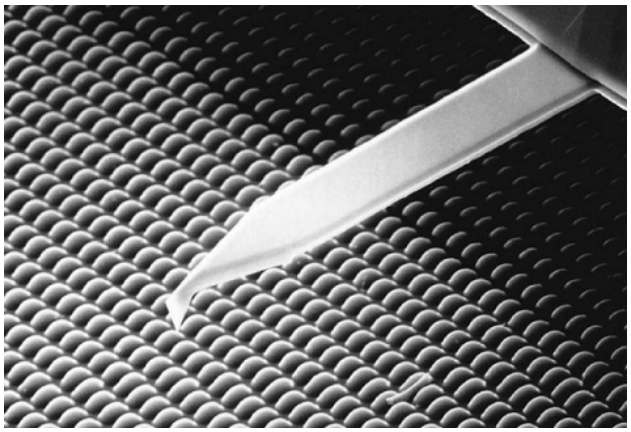

FIGURE 2.1: Scanning electron micrograph of a micromachined silicon cantilever with an integrated tip pointing in the [001] crystal direction.

terization of mechanical processes in nature and mechanical properties of matter.

In the following we presents the principles of the main AFM operating modes and some applications in imaging organic and inorganic samples whereas the final section of the chapter focuses on recent AFM applications in force measurements at the nanoscale and possible improvements of this technique.

2.2 Atomic Force Microscopy

The AFM is a unique multi-purpose microscope whose operating principle is based on both mechanical and atomic interactions. The AFM can be characterized by the following features:

- sensitivity to atomic forces
- ability to examine nearly all surfaces: metals, semiconductors and insulators,
- works in air, liquid or vacuum,
- can measure mechanical response (force-distance curves),
- can be used for mechanical manipulation of single atoms, molecules, polymers and surfaces.

Besides the AFM there are other classes of scanning probe microscopes that are

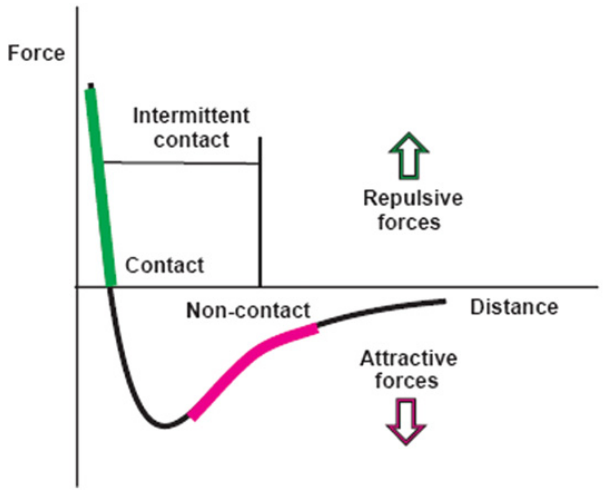

FIGURE 2.2: Schematic diagram showing surface forces as a function of distance and their relation to the modes of AFM operation.

used to measure various properties of surfaces. These include the lateral force microscope, friction force microscope, dielectric spectroscopy, magnetic force microscope and near field scanning optical microscopy.

The AFM relays on detecting the interaction of a probing tip (Fig. 2.1) with the sample surface. Fig. 2.2 shows the force between atoms at the end of an AFM tip and the surface as a function of distance of the tip from the surface. As the sample is approached there is an attractive force (van der Waals) that increases to a maximum before a gradual decrease until the force becomes repulsive (Pauli) [10]. These forces are discussed in more detail in Sec. 3.4. The graph of surface forces also has regions marked as contact, intermittent contact or tapping and non-contact referring to the different modes of operation of the AFM, see Fig. 2.3.

The definition of a tip *coming into contact* with a surface is very difficult when observing physical and other effects on an atomic scale because, in contrast to the macroscopic world, there really is no discrete boundary between the tip and sample. Therefore in the following we prefer to separate AFM modes into static and dynamical categories: the static is referred to in the literature as the contact

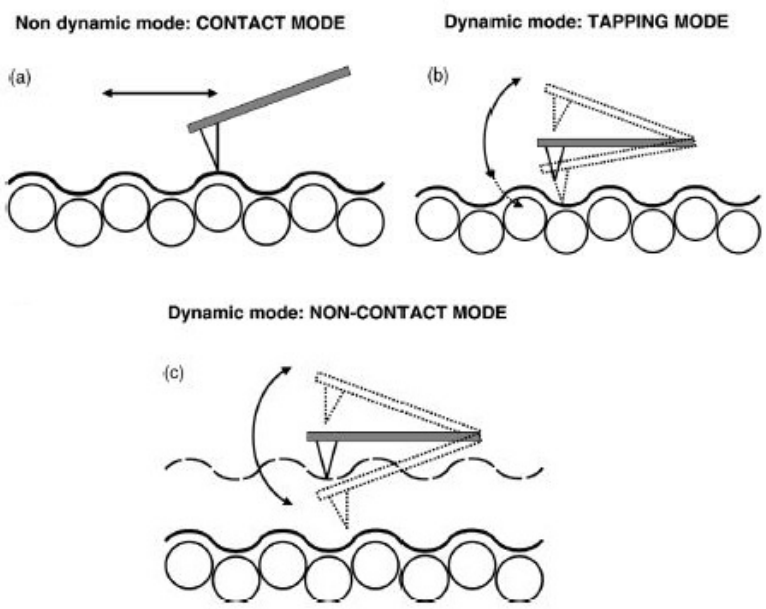

FIGURE 2.3: The most common AFM operation modes. In contact mode (a) the tip is in permanent contact with the sample surface. The shear forces applied to the sample during scanning are significant and potentially damaging the surface especially in case of biological samples. b) The AFM tapping mode uses a tip oscillating. Since the tip is not in contact with the sample during lateral movement in scanning, shear forces applied to the sample by the tip are negligible. c) In non-contact AFM modes, the cantilever tip is placed at the attractive van der Walls force region and force gradients are detected. The force gradient can be detected either from shift in the cantilever resonance frequency or the amplitude and phase of the cantilever oscillation.

mode, the dynamical (AM-AFM and FM-AFM) as the non-contact or tapping mode.

2.3 Static mode

Fig. 2.4 is a schematic diagram showing the major components of a typical scanning force microscope [7]. A very simplistic explanation of the workings of such an

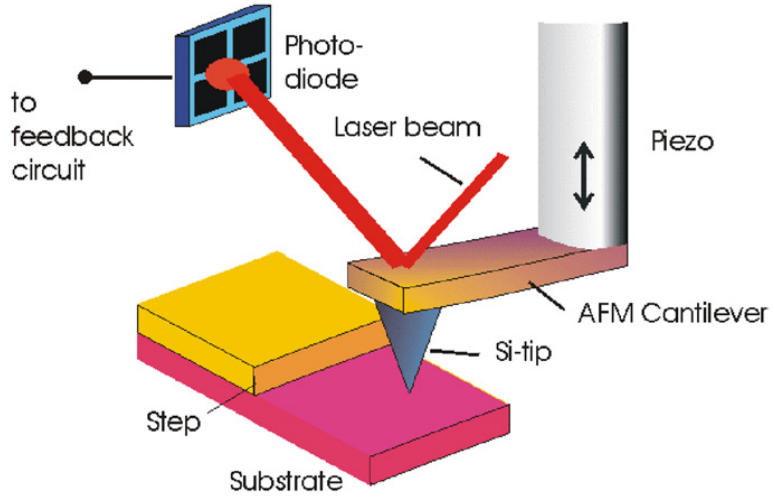

FIGURE 2.4: Schematic diagram showing major components of a scanning force microscope with an optical beam deflection system.

AFM is as follows. A cantilever supports a very fine tip having a typical end radius of a few nanometers that is used as a probe to investigate a sample. The cantilever is attached to a piezoelectric transducer (PZT). Light from a laser diode is reflected from the cantilever onto a quadrant photocell. As the cantilever and tip are scanned over the surface the cantilever bends and the light beam reflected from the cantilever is deviated by the bending, hence its position on the quadrant photocell changes. The signals from the quadrant photocell are used as the input to a servo system that applies a voltage to the PZT to move the cantilever so as to maintain a constant bending of the cantilever and hence return the reflected beams point of incidence on the quadrant photocell to the center. This ensures that the force exerted by the tip on the surface remains constant and that the tip follows the surface. A measure of changes in the servo signal gives an indication of the surface topography.

The cantilever, tip, detection system and servo are at the heart of the AFM and their properties must be carefully controlled in order to achieve optimum vertical and horizontal resolution. The AFM high lateral resolution is achieved by using sharp tips and low forces. Parameters used to describe the tip properties are the

radius of the apex of the tip R_{tip} and the cone angle α.

The displacement or bending of a cantilever z is proportional to the forces acting on it. The factor describing the proportionality is the stiffness or spring constant of the cantilever k. In the contact or static mode of operation the feedback loop controls the displacement or more accurately, the bending of the cantilever and keeps it constant. This means that the deflection $z = F_{ts}/k$ of the cantilever is kept constant. The physical interpretation of the images obtained in static mode as follow: the image is a map $z(x, y,\text{grad}F_{ts} = 0)$ i.e. $z(x, y, F_{ts}=\text{const})$ where F_{ts} is the interaction force between the tip and sample.

It has been demonstrated that the atomic resolution is successfully performed by static AFM, see [8, 9, 7] and references therein. Nevertheless, this operation mode can only be applied in certain cases since it suffers from several drawbacks. Frictional force exerted by the sample on the tip as it sweeps over the sample, may contribute to the topographical image so that surface domain with different frictional properties may appear as topographical features in the image. Moreover the constant downward force of the tip onto the surface is not low enough to avoid certain sample surfaces, including not only biological and most polymer surfaces, but even many seemingly harder materials which are not completely resistant to such damage.

Only the introduction of new techniques based on dynamic force microscopy allows to overcomes many drawbacks of the static-mode.

2.4 Dynamic mode

In this mode the cantilever oscillates above the surface during the scan excited by an actuator that is driven at either the resonant frequency f_0 or close to the cantilever resonant frequency with fixed amplitude A_0. The excitation is in the vertical direction for the non-contact, intermittent or tapping modes or in the horizontal direction for the torsion mode. As the tip interacts with the sample there

is a change in amplitude of oscillation. The cantilever position is controlled by feedback to keep a constant distance between the tip and the sample.

Two main techniques are used to servo control the cantilever: amplitude modulation (AM) and frequency modulation (FM). The AM mode is used very successfully in ambient condition and in liquid as an effective tool for imaging biological specimens. Besides, using the FM mode in vacuum dramatically improved the resolution up to atomic scale.

2.4.1 Amplitude modulation mode

In the AM-AFM (also known as tapping mode), a stiff microlever, which has a sharp tip at its free end, is driven by an oscillation piezo at a fixed frequency, usually near or at the free resonance frequency. The oscillation amplitude is used as a feedback parameter i.e. the position of the cantilever is varied to have a constant amplitude [11]. Indeed the scanning provides an isoamplitude image. In case of homogeneous sample, the interaction and the the oscillation amplitude depends only on the tip-sample distance and the isoamplitude imagine is associated with the surface topography. Additionally, material properties variations could be mapped by recording the phase shift between the driving force and the tip oscillation.

AM or tapping mode uses an oscillating tip (frequency in air 50-500 kHz, in fluids approximately 10 kHz) at a tip amplitude of several nm [3, 6]. In the absence of tip-surface forces $F_{ts} = 0$, the cantilever is well described as a damped harmonic oscillator excited by the sinusoidal oscillation of the piezo actuator [12]. After a transient evolution, the motion is dominated by the steady solution, a sinusoidal function with a phase lag with respect to the excitation force. The dependence of the amplitude on the excitation frequency is calculated by the Lorentzian curve. The oscillation amplitude A depends on the driving force F_0, the hydrodynamic damping and the position of the excitation frequency with respect to the natural

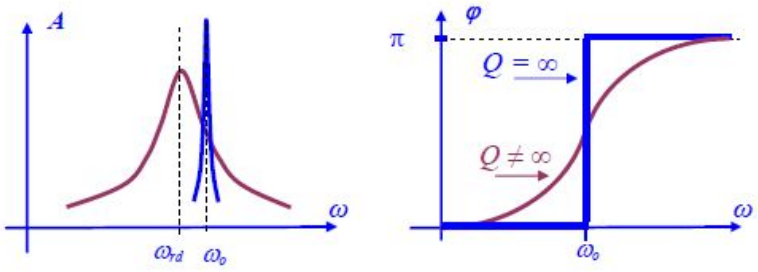

FIGURE 2.5: Change of the amplitude-frequency characteristic and phase response in a system with dissipation. Blue color shows characteristics of non-dissipative system.

frequency (Fig. 2.5).

$$A(\omega) = \frac{F_0/m}{\sqrt{(\omega_0^2 - \omega^2)^2 + (\omega\omega_0/Q)^2}} \tag{2.1}$$

Here m is the effective mass, Q the quality factor.

The resonance frequency ω_r in presence of damping is related to the natural (free resonance) frequency ω_0 by

$$\omega_r = \omega_0\sqrt{1 - \frac{1}{2Q^2}}$$

where Q is the quality factor.

Approaching the surface, the tip interacts with the sample. In case of small tip oscillations, the motion of the tip is described as an harmonic oscillator with a reduced effective resonance frequency depending on the gradient of the interaction $\partial F_{ts}/\partial z$:

$$\omega_0' = \sqrt{\frac{k - (\partial F_{ts}/\partial z)}{m}}$$

where k stands for the cantilever spring constant.

The change in the effective resonance frequency implies a whole shift of the resonance curve where ω_0 is replaced by ω_0'. First, let us assume that the tip is excited at the natural frequency. The approaching of the tip towards the surface will modify the resonance frequency which in turn implies a decrease of the oscillation amplitude to the value of the new resonance curve at the excitation frequency of

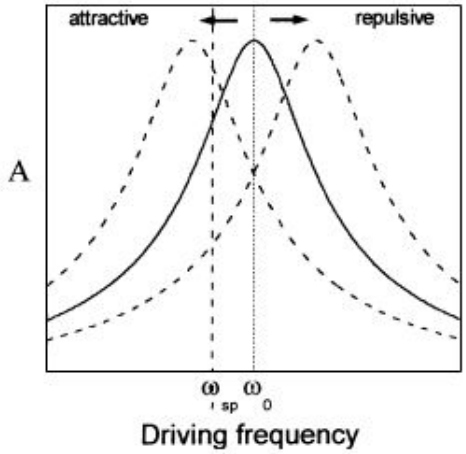

FIGURE 2.6: Free resonance curve (solid line) for the tip, i.e. the harmonic oscillator, and under the influence of attractive and repulsive forces (dashed lines). The force gradient of the external force produces a shift of the resonance curve (weakly perturbed harmonic oscillator model) without introducing any shape or size modifications.

the oscillator, see Fig. 2.6. Instead, if the excitation frequency is just off resonance to the left, the oscillation amplitude could decrease or increase depending on the position of the new resonance frequency with respect to the natural frequency.

If the oscillating tip moves towards the surface, it begins to interact with the surface whereas the tip oscillation amplitude decreases due to the surface interaction. This amplitude reduction is used in the AM-AFM operating mode to identify and measure surface topographic features since the average cantilever deflections are used as an input signal into the feedback loop to keep a constant amplitude oscillation. The piezo-vibrator drives the cantilever oscillations at frequency ω (close to a resonant frequency) and with amplitude A_ω. During scanning the AFM feedback system keeps the oscillations amplitude constant by varying the PZT positions to keep a constant tip-surface separation. The voltage in the feedback loop is recorded as topographic AFM image of the sample.

Phase imaging can be performed at the same time as topographic AM-AFM imaging tapping mode in a single scan [3, 6]. The tip-sample interactions depends

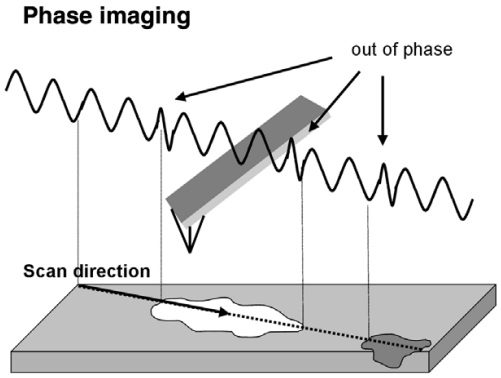

FIGURE 2.7: AFM phase imaging. The variation in materials viscoelasticity lead to different phase lags of the cantilever oscillation which is simultaneously monitored by the AFM control electronics, recorded and transformed into AFM images. AFM phase imaging provides non quantitative information about hardness and elasticity of samples.

not only on the sample topography but also on different sample characteristics as hardness and elasticity or adhesion. In tapping mode, variations of such material properties lead to different phase lags of the cantilever oscillation which is simultaneously monitored by the AFM control electronics, recorded and transformed into AFM images. AFM phase imaging provides non quantitative information about hardness and elasticity of samples. For example, a flat polymer with different stiffness at the surface may be distinguishable in phase mode but not in surface topography image. Phase imaging also acts as a real-time contrast enhancement techniques because it highlights edges.

Approaches to improve spatial and/or compositional resolution by force microscopy have either been focused on the use of higher harmonics to enhance the sensitivity to tip-surface interactions [13, 14]. The multi-modes force microscope is based on the simultaneous excitation of the first two flexural modes of the cantilever. The root mean square amplitude of the first mode is used as the feedback parameter while the phase shift of the second mode is used to obtain compositional maps with very high force sensitivities. The tip-molecule forces generate

higher harmonics of the first mode. Whenever the frequency of a higher harmonic matches or is close to the frequency of the second mode, the modes became coupled. Multifrequency AFM has shown a remarkable enhancement of sensitivity of the microscope to image in a gentle manner and with high spatial resolution a variety of heterogeneous materials.

AM-AFM solves some problems that appears with static AFM but it cannot be extended to UHV. In fact, after perturbing the system (as happens when moving to a new position over the surface during the scan) the change in amplitude in AM mode does not occur instantaneously but the system responds in a transient time scale $\tau_{AM} = 2Q/f_0$ which limits the available bandwidth. Due to high Q factors in vacuum, the AM mode becomes too slow compared to acquisitions times required by imaging. The problem is solved by introducing the FM.

2.4.2 Frequency modulation mode

The FM mode introduced in [15] provided the key to achieve increased sensitivity through higher Q without any restriction on the detection bandwidth B, which approximately represents the number of pixels per second that can be recorded. In the FM mode the signal used to produce the image comes from the direct measurement of the resonance frequency of the cantilever, which is modified, as in the AM case, by the tip-surface interaction [6, 8].

At variance with the AM mode, the cantilever is kept oscillating at its current resonant frequency (different from f_0 due to the tip-sample interaction) with a constant amplitude A_0. The driving signal of the cantilever oscillations is generated through a feedback loop. The output of the deflection sensor is amplified, phase shifted by -90° and used to drive the cantilever (self-excitation scheme) [6, 16, 8]. Usually, either the input signal to the self excitation circuit or its inputs signal is bandpass filtered with the center frequency set to the fundamental resonance of the cantilever. Moreover the excitation amplitude A_{exc} is adjusted to keep the oscillation amplitude of the tip constant. The variation of A_{exc} may be measured

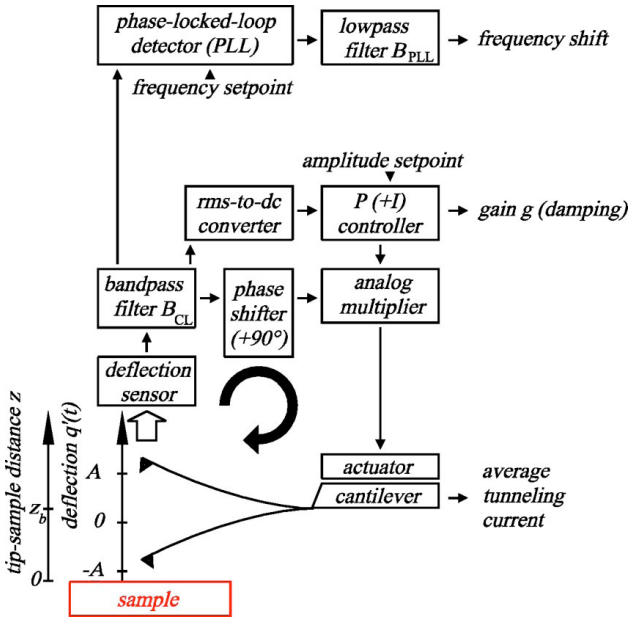

FIGURE 2.8: Block diagram of the FM-AFM feedback loop for constant amplitude control and frequency-shift measurement. Three physical observables are available: frequency shift, damping signal and (average) tunneling current. From [8].

giving the additional energy dissipation due to tip-surface interaction.

The controlled FM-AFM positive feedback is shown in Fig. 2.8. The deflection signal first enters a bandpass filter. Then the signal splits into three branches: one branch is phase shifted, routed through an analog multiplier, and fed back to the cantilever via an actuator; one branch is used to compute the actual oscillation amplitude, this signal being used to calculate a gain input g to keep constant oscillation amplitude; and one branch is used to feed a frequency detector. The frequency f is determined by the eigenfrequency f_0 of the cantilever and the phase shift ω between the mechanical excitation generated at the actuator and the deflection of the cantilever. Since $\omega = \pi/2$, the loop oscillates at $f = f_0$, see Fig. 2.5.

Indeed the control circuitry required by FM-AFM is complex since three feedbacks operate simultaneously. The first keeps the oscillation amplitude of the cantilever constant, the PLL system adjusts the frequency of the excitation os-

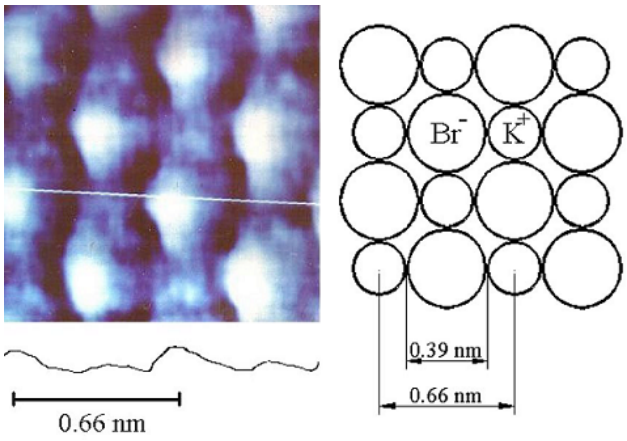

FIGURE 2.9: Atomically resolved image of KBr(001) in contact AFM mode. The small and large protrusions are attributed to K^+ and Br^- ions, respectively. Schematic diagram showing major components of a scanning force microscope with an optical beam deflection system. From [17].

cillation to keep the phase constant (self-excitation) and the third controls the tip-sample distance to maintain the frequency shift setpoint since during the scan, the tip-sample distance is varied in order to achieve a set value of Δf. Thus, the topography in the images represents a map of constant frequency shift over the surface.

2.5 AFM imaging

Atomic resolution of inert surfaces is successfully performed by static AFM, as shown in Fig. 2.9 [17] where KBr surface is resolved on an atomic scale by using a 4-K ultrahigh-vacuum (UHV) instrument. Nevertheless, imaging reactive surfaces such as Si(111)-(7 × 7) in ultra-high vacuum remained an unsolved challenge for static AFM that was solved by dynamic operation modes.

The atomic resolution of dynamic AFM has been proved on semiconductor surfaces by Erlandsson *et. al.* [18] who imaged the Si(111)7 × 7 surface with the amplitude modulation technique whereas Giessibl [19] demonstrated the atomic

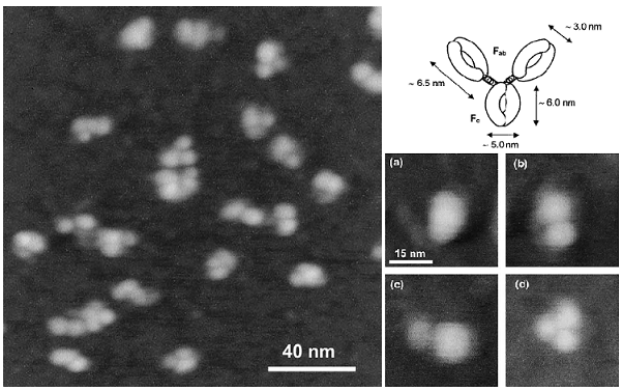

FIGURE 2.10: Tapping-mode AFM image (attractive interaction regime) of several antibodies obtained in air and at room temperature. The molecules show the morphologies of the characteristic Y shape of antibodies according to the orientation with respect to the support which are zoomed in A-D. From [20].

resolution on Si(111)-7×7 operating in UHV and using the FM detection mode.

The AM mode has been used to image a variety of system such as non organic surfaces or nanostructures see [9, 3] even if it is most often used in biomaterials science, due to the relatively small interactions between the tip and the sample, especially in the lateral direction of the surface, so that the sample distortion or damage is minimized [6, 4, 5].

In [20] high-resolution imaging of antibodies is provided by AM-AFM in attractive interaction regime i.e. when a net attractive force dominates the amplitude reduction and the tip-sample contact is avoided. Fig. 2.10 is a tapping-mode AM-AFM image of the simplest antibody molecules, the anti-human serum albumin a-HSA. The molecules have four basic morphologies associated with the orientation of the antibodies on the support. The apparent size of a given molecule is independent of the number of times this molecule has been imaged. This demonstrates that the AM-AFM prevents any sample damage also in case of soft biological sample weakly adherent to the substrate.

Achieving molecular resolution images of biological systems has been much more difficult than obtaining atomic resolution images of crystalline surfaces,

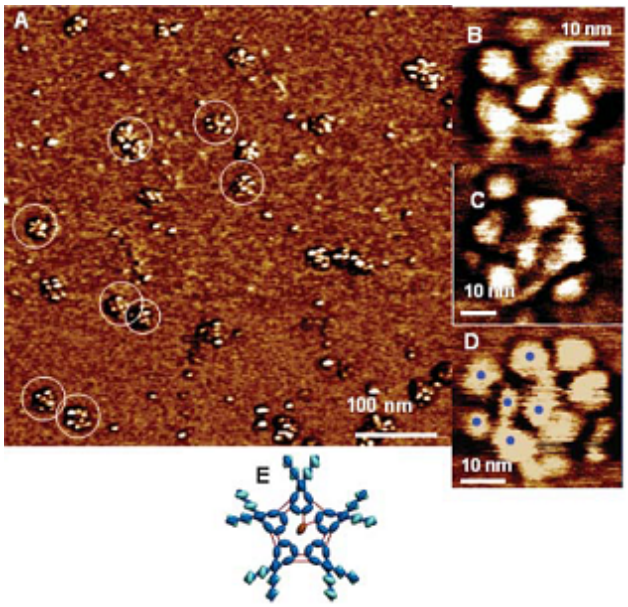

FIGURE 2.11: A) Bi-modal AFM phase image of mica surface with IgM pentamers. The image represents the variation of the phase shift of the second mode across the sample surface. B)-D) individual bi-modal images showing five subunits and a central structure (J-chain). E) Model of IgM. From [21].

see [21]. Usually, the forces exerted by the tip on the molecules either displace them laterally or break the noncovalent bonds that held the biomolecules together which in turn prevents high resolution imaging. The use of higher harmonics (multi-modes force microscope) enhances the sensitivity to tip-surface interactions and so enables imaging under the application of forces which are as small as needed by to avoid biomolecules damages [13, 14]. With this technique a complex protein structure such as the antibody immunoglobulim M pentamers (IgM) has been resolved [21]. The pentagonal shape and the position of the J-chain (central structure) are readily recognized in high resolution bi-modal phase images acquired in a noninvasive manner (Fig. 2.11).

FM-AFM is mostly used in UHV environments since it provides increased sensitivity through high-Q stiff cantilever. The atomic resolution was demonstrated on Si(111)-7×7 reconstruction and on InP(110) operating in UHV and using the

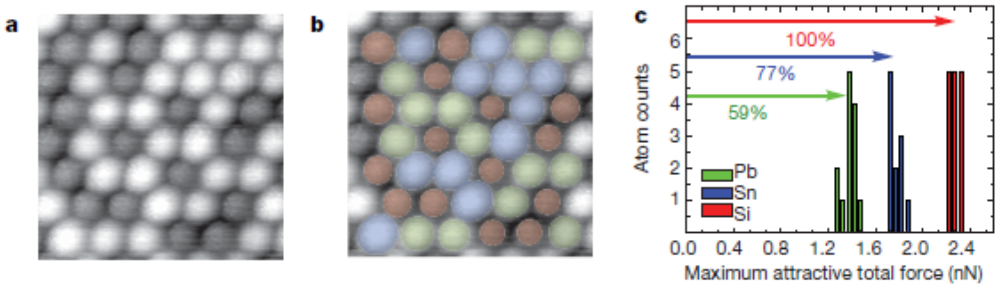

FIGURE 2.12: a) Topographic image of a surface alloy composed by Si, Sn and Pb atoms blended in equal proportions on a Si(111) substrate. b) Local chemical composition of the image in a). Blue, green and red atoms correspond to Sn, Pb and Si, respectively. c) Distribution of maximum attractive total forces measured over the atoms in a). By using the relative interaction ratio determined for Sn/Si and Pb/Si, each of the three groups of forces can be attributed to interactions measured over Sn, Pb and Si atoms. Adapted from [24].

FM detection mode, see [22, 23, 19].

The chemical identification of single atoms and molecules at surfaces is a challenge pursued since the invention of the atomic force microscope. Dynamic force microscopy is particularly promising since it achieves true atomic imaging resolution by detecting the short-range forces which depends sensitively on the chemical identity of the atoms involved since they are associated with the onset of the chemical bond between the outermost atom of the tip apex and the surface atoms being imaged. Sugimoto *et. al.* [24] performed precise measurements of such short-range chemical forces and showed that their dependence on the tip used can be overcome through a normalization procedure. This allowed to exploit the chemical force measurements as the basis for atomic recognition, even at room temperature. The effectiveness of the approach was verified by imaging the surface of a particularly challenging alloy system. The three constituent atomic species silicon, tin and lead, were successfully identified, even though they exhibit very similar chemical properties and identical surface position preferences that render any discrimination attempt based on topographic measurements impossi-

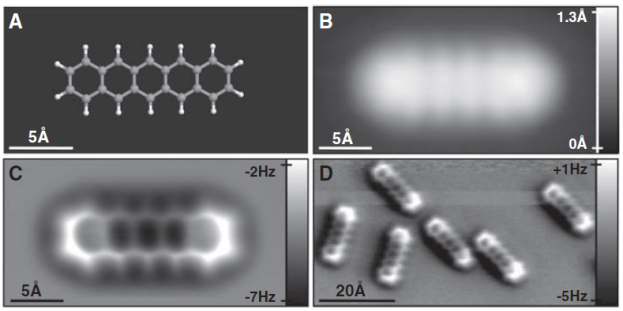

FIGURE 2.13: STM and AFM imaging of pentacene on Cu(111). A) Ball-and-stick model of the pentacene molecule. B) Constant-current STM and (C and D) constant-height AFM images of pentacene acquired with a Co-modified tip. From [25].

ble (Fig. 2.12).

Another important goal of FM-AFM is the imaging with atomic resolution of the complete chemical structure of an individual molecule. This is possible by functionalizing the microscopes tip apex with suitable, atomically well-defined terminations which dramatically enhances the atomic scale contrast [25]. Pentacene $C_{22}H_{14}$ molecules are imaged in FM-AFM modes on Cu(111) by using a CO-terminated tip, clearly resolving the five hexagonal carbon rings of each pentacene molecule, see Fig. 2.13.

2.6 Force Spectroscopy

Atomic force microscopy (AFM) has developed into a powerful technique, delivering not only topographical images with sub-molecular resolution but providing also sensitive force measurements on the nanometer and atomic scale [16, 6, 8, 10]. The use of AFM in such tip-sample force measurements is commonly referred to as *force spectroscopy*. The simplest technique used for quantitative force measurements involves directly monitoring the static deflection of the cantilever, from which the force is determined using Hooke's law [26, 27, 28]. In [28] the transition from van der Waals to Casimir forces between macroscopic gold surfaces in air is

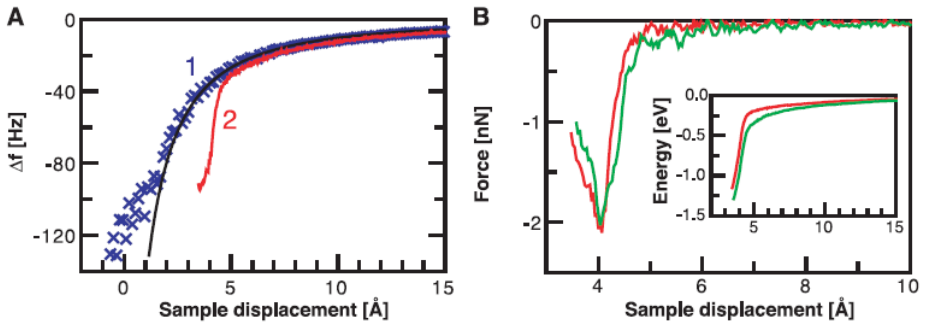

FIGURE 2.14: Short-range force and interaction energy (inset) measured above two different sites of the Si(111)-7×7 surface. From [31].

investigated by AFM in the plane-sphere geometry by measuring the cantilever static bending. The sphere and plate geometry is given by a sphere on cantilever with a diameter of 100 μm and a flat surface. The Hamaker constant of the van der Waals interactions between real Au surfaces in air is estimated in agreement with theoretical predictions.

More refined techniques suitable for nanoscale investigations rely on measuring the dynamical parameters of the cantilever excited at or near its resonant frequency while experiencing the force field of the sample surface. The interactions of the tip with the sample surface perturbs the amplitude, frequency, phase or damping of the cantilever oscillation. The measurement of these parameter modifications provides a sensitive estimation of both tip sample interaction force [29, 30, 25, 31, 32, 33, 34].

Tip-sample forces versus distance can be inferred from resonance frequency shift versus distance curves [29, 31, 34]. Lantz *et. al.* [31] performed spectroscopy over specific atomic sites on the Si(111)-7×7 using a low-temperature AFM operating in UHV environment, see Fig. 2.14. After image acquisition, the tip is positioned above a specific lattice position determined from the atomically resolved image. The shift in resonance is then recorded while the sample is ramped toward the tip by a fixed distance. The force acting on the tip at the distance of the closest approach to the sample during an oscillation cycle is calculated by inverting

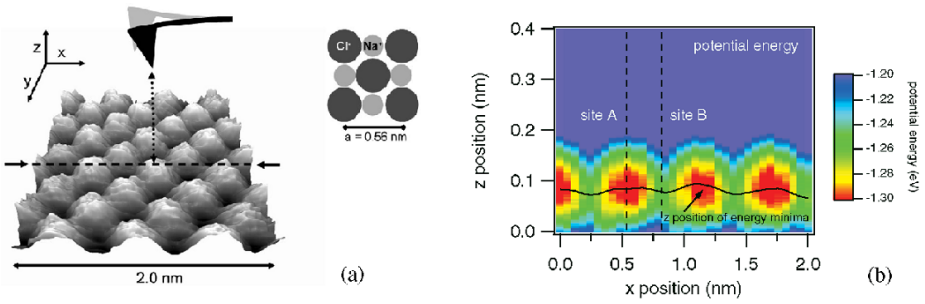

FIGURE 2.15: a) The gray scale height image shows the surface topography at a constant frequency shift obtained in conventional scan mode of noncontact atomic force microscopy on NaCl(100) in ultrahigh vacuum. For 3D spectroscopy the frequency shift was acquired as a function of tip-sample distance z for 34 points along the dashed line in x direction. b) Image of the tip-sample potential energy as a function of horizontal and vertical tip position. The black line indicates the z positions of the potential energy minima. Adapted from [35].

the frequency-distance measurement. The force has three main contributions: a strongly site-dependent short range force as well as long-range electrostatic and van der Waals forces. The short-range force due to the chemical interaction is determined by subtracting the site independent long-range force. The interaction potential and energy measured above inequivalent adatom sites displays differences suggesting the possibility to distinguish between different atomic species.

Performing force spectroscopy on planes over the sample gives the potential energy landscape of surfaces. The shape of the potential interaction energy profile between a single-atom terminated tip and a NaCl(100) surface is measured in [35]. Experiment is performed with an UHV AFM by measuring the force induced frequency shift as a function of relative tip-sample distance on a predefined grid, consisting of 34 equidistant points along the x axis for 10 equidistant positions along the y axis. Each spectroscopy curve required an acquisition time of approximately 2.5 s. Hence, including the extra time needed for feedback stabilization after each spectroscopy curve the total time for one slice in space at each y position amounted to 1.5 min. The image of the tip-sample potential energy as a function

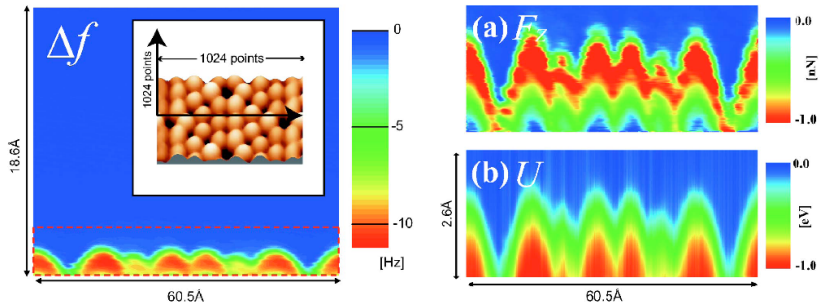

FIGURE 2.16: On the left the two-dimensional frequency shift mapping on the Si(111)-7×7 surface. Data acquisition was performed above the arrow connecting the two corner holes in the inset. The hatched lines define data inverted to provide figures on the right. a) Total force and b) the interaction potential. From [36].

of horizontal and vertical tip position is shown in Fig. 2.15.

In [36], a two-dimensional force mapping on Si(111)-7×7 surface was performed at room temperature in the plane of the 60.5Å×18.6Å area above the line connecting the two corner holes, see Fig. 2.16. Again interaction forces are provided by inverting the frequency shift versus distance curves (Eq. 3.13). It took approximately 3.5 min to obtain two-dimensional mapping image of 1024×1024 points, so that thermal drift effects had to be compensated.

An alternative way to perform force spectroscopy is the broad band excitation technique. In this case the cantilever is excited and the response recorded over a band of frequencies simultaneously, rather than at a single frequency as in conventional SPM. The full spectral response allows to reconstruct force-distance spectroscopy and enables to directly measure the energy dissipation through the determination of the Q-factor of the cantilever-sample system. The simultaneous analysis at all frequencies within the excited band (parallel detection) reduces the acquisition time. Broad band excitation can be achieved by external driving force [37] or by thermal excitation [38, 39].

The external band excitation (BE) takes advantage of the fact that only selected regions of Fourier space contain information of any practical interest [37], for instance in the vicinity of resonances. The generic BE process is illustrated in

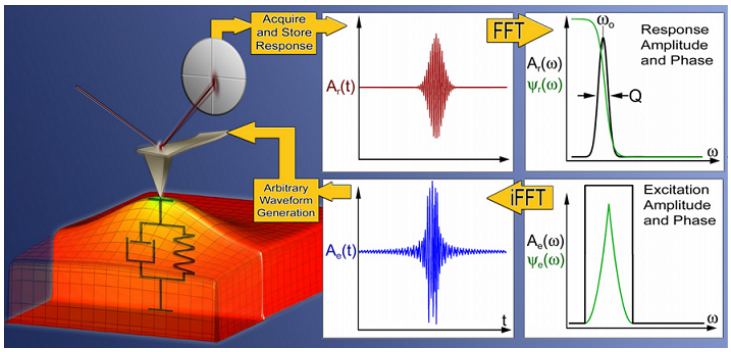

FIGURE 2.17: Operational principle of the BE method in SPM. The excitation signal is digitally synthesized to have a predefined amplitude and phase in the given frequency window. The cantilever response is detected and Fourier transformed at each pixel in an image. The ratio of the fast fourier transform of response and excitation signals yields the cantilever response (transfer function). Fitting the response to the simple harmonic oscillator yields amplitude, resonance frequency, and Q-factor, that are plotted to yield 2D images. From [37].

Fig. 2.17. Instead of a simple sinusoidal excitation, the BE method uses a signal generated to have the predefined Fourier amplitude density and phase contrast in the frequency band of interest. The inverse Fourier transform releases the excitation signal in time domain. The resulting complex waveform is used to excite the cantilever. The cantilever response to the BE drive is measured and Fourier transformed to yield the amplitude and phase-frequency curves. The acquisition is repeated at several distances from the surface providing a 3D data set i.e. $A(\omega)$ and $\vartheta(\omega)$ at each tip-sample separation (Fig. 2.18a). The ratio of the response and excitation signals yields the transfer function of the system. The measured response curves are analyzed by fitting each curve independently to the simple harmonic oscillator (SHO) model to determine the resonant frequency, amplitude, and Q-factor at each distance and display each as 2D image. and/or use as feedback signals, see Fig. 2.18b. This fast Fourier transform/fitting routine substitutes the traditional lock-in/lowpass filter that provides amplitude and phase at a single frequency at time. In the BE method, parallel acquisition of the response at all

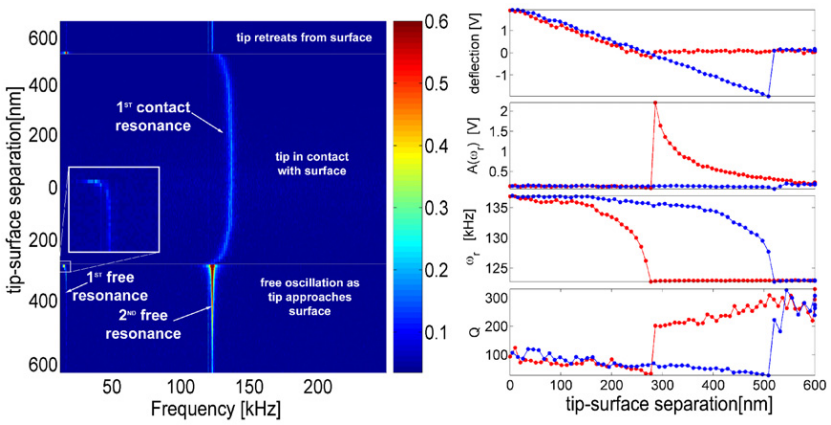

FIGURE 2.18: (a) Evolution of the dynamic properties of the cantileversurface system during forcedistance curve acquisition. (b) Deconvolution of the BE data in amplitude, resonant frequency, and Q-factor measured along the forcedistance curve. From [37].

frequencies within the band allows complete spectral acquisition at a rate of ∼10 ms for each tip-sample separation. Thus, in the BE response the system is excited and the response is measured simultaneously at all frequencies within the excited band (parallel detection). With standard lock-in detectors the response over a broad band is acquired by sampling one frequency at time. The BE approach allows a time reduction for acquiring a sweep by a factor of 10100 by performing this detection on all frequencies in parallel. Moreover, the BE acquisition time does not depend on the width of the frequency band, or, equivalently, on the number of frequency analyzed (unlike lock-in detection, which scales linearly with this number).

As an illustration of force spectroscopy, BE mapping of the frequency dependence of the cantilever response with tipsurface separation under an electrostatic broad band driving force is illustrated in Fig. 2.18a. The measurements are performed on a freshly cleaved mica surface in ambient. On approaching the surface (bottom to top) the the resonance frequency remains constant (region I). In the close vicinity of the surface, the resonant frequency decreases due to strong attractive interactions (inset). A rapid change in the resonant structure occurs upon

transition from the free to bound cantilever modes (jump to contact). Upon increasing the contact force by loading the cantilever, a slight increase in contact stiffness is observed (region II). The reverse sequence is observed during retraction (region III). The total acquisition time for this data is approximately 100 s since it is the mean of 128 curves each recorded into ∼1 s. The individual resonances at points along the vertical tip trajectory can be fitted by the SHO model and the resulting evolution of amplitude, resonant frequency, and quality factor are shown in Fig. 2.18b. Force versus distance curve can be inferred from the frequency's evolution, energy dissipation from phase and quality factor. Note that BE allows an extremely broad frequency range (25-250 kHz) to be probed in ∼1 s. A comparable scan over the same frequency band using a lock-in would require ∼30 min.

2.7 Summary

In this chapter we review the fundamental applications of static and dynamic AFM methods. In particular we describe how the changes observed in the dynamic properties of a vibrating tip that interacts with the surface make it possible to obtain molecular resolution images or to chemically resolve surfaces in UHV. Currently, AM-AFM is used very successfully in ambient condition or in liquid environments to imaging biological specimens systems whereas using the FM operating mode in UHV environments dramatically improves the resolution up to atomic scale. This division is not artificial. Amplitude modulation will be an unlike technique for UHV because the high quality factor of the microlever ($Q \approx 10^4$) would imply extremely slow feedback responses. On the other hand, FM-AFM requires three feedback loops which makes its electronics complex and slow for operation in air or liquids. Due to their characteristic, AM-AFM is widely applied in imaging biological system with molecular resolution while FM-AFM is more suitable for non organic sample imaged and chemically resolved on the atomic scale.

Atomic force microscopy provides also sensitive measurements of forces between the tip and the sample (*force spectroscopy*). FM-AFM quantifies the interaction forces by detecting the shift of the cantilever resonant frequency from the free-oscillation value upon variations in the tip-sample distance. Through the precise quantification of the short-range chemical forces responsible for atomic contrast, this spectroscopic technique has provided valuable information to unravel complex atomistic processes taking place between tip and surface and it has endowed FM-AFM with atomic specificity.

An alternative way to perform force spectroscopy is the broad band excitation technique. In this case the cantilever is excited and the response recorded over a band of frequencies simultaneously, rather than at a single frequency at a time as in conventional SPM. The full spectral response allows to reconstruct force-distance spectroscopy and enables to directly measure the energy dissipation of the cantilever-sample system. The simultaneous analysis at all frequencies within the excited band (parallel detection) reduces the acquisition time.

The main limitation of these spectroscopy techniques regards the time required to record a complete force-versus distance curve. In any case, the lower limits in time is in the order of 0.1-1 s required to detect a complete force spectroscopy. This long acquisition times are incompatible with 1-30 ms/pixel required for practical scanning probe microscopy. This is the reason why we introduce a new approach to spectroscopy measurements, the wavelet transform in thermally excited dynamic spectroscopy. The technique presented in this thesis allows to study the tip-sample interaction across the JTC transition and to characterize the adhesion surface forces after JTC. The temporal resolution is improved and the acquisition time reduced to values compatible with practical dynamical force spectroscopy imaging. The analysis applies simultaneously to all the modes either flexural ad torsional within the cut frequency of the acquisition system.

Chapter 3

Dynamic response of AFM cantilevers

Dynamic force spectroscopy utilizes the response of an excited cantilever to the interaction of the tip with surface forces to probe the mechanical, chemical and topographical characteristics of the surface at the nanoscale [16, 6]. The response of the cantilever may show a modification of the oscillation amplitude, frequency, phase or damping. The measurement of these cantilever parameters provides information on the physical properties of the sample with (sub-)molecular resolution [24, 25]. The dynamic behavior of a weakly interacting cantilever in the vicinity of the resonance can be well approximated by a simple harmonic oscillator model, described by three independent parameters: resonant frequency, ω_0, amplitude at resonance, A_0, and quality factor, Q. A shift in ω_0 is related primarily to the tip-surface force gradient, A_0 to the driving force, and Q to the energy dissipation [8, 6, 40]. Here we describe the cantilever from a thermodynamical point of view in order to relate its oscillating behavior to the tip-sample interaction. The nature of these force interaction is also discussed.

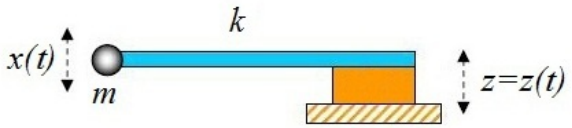

FIGURE 3.1: Probe model as an elastic cantilever with a mass at one end.

3.1 Introduction

The exact description of the AFM cantilever oscillations is a complex mathematical task [41, 42]. However, the basic features of the processes occurring during interaction of an oscillating cantilever with the environment and the surface can be understood on the basis of elementary models, in particular, using the approximation of a localized mass model. The cantilever is described as an elastic massless beam (with elastic constant k), fixed at one end to the chip, plus a mass m localized on the other end (Fig. 3.1).

The oscillating behavior of the system depends on the forces acting on it. First we describe the mechanical response of the free cantilever to the thermal excitation induced by the energy exchange with the environment through the Fluctuation-Dissipation Theorem. Then we consider variations in the cantilever dynamics caused by forces between tip and sample. Detecting these changes allows to reconstruct the tip-sample interaction potential and to characterize the chemical and/or physical properties of the sample surface. A review of the experimental methods and results in measuring these forces is presented at the end of the chapter.

3.2 Free cantilever fluctuations

When a mechanical system is in equilibrium with a thermal bath at temperature T, there is a continuous exchange between the mechanical energy accumulated in the system and the thermal energy of the local environment, the driving reservoir. The statistic interpretation of the Second Thermodynamic Principle leads to admit that

a system in thermodynamic equilibrium is not at rest but continuously fluctuates around its equilibrium state. These thermal fluctuations are always present at non zero absolute temperature.

Consider a system whose the extensive variable x is coupled to the intensive parameter F in the Hamiltonian of the system [43]. The response function $G(\omega)$ describes the response x of the system to the driving variable F in the frequency domain and is defined as:

$$G(\omega) = \frac{F(\omega)}{x(\omega)}$$

$G(\omega)$ The thermal fluctuations of an observable x are described by the Fluctuation-Dissipation theorem [43, 44] which relates the power spectral density (PSD) of the fluctuations of the variable x, $S_x(\omega)$, to the temperature and the response function $G(\omega)$ [45] as:

$$S_x(\omega) = \frac{x^2(\omega)}{\Delta\omega} = -\frac{2k_BT}{\omega}\mathbf{Im}\left[\frac{1}{G(\omega)}\right] \tag{3.1}$$

where k_B, $\Delta\omega$ and $\omega = 2\pi f$ are the Boltzmann constant, the angular frequency bandwidth and the angular frequency or pulsation associated to frequency f. **Im** stands for the imaginary part of its argument. The average shape of a spontaneous fluctuation pulse is identical with the observed shape of a macroscopic irreversible decay toward equilibrium and is, therefore, describable in terms of the macroscopic response function.

An example of mechanical dissipative system is the AFM cantilever placed in air far from the surface (free cantilever) and driven by background thermal energy. The cantilever is in thermal equilibrium with the molecules of the gas or liquid in which it is immersed and fluctuates in response to stochastic forces due to molecular motion that is connected to the temperature of the thermal bath. The cantilever dynamics can be reasonably modeled as a stochastic harmonic oscillator with viscous dissipation [46, 47, 48]. In this case x and F are the displacement and the force applied to the system. The Brownian motion of the vertical coordinate

x of the cantilever free end is described by the second order Langevin equation

$$m\ddot{x}(t) + \gamma\dot{x}(t) = -kx(t) + F_{ext}(t) \tag{3.2}$$

Here m and k mean the cantilever effective mass and elastic stiffness, respectively, γ the damping factor. The external driving force F_{ext} is the thermal stochastic force which accounts for the interaction with the local environment. F_{ext} is defined by its statistic properties (Langevin hypothesis) [49, 48, 44]:

- $F_{ext}(t)$ is a zero-mean force $\langle F_{ext}(t)\rangle = 0$
- $F_{ext}(t)$ is completely uncorrelated in time:

$$\left\langle F_{ext}(t)F_{ext}(t')\right\rangle = \alpha\delta(t-t') \tag{3.3}$$

where $\delta(t-t')$ is the Dirac delta function and α a proportionality constant whose value will be determined in the following through the fluctuation-dissipation theorem. Since the autocorrelation function and the spectral density are mutual Fourier transform (Wiener-Khintchine theorem [43, 48]), the power spectrum of the stochastic thermal activating force $S_F(\omega) = \alpha$. Hence the stochastic force of the physical system has no frequency dependence, the reason why it is called *white noise*.

The transfer function of the system is provided by writing Eq. 3.2 in the Fourier space (frequency domain) as

$$G(\omega) = k\left[1 - \frac{\omega^2}{\omega_0^2} + \mathrm{i}\frac{\omega}{Q\omega_0}\right] \tag{3.4}$$

where we introduced the resonant angular pulsation $\omega_0 = \sqrt{k/m}$ and the quality factor $Q = m\omega_0/\gamma$. In this case, from Eq. 3.1 and Eq. 3.4, the PSD of the thermal fluctuations x is given by

$$S_x(\omega) = \frac{2k_BT}{k\omega_0}\frac{1/Q}{(1-u^2)^2 + (u/Q)^2} \tag{3.5}$$

where $u = \omega/\omega_0$ is the reduced frequency. The PSD of the fluctuations $S_x(\omega)$ is related to the PSD of the driving force $S_F(\omega)$ trough the response function

$G(\omega)$ [47] by

$$S_F(\omega) = S_x(\omega)G^2(\omega) \tag{3.6}$$

The power spectrum of the stochastic thermal activating force F is deduced from Eq. 3.4, Eq. 3.6 and Eq. 3.5 giving

$$S_F(\omega) = 2k_BT\gamma$$

Therefore the α constant in Eq. 3.3 as determined from the Fluctuation-Dissipation theorem is $\alpha = 2k_BT\gamma$ providing an autocorrelation function of the external stochastic force expressed by:

$$\left\langle F_{ext}(t)F_{ext}(t')\right\rangle = 2k_BT\gamma\delta(t-t')$$

The last relation quantifies the intimate connection between the viscous coefficient γ and the randomly fluctuating force $F_{ext}(t)$: the fluctuating force is an increasing function of γ and vanishes identically if and only if γ vanishes. This is a consequence of the fact that the microscopic events that give rise to those two forces (the damping force $-\gamma\dot{x}$ and the fluctuating force F_{ext}) simply cannot be separated into one kind of microscopic event (like the molecular collision) that give rise *only* to a viscous effect and another kind that give rise *only* to a fluctuating effect.

The Parseval relation allows to determined the variance of the fluctuations of the observable x (in our case the cantilever positional fluctuations) by integrating the positional PSD $S_x(\omega)$. Then:

$$\left\langle x^2\right\rangle = \int_{-\infty}^{+\infty} S_x(\omega)d\omega = \frac{2k_BT}{k\omega_0 Q}\int_{-\infty}^{+\infty}\frac{d\omega}{\left(1-\frac{\omega^2}{\omega_0^2}\right)^2+\left(\frac{\omega}{Q\omega_0}\right)^2} = \frac{k_BT}{k} \tag{3.7}$$

where we used Eq. 3.5 and the relation:

$$\int_{-\infty}^{+\infty}\frac{d\omega}{\left(1-\frac{\omega^2}{\omega_0^2}\right)^2+\left(\frac{\omega}{Q\omega_0}\right)^2} = \frac{Q\omega_0}{2}$$

Considering Eq. 3.7, the potential energy of the cantilever modeled as a damped harmonic oscillator takes the form of:

$$\frac{1}{2}m\omega_0^2 \left\langle x^2 \right\rangle = \frac{1}{2}k \left\langle x^2 \right\rangle = \frac{1}{2}k_B T$$

where $\left\langle x^2 \right\rangle$ represents the mean square displacement of the cantilever caused by the thermal motion in the direction normal to the surface. This relation corresponds to the equipartition theorem stating that if a system is in thermal equilibrium, the mean value of any harmonic term in energy must be equal to the thermal energy to $1/2k_BT$.

Finally, by applying the Fluctuation-Dissipation theorem (Eq. 3.1) to an harmonic damped oscillator we demonstrate the equipartition theorem. The reverse path to infer the Fluctuation-Dissipation theorem from the equipartition theorem is also possible [47, 44].

The mean-square amplitude of the cantilever thermal fluctuation experimentally measured in the frequency domain is often used to estimate the cantilever spring constant k [41, 50] from:

$$\left\langle x^2 \right\rangle = \int_0^\infty 2S_x(f)df = \frac{k_B T}{k}$$

3.3 Interacting cantilever

Near the surface the tip experiences the sample force. During the surface approach, the cantilever motion is affected by the additional force $F_{ts}(z)$ due to van der Walls interaction with the sample. For small oscillations of the cantilever around the distance z_0 from the surface, as for examples in case of thermal excitations, the force may be approximated by the first (linear) term in the series expansion [40, 8]:

$$F_{ts}(z) = F_{ts}(z_0) + \frac{\partial F_{ts}}{\partial z}(z_0)x$$

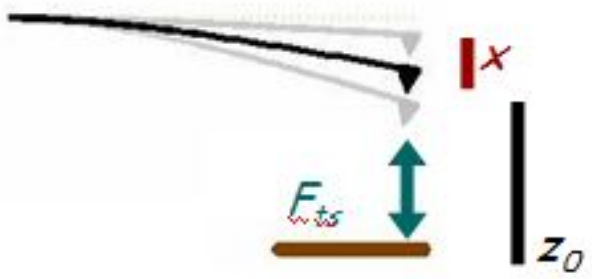

FIGURE 3.2: Model of the interacting cantilever.

where z is the tip-surface distance, positive along the surface normal direction. The cantilever motion is now described by

$$m\ddot{x}(t) + \gamma\dot{x}(t) + kx(t) = F_{ext}(t) + F_{ts}(z_0) + \frac{\partial F_{ts}}{\partial z}(z_0)x(t) \tag{3.8}$$

The constant force F_{ts} statically deflects the cantilever, the force gradient influences the cantilever oscillations around the new equilibrium position. In fact, with the variables substitution $x = x + F_{ts}(z_0)/k$ which incorporates the cantilever static bending, we come to the equation

$$m\ddot{x}(t) + \gamma\dot{x}(t) + \left(k - \frac{\partial F_{ts}}{\partial z}(z_0)\right)x(t) = F_{ext}(t) \tag{3.9}$$

where x is the cantilever vertical motion and z_0 the separation from the surface(Fig. 3.2).

This means that in case of small oscillations the derivative of the tip-sample force is constant for the whole range covered by the oscillating cantilever and the presence of a force gradient results in a change of effective stiffness of the system

$$k^* = k - \frac{\partial F_{ts}}{\partial z} \tag{3.10}$$

Presence of a gradient in the tip-surface interaction force results in a shift of the amplitude and phase response curves of the oscillating cantilever. The change in the effective spring constant modify the cantilever resonance frequency since $\omega_0 = 2\pi f_0 = \sqrt{k/m}$ and therefore

$$f_0' = f_0\sqrt{1 - \frac{1}{k}\frac{\partial F_{ts}}{\partial z}}$$

In case of small force gradient ($|\partial F_{ts}/\partial z| << k$ the shift in eigenfrequency $\Delta f = f_0' - f_0$ becomes proportional to the force gradient

$$\frac{\partial F_{ts}}{\partial z} = -2k\frac{\Delta f}{f_0} \tag{3.11}$$

By measuring the frequency shift Δf, one can determine the tip-sample force gradient.

Approaching the surface, the attractive tip-sample force causes a sudden jump-to-contact. The instability occurs in the quasistatic mode if

$$-\frac{\partial F_{ts}}{\partial z}(z_{jtc}) > k \tag{3.12}$$

The jump to contact often renders the short-range part of the interaction curve inaccessible experimentally. The jump-to-contact can be avoided even for soft cantilevers by dynamic methods i.e. by oscillating the cantilever a large enough amplitude. FM-AFM detects with high sensitivity minute changes in the resonant frequency due to the force interaction between cantilever tip and sample. In this case the relation connecting the frequency shift to the interaction force is significantly more complex and depends on both the spring constant and amplitude of oscillation [51]

$$\Delta f = -\frac{f_0}{\pi A k}\int_{-1}^{1} F_{ts}(z + A(1-u))\frac{u}{\sqrt{1-u^2}}du \tag{3.13}$$

where f_0 is the unperturbed resonance frequency, Δf the change in resonance frequency, A the amplitude of oscillation kept constant during the measurement and z is the distance of closest approach between tip and sample.

3.4 Tip-sample force interaction

The tip-sample interaction can be modeled by two main contributions, short range forces (such as bonding forces) and long range forces (such as van der Waals and electrostatic forces) [8, 51, 10, 6], see Fig. 2.2. In ambient conditions, meniscus

forces formed by adhesion layers on tip and sample (water or hydrocarbons) can also be present [52, 53]. The van der Waals interaction is caused by fluctuations in the electric dipole moment of atoms and their mutual polarization. For two atoms at distance z, the energy varies as $1/z^6$. Assuming additivity and disregarding the discrete nature of matter by replacing the sum over individual atoms by an integration over a volume with a fixed number density of atoms, the van der Waals interaction between macroscopic bodies can be calculated by the Hamaker approach [54] This approach does not account for retardation effects due to the finite speed of light and is therefore only appropriate for distances up to several hundred angstroms. For a spherical tip with radius R next to a flat surface (z is the distance between the plane connecting the centers of the surface atoms and the center of the closest tip atom) the van der Waals potential is given by [55, 56]

$$V_{vdW} = -\frac{HR}{6z}$$

The van der Waals force for spherical tips is thus proportional to $1/z^2$, while for pyramidal and conical tips, a $1/z$ force law holds [51]. The Hamaker constant H depends on the type of materials (atomic polarizability and density) of the tip and sample. For most solids and interactions across a vacuum, H is of the order of 0.1 aJ [56, 57, 58].

Approximating tip and sample by a continuum is valid if z is significantly greater than the interatomic distances. If z is in the order of the next-neighbor distance σ, the continuum vdW force can be superseded by the van der Waals force between the front atom and the sample atom closest to it. If tip and sample have exposed dangling bonds, chemical bonding can also occur. The simplest modele of this chemical short-range interaction is provided by a Lennard-Jones potential with bond energy E_{bond} and equilibrium distance σ:

$$V_{LJ} = -E_{bond}\left[2\left(\frac{\sigma}{z}\right)^6 - \left(\frac{\sigma}{z}\right)^{13}\right]$$

Different potentials used to quantitatively describe the chemical short-range forces are provided by [8, 6] and references in it.

When AFM experiments are performed in air, a thin liquid film composed mostly of water adsorbs on all surfaces. Due to the presence of this film, the surface properties can change dramatically. The physics and chemistry of these films are very rich and complex: they determine friction and adhesion of surfaces, chemical reactivity, optical properties, among others. Moreover, as the SFM tip approaches the surface, water condensation can induce the formation of a nanometer-sized water bridge even before tip and sample are in mechanical contact [52, 53, 59]. This meniscus implies an attractive (capillary) force. With soft cantilevers (< 1 N/m), this meniscus can be strong enough to pull the tip onto the sample so that the tip jumps onto the sample long before the critical jump distance is reached and the resonance frequency does not drop to zero, see Eq. 3.12 and Eq. 3.11. Therefore, the jump to contact observed typically in SFM under ambient conditions is mainly not due to van der Waals forces, but a two-fold process: first, when the tip is at a distance of about 2-3 nm, a liquid meniscus forms between tip and sample, and afterward, this meniscus pulls the tip onto the sample so that a mechanical contact between both is formed. The process of water films formation depends on relative humidity. Water could be ever observed on a highly hydrophobic surface like graphite where the presence of the scanning tip produces the condensation of water on the surface [52].

3.5 Summary

Here the AFM cantilever is modeled as a damped harmonic oscillator to characterize its response to the local environment energy exchanges. The thermally excited Brownian motion of the cantilever tip is connected to the local mechanical compliance via the fluctuation-dissipation theorem. The interaction potential can be reconstructed by the modification of the thermal motion of the cantilever due to the tip-surface forces. In particular, we present the relation between the frequency shift and the tip-sample interaction force for both large and small oscil-

lations amplitude. The van der Waals long-range forces are model by an Hamaker potential, the short-range interaction by a Lennar-Jones potential. In ambient condition, effects of capillary forces due to liquid neck between tip and surface are discussed.

Chapter 4

Time meets frequency

The mathematical framework used for simultaneous analysis of the signal's time and frequency properties is the wavelet transform analysis. This is often compared with the Fourier transform, in which signals are represented as a sum of sinusoids. The main difference is that wavelets are localized in both time and frequency whereas the standard Fourier transform is only localized in frequency. The wavelet transform is a time-frequency analysis method which provides localized information in time and frequency domain simultaneously (time-frequency representation) [60, 61]. Nevertheless it is necessary to determine the time and frequency resolution of wavelet transforms and how this resolution depends on wavelet parameters. Time-frequency analysis by wavelet transform is an effective tool to characterize the spectral content of signals rapidly varying in time. Therefore it has been successfully adopted for a vast number of applications in many areas of physics and engineering for quantitative measurements.

4.1 Introduction

Experimental data frequently appear as a time series. In order to be characterized, time signals are transformed in frequency domain to describe their spectral content. A fundamental method for signal processing is the Fourier transform (FT). However the Fourier analysis is devised for stationary system i.e. the frequency spectrum is correctly correlated only with a temporally invariant physical system. This leaves aside many applications where the spectral content of the signal changes during the data collection. This change is not revealed by FT which only provides an average over the time period and prevents from correlating the frequency spectrum with the signal modification in time.

To overcame FT limitations, data are studied in the frequency domain by the Continous Wavelet transform (WT), a powerful tool to characterize non stationary systems [61]. WT is a time-frequency analysis method which provides localized information in time and frequency domain simultaneously. The one-dimensional time series data are decomposed into a time-frequency plane allowing to determine the temporal evolution of the signal spectral content i.e. both spectral modes and how those modes vary in time. WT is a refined alternative to the classical windowed Fourier analysis, providing not only the representation of the spectral energy content of the signal at a certain time, but also the ability to adapt the resolution to the signal frequency. A wavelet is a smooth function $\Psi(t)$ with a compact support (or a rapid decay at infinity, contrary to the Fourier basis), and zero average,

$$\int_{-\infty}^{+\infty} \Psi(t)dt = 0$$

which is translated in time by d and dilated by a positive scale parameter s,

$$\Psi_{s,d}(t) = \frac{1}{\sqrt{s}}\Psi\left(\frac{t-d}{s}\right)$$

The zero average condition imply that $\Psi(t)$ is an oscillating function. The function $\Psi(t)$ is called a mother wavelet, the translated and dilated replicas $\Psi_{s,d}(t)$ are called daughter wavelets. The wavelet transform of a function of time t, $f(t)$, at the scale

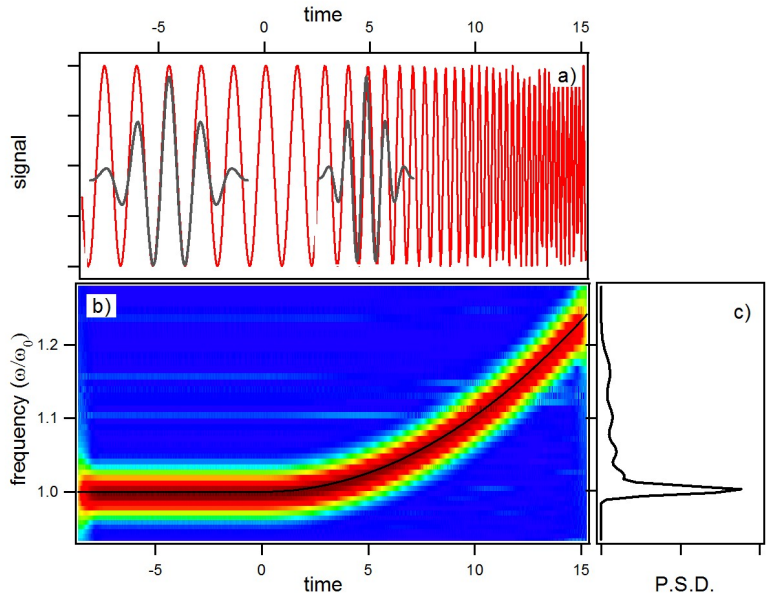

FIGURE 4.1: Comparison between the Fourier transform and the wavelet transform analysis. a) The time signal, a cosine function for negative times and a cosine with quadratic chirp for positive times. Two daughter wavelet functions are superposed to the signal. b) Wavelet Transform of the temporal trace represented in a) showing the evolution of the frequency. The white line is the calculated instantaneous frequency. c) Fourier Transform (Power Spectral Density) of the signal represented in a). Only an average of the signal frequencies is observed

s and delay d is computed by correlating $f(t)$ with the daughter wavelet at the corresponding scale and delay,

$$Wf(s,d) = \int_{-\infty}^{+\infty} f(t)\Psi^*_{s,d}(t)dt = \int_{-\infty}^{+\infty} f(t)\frac{1}{\sqrt{s}}\Psi^*\left(\frac{t-d}{s}\right)dt \qquad (4.1)$$

The wavelet transform coefficients $Wf(s,d)$ are "resemblance" coefficients, that measure the similitude between the signal and the wavelet atoms at various scales and delays.

The square modulus of the wavelet coefficients $|Wf(s,d)|^2$ is proportional to the local energy density of the signal at the given delay and scale, called the *scalogram* of the signal. As explained in detail below, the delay-scale representation in which wavelets are defined can be mapped into the more physical time-frequency

representation to describe the signal energy localization in frequency and time. It is useful to point out that the instantaneous frequency of the signal can be traced by the so called *wavelet ridges* analysis of the spectrogram in the time-frequency plane. The wavelet ridges are the maxima points of the normalized scalogram [61], showing the instantaneous frequencies within the limits of the transform's resolution.

To visualize the differences between the FT and WT consider an analytical signal $f(t) = a\cos\varphi(t)$ with time varying phase $\varphi(t)$, where $\varphi(t) = \omega_0(t)$ at negative times and $\varphi(t) = \omega_0 t + \alpha t^3$ at positive times (Fig. 4.1a). The instantaneous pulsation is the derivative of the phase $\omega(t) = \varphi^{'}(t)$ (the white line in Fig. 4.1b). Since FT is a time invariant operator, only an average of the time dependent spectrum is observed (Fig. 4.1c). On the other hand, WT approach combines the time domain and frequency domain analysis so that the evolution of each spectral component is determined. The wavelet analysis allows to extract accurately the instantaneous frequency information even for rapidly varying time series.

This chapter describes the method of wavelet analysis, includes a discussion of different wavelet functions and summarizes some examples of WT applications to demonstrate its usefulness in quantitative measurements.

4.2 Wavelet transform analysis

The WT approach adopts an analyzing function $\Psi(t)$ called *mother wavelet* as basis function [61, 62]. One thing to remember is that wavelet transforms do not have a single set of basis functions like the Fourier transform, which utilizes just the sine and cosine functions. Instead, wavelet transforms have an infinite set of possible basis functions. A function $\Psi \in L^2(R)$ is *admissible* as a wavelet basis if it has zero average

$$\int_{-\infty}^{+\infty} \Psi(t)dt = 0$$

Name	$\psi_0(\eta)$	$\hat{\psi}_0(s\omega)$	*e*-folding time τ_s	Fourier wavelength λ
Morlet (ω_0 = frequency)	$\pi^{-1/4} e^{i\omega_0\eta} e^{-\eta^2/2}$	$\pi^{-1/4} H(\omega) e^{-(s\omega-\omega_0)^2/2}$	$\sqrt{2}s$	$\frac{4\pi s}{\omega_0+\sqrt{2+\omega_0^2}}$
Paul (m = order)	$\frac{2^m i^m m!}{\sqrt{\pi(2m)!}}(1-i\eta)^{-(m+1)}$	$\frac{2^m}{\sqrt{m(2m-1)!}} H(\omega)(s\omega)^m e^{-s\omega}$	$s/\sqrt{2}$	$\frac{4\pi s}{2m+1}$
DOG (m = derivative)	$\frac{(-1)^{m+1}}{\sqrt{\Gamma\left(m+\frac{1}{2}\right)}} \frac{d^m}{d\eta^m}\left(e^{-\eta^2/2}\right)$	$\frac{-i^m}{\sqrt{\Gamma\left(m+\frac{1}{2}\right)}}(s\omega)^m e^{-(s\omega)^2/2}$	$\sqrt{2}s$	$\frac{2\pi s}{\sqrt{m+\frac{1}{2}}}$

$H(\omega)$ = Heaviside step function, $H(\omega) = 1$ if $\omega > 0$, $H(\omega) = 0$ otherwise.
DOG = derivative of a Gaussian; $m = 2$ is the Marr or Mexican hat wavelet.

FIGURE 4.2: Three wavelet basis functions and their properties. Constant factors for Ψ_0 and $\hat{\Psi}_0$ ensure a total energy of unity.

and therefore if it is oscillatory. Moreover an admissible function must be localized in both time (unless the Fourier basis) and frequency space i.e. must have a band-pass like spectrum. In other word, $\Psi(t)$ must be a *wave*. A wavelet function is normalized $\|\Psi\| = 1$ and centered in the neighborhood of $t = 0$. The wavelet basis function is chosen according to the application to be analyzed. In choosing the wavelet function, there are several factors which should be considered.

1) Complex or real. A complex wavelet function will return information about both amplitude and phase and is better adapted for capturing oscillatory behavior. A real wavelet function returns only a single component and can be used to isolate peaks or discontinuities.

2) Width. The width of a wavelet function is defined here as the wavelet amplitude in time domain. The resolution of a wavelet function is determined by the balance between the width in real space and the width in Fourier space. A narrow (in time) function will have good time resolution but poor frequency resolution,

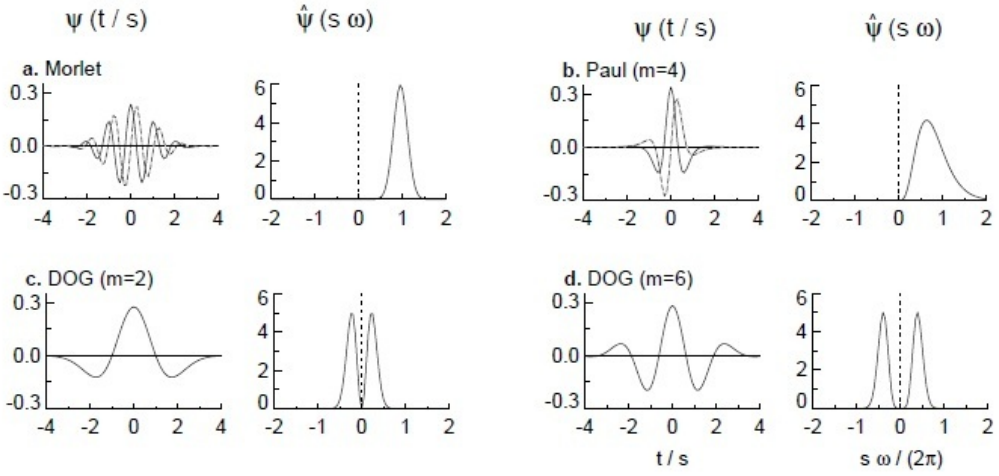

FIGURE 4.3: Four different wavelet bases. The plots on the left give the real part (solid) and imaginary part (dashed) for the wavelets in the time domain. The plots on the right give the corresponding wavelets in the frequency domain. For plotting purposes, the scale was chosen to be s = 10dt. (a) Morlet or Gabor, (b) Paul (m = 4), (c) Mexican hat (DOG m = 2), and (d) DOG (m = 6)

while a broad function will have poor time resolution, yet good frequency resolution.

3) Shape. The wavelet function should reflect the type of features present in the time series. For time series with sharp jumps or steps, one would choose a boxcar-like function such as the Harr, while for smoothly varying time series one would choose a smooth function such as a damped cosine.

Four common nonorthogonal wavelet functions are given in Fig. 4.2. The Gabor and Paul wavelets are both complex, while the DOGs are real valued. Pictures of these wavelet in both the time and frequency domain are shown in Fig. 4.3. Many other types of wavelets exist, such as the Haar and Daubechies, most of which are used for orthogonal wavelet analysis. Here we choose a complex Gabor wavelet (also called Gaussian wavelet) as the mother wavelet, because it has the least spread in both frequency and time domain and thus the best time-frequency

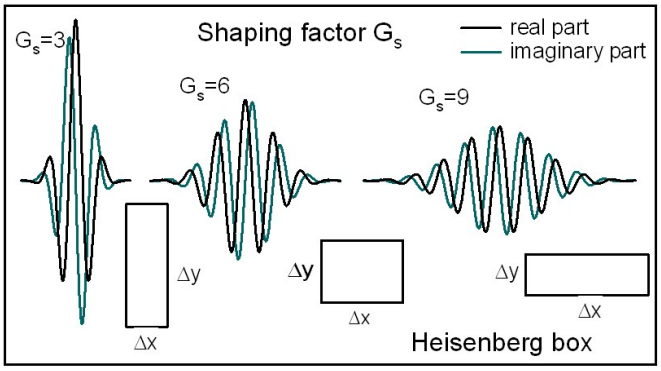

FIGURE 4.4: Complex Gabor wavelet with different shaping factors. An increase of G_S corresponds to more oscillations. The "Heisenberg box" depicts the relationship between the time and frequency resolution, like the uncertainty principle in quantum mechanics (adapted from Ref. [63])

resolution. The Gabor wavelet consists of a plane wave modulated by a Gaussian

$$\Psi(t) = \frac{1}{(\sigma^2\pi)^{1/4}} e^{\frac{t^2}{2\sigma^2} + i\eta t}$$

Here σ controls the amplitude of the Gaussian envelope, η the carrier frequency. The shape of the mother Gabor wavelet is characterized by a single dimensionless parameter called the Gabor shaping factor $G_S = \sigma\eta$ [63], which takes in to account the envelope width (temporal resolution) and the number of oscillations within the envelope width (frequency resolution) (Fig. 4.4). An increase of G_S means more oscillations under the wavelet envelope and a larger time spread, the frequency resolution being improved and the time resolution degraded.

A family of time-frequency atoms is obtained by dilations and translations of a mother wavelet $\Psi(t)$ as

$$\Psi_{s,d}(t) = \Psi\left(\frac{t-d}{s}\right)$$

where d is the delay and s the adimensional scale parameter. The generated functions $\Psi_{s,d}(t)$ are called daughter wavelets (Fig. 4.5). These atoms remain normalized $\|\Psi_{s,d}\| = 1$ to have unit energy. The wavelets dilation sets by the scale

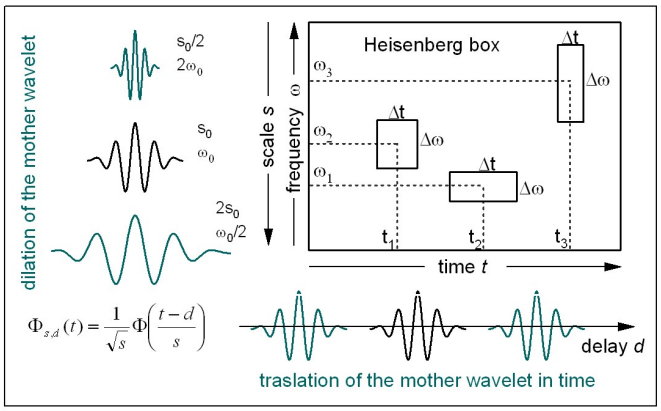

FIGURE 4.5: The daughter wavelets generated by dilations and translations of a mother wavelet. The Heisenberg box is determined by the shaping factor of the mother wavelet G_S and the scaling parameter s of the daughter wavelet (adapted from [64])

parameter s is directly related to the frequency. The wavelet angular frequency at scale s is given by $\omega_s = \eta/s$ [65]. The associated frequency is $f_s = \omega_s/2\pi$.

The continuous wavelet transform of a signal $f(t)$ is expressed as the convolution of the signal with a daughter wavelet, see Eq. 4.1 which we rewrite herein:

$$Wf(s,d) = \int_{-\infty}^{+\infty} f(t)\Psi^*_{s,d}(t)dt = \int_{-\infty}^{+\infty} f(t)\frac{1}{\sqrt{s}}\Psi^*\left(\frac{t-d}{s}\right)dt$$

By varying the wavelet scale s and translating along the localized time axis that means delaying by d, one can construct a time frequency representation showing both the amplitude of the spectral content and how this amplitude varies with time. Because the wavelet function $\Psi(t)$ is in general complex, the wavelet transform coefficients $Wf(s,d)$ are also complex. The transform can then be divided into the real part, $\mathbf{Re}\ \{Wf(s,d)\}$, and imaginary part, $\mathbf{Im}\ \{Wf(s,d)\}$, or amplitude, $|Wf(s,d)|$, and phase, $\angle Wf(s,d)$. Finally, the square modulus of the wavelet coefficients $|Wf(s,d)|^2$, called the *scalogram*, represents the local time-frequency energy density of the signal within the limit of the wavelet transform resolution. For real-valued wavelet functions such as the DOGs (derivatives of a Gaussian) the imaginary part is zero and the phase is undefined.

4.3 Instantaneous frequency

A cosine modulation

$$f(t) = a\cos(\omega_0 t + \phi_0) = a\cos(\phi(t))$$

has a frequency ω_0 that is the derivative of the phase $\phi(t) = \omega_0 t + \phi_0$ [61]. To generalize this notion, real signals f are written as an amplitude a modulated with a time varying phase ϕ:

$$f(t) = a(t)\cos(\phi(t))$$

with $a(t) > 0$. The instantaneous frequency is defined as a positive derivative of the phase

$$\omega(t) = \phi'(t) \geq 0$$

The time variation of several instantaneous frequencies can be measured with time-frequency decompositions. The WT coefficients are *resemblance* coefficients, that measure the similarity between the signal and the wavelet function at various delays and scales. The WT compares the signal with the daughter wavelet (Fig. 4.1a). When the period of a daughter wavelet is the same as or the closest to that of the signal, the WT amplitude reaches the maximum at that time and frequency position. Considering the time t, the scalogram is maximum at frequency

$$\frac{\eta}{s}(t) = \omega(t) = \phi'(t)$$

The corresponding points $(t, \omega(t))$ are called *ridges* and the instantaneous frequency is traced by the *wavelet ridges* analysis of the spectrogram in the time-frequency plane as shown in Fig. 4.1b. In other word, the wavelet ridges are the maximum points of the normalized scalogram [61, 66], representing the instantaneous frequencies within the limits of the transform resolution. When the signal contains several spectral lines whose frequencies are sufficiently apart, the wavelet transform separates each of these components and the ridges detect the evolution

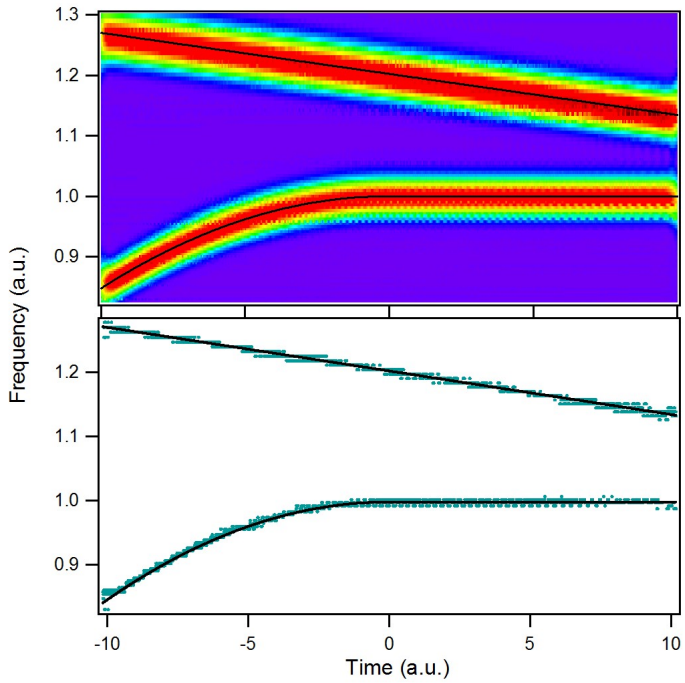

FIGURE 4.6: Wavelet transform of a signal that includes a linear chirp whose frequency decreases and a quadratic chirp whose frequency increases. The green points are the ridges calculated from the time-frequency topography. The black lines display the instantaneous frequency of the linear and quadratic chirp calculated mathematically. The ridges discriminates the instantaneous frequency of the two spectral components.

in time of each spectral component [61]. Let us consider

$$f(t) = a_1(t)\cos(\phi_1(t)) + a_2(t)\cos(\phi_2(t))$$

Sufficiently apart means that the difference between the instantaneous frequency of the two components ($|\phi_1'(t) - \phi_t'(t)|$) is larger than the wavelet atom bandwidth. Then the ridge points are distributed along two time-frequency lines $\omega(t) = \phi_1'(t)$ and $\omega(t) = \phi_2'(t)$. Fig. 4.6 refers to a signal that includes a linear chirp whose frequency decreases and a quadratic chirp whose frequency increases. The two components are sufficiently separated to be extracted by ridges analysis. This results is valid for any number of time varying spectral components, as long as

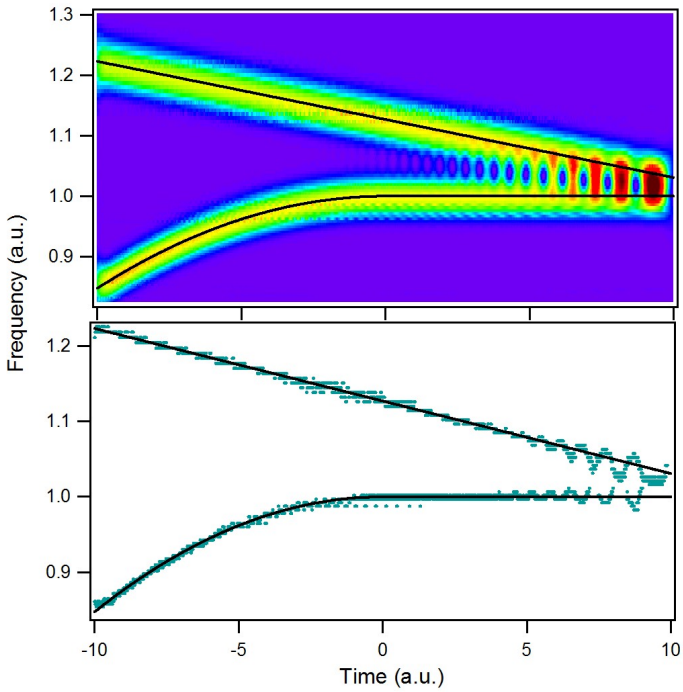

FIGURE 4.7: Wavelet transform of a signal that includes a linear chirp whose frequency decreases and a quadratic chirp whose frequency increases. The green points are the ridges calculated from the time-frequency topography. The black lines display the instantaneous frequency of the linear and quadratic chirp calculated mathematically. The interference of the two spectral components destroys the ridge pattern.

the distance between any two instantaneous frequencies exceeds the frequency resolution of the wavelet atom. If two spectral lines are too close, they interfere, which destroys the ridge pattern (Fig. 4.7).

4.4 Time-frequency resolution

Time and frequency energy concentrations are restricted by the Heisenberg uncertainty principle. This principle has a particularly important interpretation in quantum mechanics that the energy and frequency uncertainty cannot be reduced arbitrarily. In signal processing, the uncertainty principles sets that the time reso-

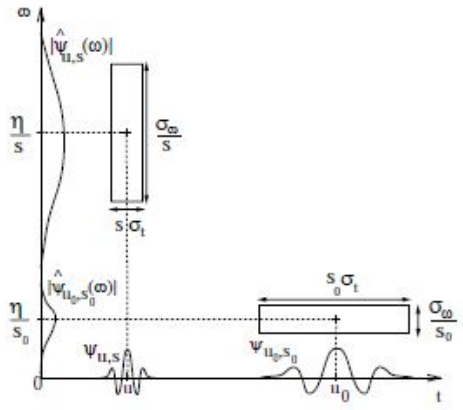

FIGURE 4.8: Heisenberg boxes of two wavelets. Smaller scales decrease the time spread but increase the frequency support, which is shifted towards higher frequencies.

lution and the frequency resolution cannot be improved simultaneously. When the time resolution is improved, the frequency resolution degrades. Likewise, when the frequency resolution is improved, the time resolution degrades. The basis function must therefore be adjusted as a trade-off between both accuracies [61, 67].

The time-frequency resolution of the WT is limited by the time-frequency resolution of the corresponding atoms. Using a mother wavelet implies an uncertainty both in time and frequency. In the time-frequency space this uncertainty is represented as a box, called the Heisenberg box, one dimension denoting the time resolution Δ_t, the other the frequency resolution Δ_ω, the area of the Heisenberg box $\Delta_t\Delta_\omega$ being constant. In signal processing the Gabor wavelets have a minimum joint time-frequency localization. Its Heisenberg box is determined by the σ parameter, giving a time resolution $\Delta_t = \sigma/\sqrt{2}$ and an angular frequency resolution $\Delta_\omega = 1/(\sqrt{2}\sigma)$, associated to the frequency resolution by $\Delta_f = \Delta_\omega/2\pi$.

When the wavelet is subject to a scale dilatation s, the corresponding Heisenberg box centered at time t and frequency $f_s = \omega_s/2\pi$ has size $\Delta_{s,t} = s\Delta_t$ along time and $\Delta_{s,\omega} = \Delta_\omega/s$ along frequency (see Fig. 4.5). As expected from the uncertainty principle, the area of the rectangle $\Delta_{s,t}\Delta_{s,\omega}$ remains equal to that of the

mother wavelet at all scales i.e. $\Delta_{s,t}\Delta_{s,\omega} = \Delta_t\Delta_\omega = 1/2$.

In order to appreciate the different time-frequency resolutions imposed by the parameters choice, three model signals, a temporal delta function, a square pulse and a sinusuoid, are transformed using two different Gabor mother wavelets ($\sigma = \sqrt{3/2}$, $\eta = 9\pi$ and $\sigma = \sqrt{3/4}$, $\eta = 4.5\pi$) (Fig. 4.9). A delta-like signal is completely localized in time and has a spectral content uniformly spread over all frequencies. The time spread of the scalogram at each frequency is then determined only by the time resolution of the wavelet. Small values of G_S improve the time resolution whereas increasing the scaling factor s (and then decreasing the frequency at which the Heisenberg box is centered) implies a smaller time localization (Fig. 4.9a-b). This is true also considering the edge effects caused by a square function whose temporal amplitude is equal to the wavelet transform time window. In this case only half of the Heisenberg box centered at the time interval boundaries falls into the scalogram (Fig. 4.9c-d). A sinusoid signal is completely localized in frequency domain and spread in time domain. The wavelet transform of a sinusoid function is a line centered at the oscillation frequency whose frequency spread is determined by the frequency resolution of the wavelet transform. Higher Gabor shaping factor G_S means higher frequency resolution (Fig. 4.9e-f). Note that the edge effects, due to the truncation of the sinusuoid by the finite transform time window, are consistent with the previous example.

The frequency resolution of wavelet atoms is proportional to $1/s$ and then to $\omega = 2\pi f$ in such a way that the bandwidth-to-frequency ratio $\Delta_{s,f}/f_s$ is constant, as illustrated in Fig. 4.5 and Fig. 4.8. This means that the frequency resolution of the wavelet scalogram is higher at low frequencies but coarser at higher frequency. This is an important improvement of wavelet transform with respect to windowed Fourier transform whose frequency support remains constant at all frequency [61, 62, 67]. The widowed Fourier transform is a time-frequency analysis which correlates the signal with sliding blocks obtained by multiplying the sines and cosines (waves) by a sliding window localized in time. The main problem is

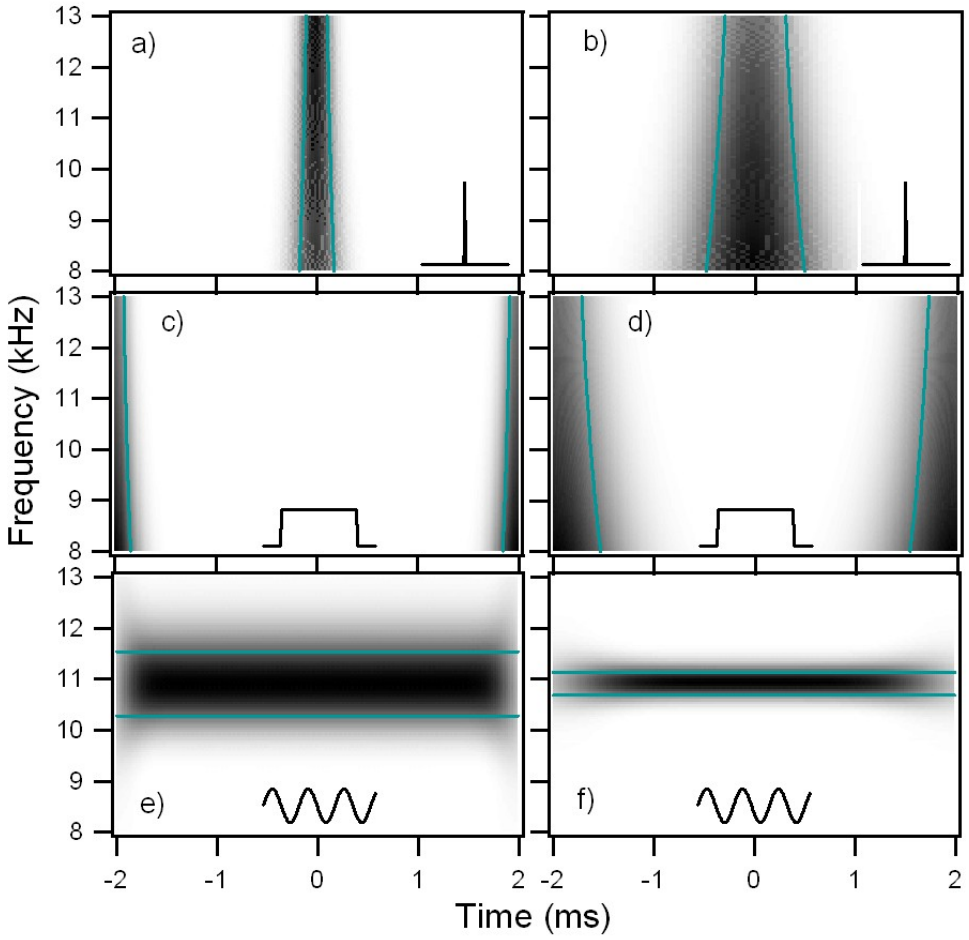

FIGURE 4.9: Wavelet transform of three model signals using two different mother wavelets (on the left $G_S = 12$, on the right $G_S = 35$). a-b) WT of a delta-like function. The time spread is only due to the wavelet resolution in time $\Delta_{s,t}$. It is proportional to the scaling factor s then it decreases as the frequency increases. c-d) WT of a square function. The time spread at the edges due to the wavelet resolution in time is $\Delta_{s,t}/2$, decreasing with frequency. e-f) WT of a cosinusoid function. The frequency spread depends on the mother wavelet used. The lines are the calculated time (a-d) and frequency (e-f) accuracy

that the blocks do not depend on the frequency to be analyzed so that relative resolution at high frequency degrades significantly.

One way to see the time-frequency resolution differences between the win-

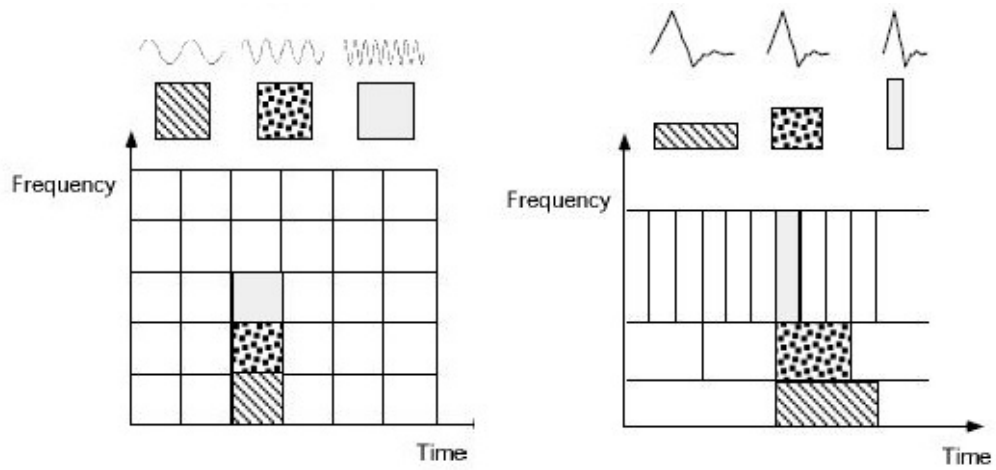

FIGURE 4.10: Windowed Fourier basis functions (left) and Daubechies wavelet basis functions (right) time-frequency tiles and coverage of the time-frequency plane.

dowed Fourier transform and the wavelet transform is to look at the basis function coverage of the time-frequency plane [67]. Fig. 4.10 shows a windowed Fourier transform performed by using simply a square wave as window. Because the same window is used for all frequencies, the resolution of the analysis is the same at all locations in the time-frequency plane, limiting its applicability. For instance, the hyperbolic chirp

$$f(t) = cos\left(\frac{\alpha}{\beta - t}\right)$$

has instantaneous frequency

$$\phi'(t) = \frac{\alpha}{(\beta - t)^2}$$

which goes from 0 to $+\infty$ in a finite interval. The instantaneous frequency of hyperbolic chirps cannot be estimated by a windowed Fourier transform because for any fixed window size, the instantaneous frequency varies too quickly at high frequencies, see Fig. 4.11.

An advantage of wavelet transforms is that the windows vary proportionally with the frequency. In order to isolate signal discontinuities, one would like to have

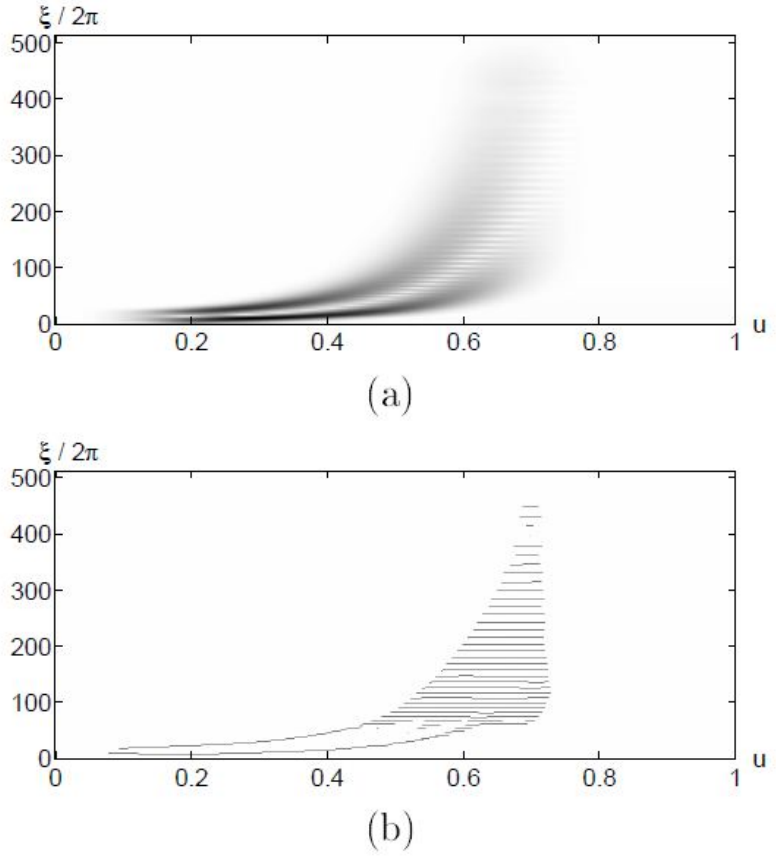

FIGURE 4.11: Sum of two hyperbolic chirps. a) Windowed Fourier transform b) Ridges calculated from the spectrogram in a).

some very short basis functions. At the same time, in order to obtain detailed frequency analysis, one would like to have some very long basis functions. A way to achieve this is to have short high-frequency basis functions and long low-frequency ones. This is exactly what wavelet transforms provide. Fig. 4.10 shows the coverage in the time-frequency plane with one wavelet function, the Daubechies wavelet. The wavelet ridges are able to follow also the rapid time modification of the instantaneous frequencies of hyperbolic chirps. This is particularly useful to analyze the return signals of hyperbolic chirps emitted by radars or sonars [61]. The response can be detected at all frequencies with adapted resolution. Therefore WT can accurately extract the instantaneous frequency also of signal with rapid

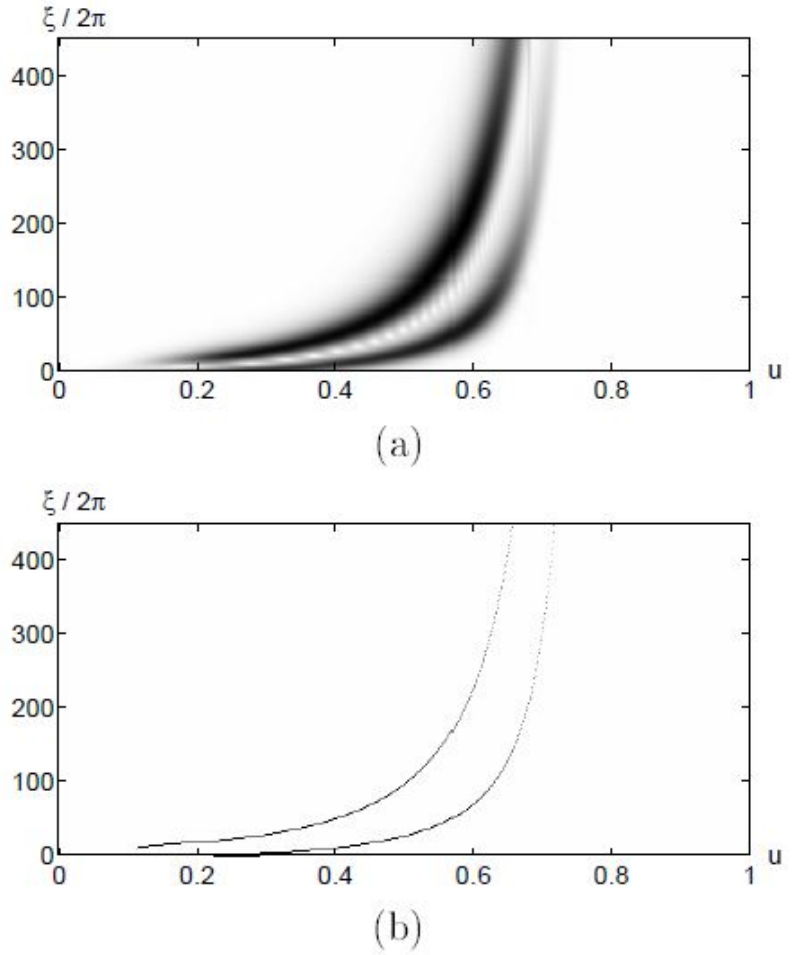

FIGURE 4.12: Normalized scalogram of two hyperbolic chirps. b) Wavelet ridges.

and wide spectral variation.

4.5 Applications of wavelet transform

Wavelets have been used in a number of application in different fields of science and technology to extract information from and/or denoise many different kinds of data, including - but certainly not limited to - audio signals, images, optical spectra, time series. Previously, wavelet analysis have been used in atomic force spectroscopy mainly to denoise or extract data from images [68, 69], which is by

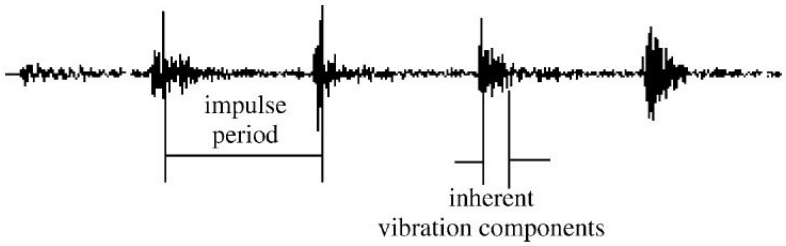

FIGURE 4.13: Time course of roller bearing vibration signal with typical local fault

far the most important application of the wavelet transform. Moreover, thanks to its character of reflecting the localized information in time and frequency, WT can be applied in vibration signal analysis in transient regimes.

In [70] the time-energy density methods is used to efficiently extract the fault characteristics of a roller bearing. The high frequency vibrations caused by local fault of the rotating roller bearing can excite a resonance response of the system. The excitation force due to the fault activates a non stationary response 4.13. Since the forces induced by the fault act for a short time lapse, the steady-state roller bearing vibrations signals display an abrupt change due to huge vibrations at the resonant frequency from the roller bearing which attenuate rapidly because of damping. The vibration signal of roller bearing with fault is then modulated by an impulsive force so that the fault characteristic frequency cannot be defined by FT analysis. On the contrary, the time-energy density analysis based on WT easily extract the position of the fault characteristic frequency in case of roller bearing with both outer-race and inner-race fault.

The WT approach is a efficient tool also to estimate damage location in a simply-supported solid beam [65]. The beam is excited by the impact of a dropped steel ball, that generates bending waves exploited to localized the position of a small crack artificially created between the impact point and the free end. If the bending wave is measured between the impact point and the crack, the signal contains the initial propagating wave and a small wave reflected by the damage. The

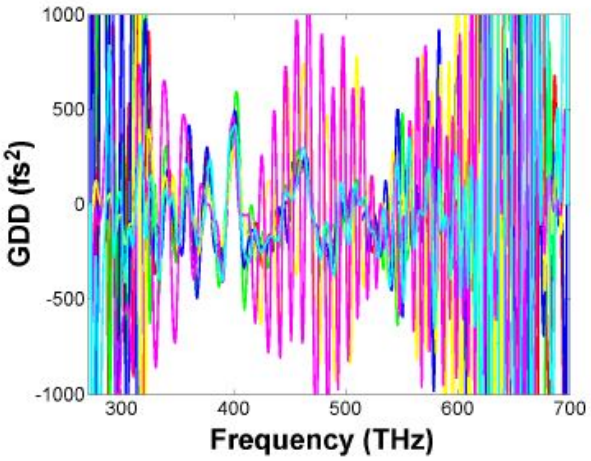

FIGURE 4.14: Extracted group delay dispersion from the double differentiations of phases extracted from a Fourier transform technique.

difference in the arrivals time of the propagating wave and the reflected wave allows to estimate the crack location. The bending waves have frequency-dependent group velocity which has to be considered. This is performed by WT ridges analysis delivering an accurate measurement of the damage location.

Moreover, WT analysis is used to extract group delay (GD) and group delay dispersion (GDD) from white light spectral interferograms [66, 71]. In conventional approaches, GD is obtained by differentiation of the phase extracted by FT technique. The measured GD displays additional oscillation structures mainly introduced by the noise of the phase differentiation. In GDD extraction that takes double differentiations this effect is more dramatic. The noise level induced by differentiation is so high that the GDD is difficult to extract, see Fig. 4.14. The joint time-frequency analysis with WT technique allows to directly extract the GD from the spectral interferogram by ridges analysis. Then differentiation noise effect are greatly reduced. GD and GDD are more precisely measured. The improvement of GDD estimation by wavelet analysis is shown in Fig. 4.15

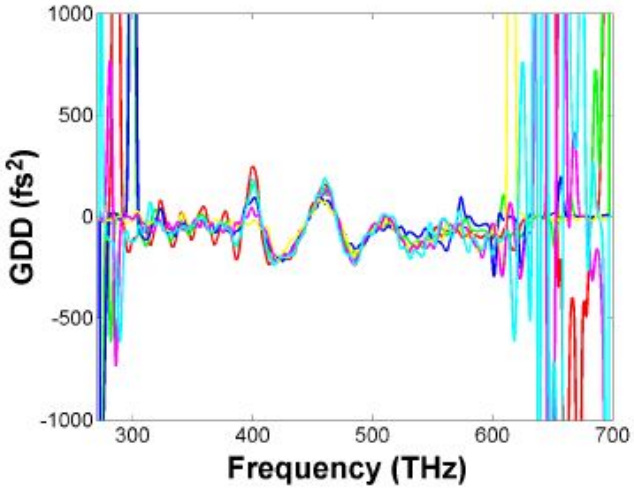

FIGURE 4.15: Extracted group delay dispersion from the ridges of wavelet-transform for the spectral interferograms.

4.6 Summary

Fourier theory states that a signal can be expressed as the sum of a, possibly infinite, series of sines and cosines, referred to as a Fourier expansion. The big disadvantage of a Fourier expansion however is that it has only frequency resolution and no time resolution. This means that although we might be able to determine all the frequencies present in a signal, we do not know when they are present. The wavelet transform or wavelet analysis is probably the most common solution to overcome the shortcomings of the Fourier transform. Wavelet analysis adopts scalable functions as basis. They are shifted along the signal and for every position the spectrum is calculated. The result is a time-frequency representations of the signal. The wavelet basis is not unique but has to be carefully choose depending on the signal characteristics. Then the instantaneous frequency can be evaluated by wavelet ridges, the maximum points of the time-frequency representation.

The wavelet transform resolution is limited by the Heisenberg's uncertainty principle, which, in signal processing terms, states that it is impossible to know the exact frequency and the exact time of occurrence of this frequency in a signal.

In other words, a signal can simply not be represented as a point in the time-frequency space but as the energy density contents into the Heisenberg box.

Wavelet transform approach has been successfully exploited in many field of physics and engineering providing quantitative measurements. This induced us to apply the wavelet time-frequency analysis in AFM force spectroscopy.

Chapter 5

The experiment

The experiments is performed by monitoring the cantilever thermal fluctuations with an AFM based on the optical beam deflection detector. The custom acquisition system collects the photodiode signal by an external digitizing oscilloscope. In this chapter we describe the experimental set-up and the procedure to calibrate the cantilevers spring constant.

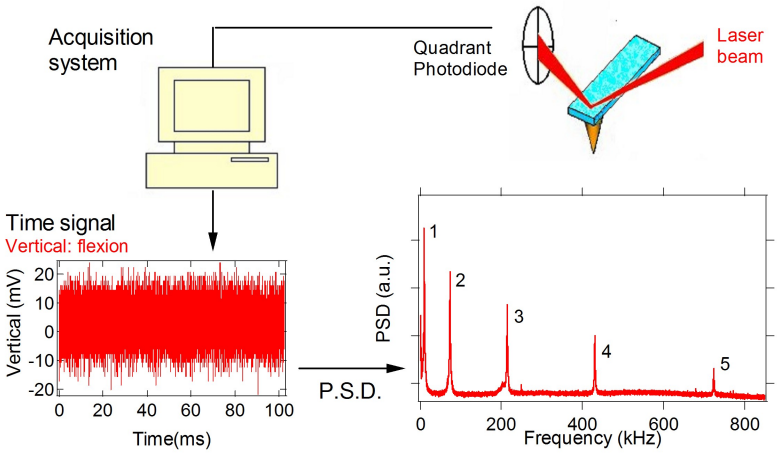

FIGURE 5.1: Block diagram of the optical beam detection system. The power spectral density is provided by the thermal vertical signal of the free cantilever.

5.1 Introduction

The experiments consists in measuring the tip-sample interaction through the analysis of the thermally excited cantilever fluctuations in the vicinity of the sample. In both cases the sample is a freshly cleaved highly oriented pyrolitic graphite (HOPG) surface in ambient condition. The experiment is performed in two phases. First long-range van der Waals force are probed in stationary regime and the data processed by Fourier transform analysis. Then, to reduce the acquisition time, the measurement is performed in dynamic regime i.e. transient regime and the tip-sample force is inferred by wavelet transform analysis of the time signal. In this case both long- and short-range interactions are probed

5.2 Experimental set-up

Fig. 5.1 schematically shows the experimental apparatus. The experiment is performed with an AFM [72] (Fig. 5.2) suitable for static and dynamic (amplitude modulation) operation modes. The AFM resides on a massive platform suspended

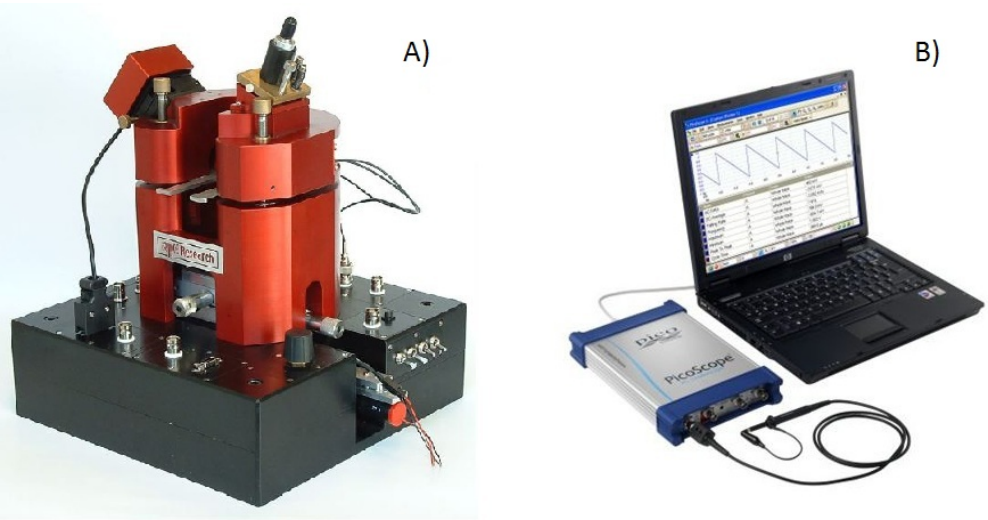

FIGURE 5.2: A) APE Research Atomic Force Microscope. B) Picoscope PC Oscilloscope 5402

by springs to provide isolation from external mechanical noise. The system is inside an isolation box to provide thermal and acoustic shielding. The head houses the cantilevers holder which can be removed to easy mount the cantilever. The piezoscanning system is based on a single scanner tube with a maximum vertical extension of 2 μm.

The cantilever deflection is monitored by a standard optical beam deflection system based on a 600 nm laser diode coupled to a monomode fiber (with a mode field diameter of 4μm), which acts as a mode filter, giving a TEM00 beam output after recollimation. The collimated fiber output is focalized with an aspherical lens to a 10 μm spot on the cantilever end. A four quadrant silicon diode monitors the cantilever flexural deflection (vertical signal provided by the top-bottom differential output) and its torsion (lateral signal provided by the left-right differential output). The overall bandwidth of the optical lever deflection system exceeds 1 MHz.

The scanner and the data acquisition are driven by a Control Unit equipped with a multi input-output board that allows to easy collect the photodiode outputs

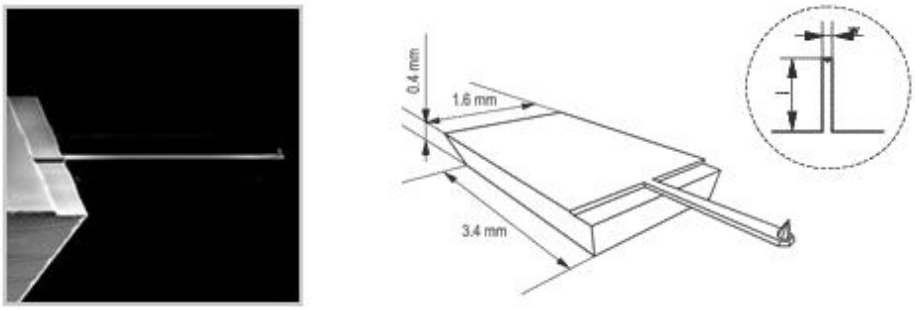

FIGURE 5.3: Left: SEM image of the Silicon cantilever and probe. Right: Schematic diagram of the probe chip.

by a digitizing oscilloscope (PicoScope 5204 PC oscilloscope 5.2 [73]) devised for high-speed data acquisition and digitize signals with 8 bit vertical resolution and minimal distortion. Its 250 MHz analog bandwidth is complemented by a real-time sample rate of 1 GS/s. The 128 megasample buffer memory ensures that complex waveforms can be captured at the full sampling rate. A USB cable connects the PicoScope to the PC where data are stored in real time.

The sample consisted of a freshly cleaved highly oriented pyrolitic graphite (HOPG) surface. The experiments are conducted in air, with a relative humidity of less than 50%. No external driving force is applied to cantilever whose vibrations are activated only by thermal exchanges with the local environment.

The experiments are performed using μmasch CSC17 [74] rectangular cantilevers whose nominal dimensions are $50 \times 460 \times 2\mu\text{m}^3$, the resonance frequency f_1=12 kHz and the elastic constant k=0.15 N/m, see Fig. 5.3.

Before performing the measurements of the tip-sample interaction, the calibration of the optical lever sensitivity (deflection sensitivity calibration) of the instrument is performed on the hard HOPG surface. The cantilever bending is monitored by the differential vertical output current from the quadrant photodiode, which is correlated with the calibrated piezotube extension. The deflection calibration is done while the tip is in contact with the hard HOPG surface by assuming a negligible indentation and thus equal distances spanned by the can-

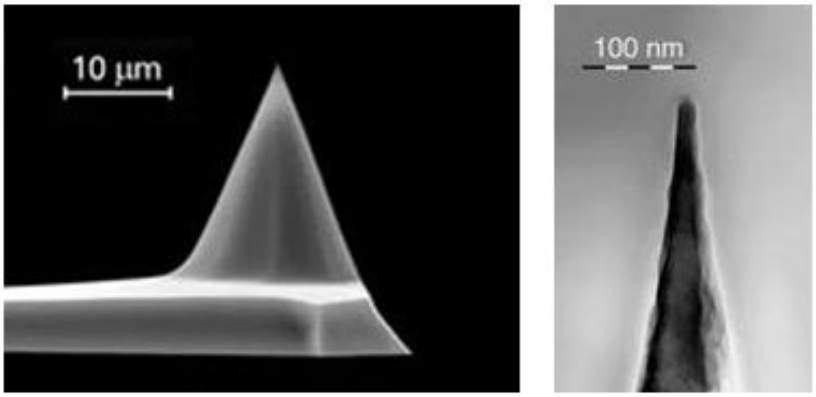

FIGURE 5.4: Left: SEM image of the uncoated SPM Silicon probe tip. Right: SEM micrograph of Silicon etched probe tip end.

tilever tip and the piezotube. The obtained sensitivity is in the range of 50-200 nm/V, depending on the cantilever type, beam position, and laser light power level. Since the laser beam position influences the effective length of the cantilever and the sensitivity, care has been taken during the measurements regarding the stability of laser alignment. The cantilever 15° tilt with respect to sample surface is considered for sensitivity correction [26].

5.3 The cantilevers spring constant

The n-type silicon (phosphorus doped) etched probe tip has a conical shape with full cone angle of 40° as shown in Fig. 5.4. The total tip height is 20-25 μm and the typical probe tip radius $R = 10$ nm. By measuring the plan view dimensions of many cantilever from CSC17 series by an optical microscope we obtained a mean width of approximately 40μm, a value which is 20% less than the nominal value. On the contrary, the measured mean length (460 μm) agrees with the value declared by the manufacturer.

The rectangular cantilever displays different oscillation modes (Fig. 5.5): flexural, torsional and lateral oscillations. In all cases the system can be modeled as a damped oscillator whose spectral response is a Lorentzian function, see Sec. 3.2.

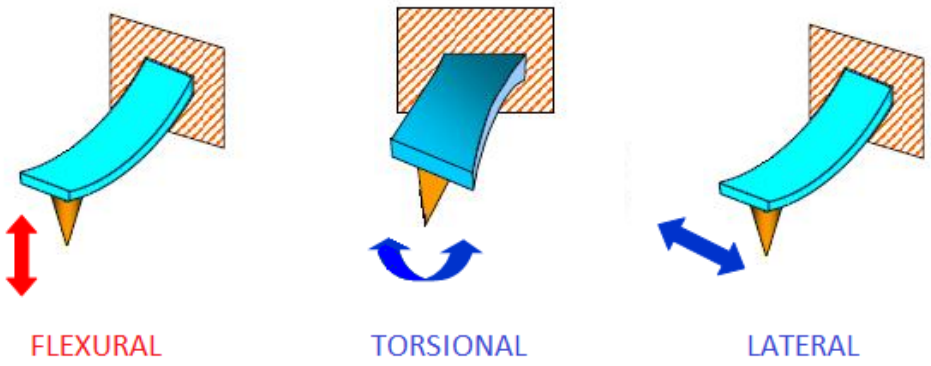

FIGURE 5.5: Oscillation modes of the rectangular cantilever: flexural, torsional and lateral.

The cantilever elastic constants can be estimated by measuring its spectral behavior. In fact, the cantilever spring constant can be calibrated by two different procedures: the Sader method [75] and the thermal noise method [41, 50]. The Sader methods relies solely on the measurement of the cantilever plan view dimensions (length L and width w), the resonant frequency f_0 and quality factor Q of the cantilever oscillation and the knowledge of the density and viscosity of the fluid in which these are measured (typically air). In case of rectangular cantilever the elastic constant is provided by [75]:

$$k = 0.1906 \rho_f w^2 L Q \omega_0^2 \Gamma_i(\omega_0) \tag{5.1}$$

ρ_f is the density of the fluid in which the measurement is taken (typically air), ω_0 the fundamental mode resonant angular frequency, Γ_i is the imaginary component of the hydrodynamic function, which is available on Sader website with a Java applet to perform the elastic constant calculation [76]. The resonance frequency $f_0 = \omega_0/2\pi$ and Q of the cantilever are measured by performing a power spectral density analysis of the cantilever thermally driven oscillations. The resonance peak is then fitted with the simple harmonic oscillator (SHO) model:

$$A(\omega) = A_{white} + \frac{A_0}{\sqrt{(\omega_0^2 - \omega^2)^2 + (\omega\omega_0/Q)^2}}$$

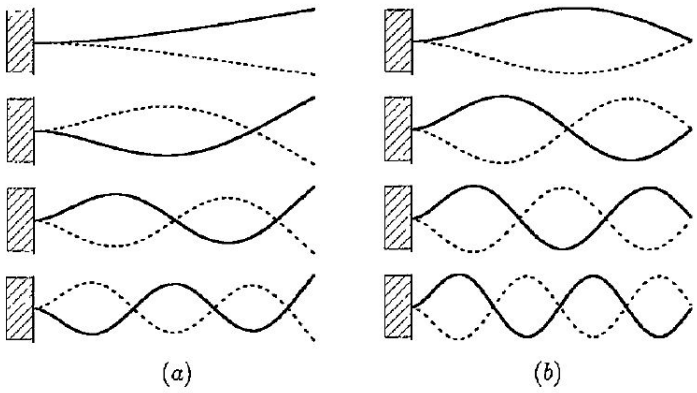

FIGURE 5.6: Shape of the first four vibrations modes of a free (a) and supported (b) cantilever.

where A_{white} is a white noise fit baseline accounting for the electronic white noise. The parameters A_{white}, A_0, $\omega_0 = 2\pi f_0$ and Q are fitted to the PSD data using a least-squares procedure implemented in MatLab code [77].

An alternative calibration method is the thermal tune method based on modeling the cantilever as a rectangular bar with a fixed end [41, 50, 78]. Making use of the equipartition theorem, the thermal (i.e. Brownian) motion of the cantilever oscillation is related to the thermal energy k_BT. The beam theory explicitly considers the actual bending modes of the cantilever (Fig. 5.6) and therefore the energy of all the oscillatory modes. Moreover, the cantilever displacement as measured by the optical lever detection scheme is different from the actual displacement of the cantilever because it is proportional to angular changes in the cantilever position, not its absolute deflection and these angular changes depend on the bending mode of the cantilever. Then, considering only a single bending mode i, the cantilever elastic constant is evaluated by:

$$k = \frac{16k_BT}{3\alpha_i^2 \left\langle z^{*2} \right\rangle} \left(\frac{\sin \alpha_i \sinh \alpha_i}{\sin \alpha_i + \sinh \alpha_i} \right)^2$$

Here $\left\langle z^{*2} \right\rangle$ is the mean square virtual cantilever displacement i.e. the mean square displacement as measured by the optical lever scheme. By the Parsival's relation $\left\langle z^{*2} \right\rangle$ can be estimated in the frequency domain allowing to subtract the white noise

		free flex.					clamped flex.	
	mode	1	2	3	4	5	1	2
FT	f_n (kHz)	10.757	74.28	215.1	431.3	724	69.23	200.81
	Q_n	58	170	290	420	530	17	89
	f_n/f_1 exp.		6.90	20.0	40.1	67	6.43	18.7
WT	f_n (kHz)	10.908	76.09	222.6	444.4		62.80	195.7
	Q_n	63	180	320	470		32	89
	f_n/f_1 exp.		6.97	20.4	40.7		5.75	17.9
	f_n/f_1 teo.		6.26	17.5	34.4	56.8	4.38	14.2

TABLE 5.1: Free and clamped cantilever flexural resonant frequencies and quality factors for the cantilever used in the FT and WT approaches. The measured ratio between the frequencies of the higher modes with the first one is compared with the theoretical prediction [41].

background contribution, see Sec. 6.4 and [79]. The coefficients α_i as determined by the boundary conditions are tabled in [41] both for free and supported cantilever end. In particular, for the first two flexural modes for the free cantilever:

$$\alpha_1 = 1.88 \text{ and } k = 0.82\frac{k_B T}{\langle z^{*2}\rangle} \tag{5.2}$$

$$\alpha_2 = 4.69 \text{ and } k = 0.25\frac{k_B T}{\langle z^{*2}\rangle} \tag{5.3}$$

In the following, we present the results of spring constant calibration performed on the two cantilever used for the tip-sample interaction measurements in both FT and WT approaches. The two μmasch CSC17 cantilevers came from the same batch.

As previously seen, the procedure to calibrate the cantilever spring constant requires to detect the PSD of the free cantilever. The photodiode signal is collected while the cantilever thermally oscillates far from the surface. Then the power spectral density (PSD) is calculated off line and averaged over 90 temporal traces of

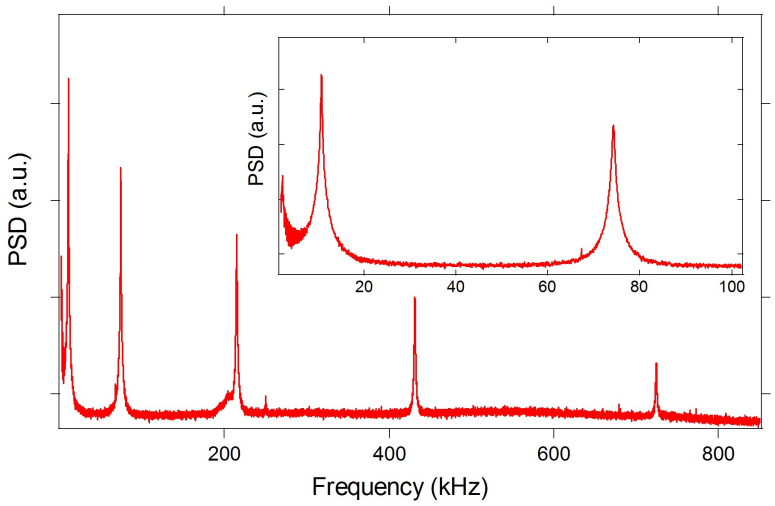

FIGURE 5.7: Power Spectral density of the free flexural modes for the cantilever used in the FT approach. The inset zooms on the two lower modes.

$1 \cdot 10^6$ samples each, acquired at 1MHz. Fig. 5.7 displays the PSD of the cantilever used to evaluate the tip-sample interaction by the FT approach, see Chap. 6. The electronic white noise level is small enough to observe the resonances up to the fifth flexural mode. The resonance peaks are fitted by a Lorentzian function providing the resonant frequencies f_0 and quality factors Q in Tab. 5.1.

When the tip is in contact with the sample, the cantilever still thermally oscillates but with modified flexural modes of oscillation (supported cantilever, see Fig. 5.6). The changed boundary conditions shift the resonance frequencies and increase the energy dissipation effects giving rise to a decrease of the quality factors (Tab. 5.1). The measured resonant frequencies compare well with theory for both free and supported cantilever [41]. The fitting parameters f_0 and Q and the measured plan views dimensions provide the elastic constant k=0.12 N/m as evaluated with the Sader method. The thermal tune method applied to both the first and second flexural modes gives k values that agree within 5%.

The same measurements are performed to calibrate the elastic constant of the cantilever used in the WT approach (Chap. 7). Fig. 5.8 shows the PSD referred

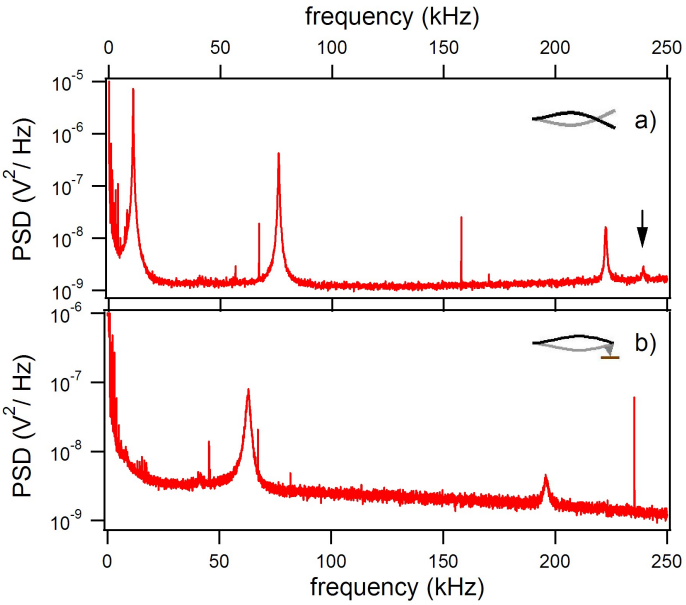

FIGURE 5.8: a) Thermal PSD of the flexural fluctuations zoomed on the three lower modes for the cantilever used in the WT approach. The arrow points at the first torsional mode. b) Same as a) but with the tip in contact with the sample at constant negative load (F≈ -0.6nN)

to the three lower flexural eigenmodes of the free cantilever and to the two lower contact eigenmodes (Fig. 5.6). In the spectrum it is visible also a minute contribution from the first torsional mode at 240 kHz, due to positioning the laser spot not exactly in the middle of the cantilever width. The resonant frequencies f_0 and quality factors Q for the free and pinned cantilever are reported in Tab. 5.1. The small disagreement between measured and calculated resonance frequencies can be explained by the not perfect rectangular shape of the cantilever. In this case the fifth eigenmode peak is not visible probably due to the position of the laser spot of the optical beam detection which was on the fifth mode node, see Fig. 5.6. The plan view dimensions measured by an optical microscope are used to estimate the elastic constant $k = 0.13$ N/m [75].

Since we apply the WT approach also to the torsional modes, we need to calculate their PSD from the photodiode lateral temporal traces. The PSD is per-

	t_1	t_2	t_{c1}	t_{c2}	l_1	l_{c1}
Frequency (kHz)	239.4	763.4	305	782	210.1	221.6
Quality factor (Q)	310	570	14	120	590	200
Frequency ratio exp.	22.0	70.0	28.0	71.7	19.3	20.3
Frequency ratio theo.	23.4	70.1			19.0	

TABLE 5.2: Measured and calculated [41, 80] torsional t and lateral l resonance frequencies for the cantilever free (t_i and l_i) and clamped (t_{ci} and l_{ci}) cantilever used in the WT approach. The theoretical results are expressed as ratios with respect to the first flexural frequency. The Q factors are measured from the PSD.

formed off-line by averaging over 90 temporal traces of 1M samples each, acquired at 1MHz, see Fig. 5.9a. The PSD displays the resonance peaks corresponding to the first lateral and and to the two lower torsional modes [80, 81]. The lateral bending mode is analogous to the flexural modes but with interchanged cantilever width and thickness. The resonance frequencies and quality factors are reported in Tab. 5.2. The small peak at 223 kHz is the third flexural mode, which contributes to the lateral signal because the cantilever is not perfectly parallel to the sample surface. The Sader method gives a torsional elastic constant $k_\vartheta = 9.9$ nNm [82].

When the tip is in contact with the surface, due to the modified mechanical boundary conditions, the cantilever end is no longer free. A clear shift of the torsional and lateral mode resonances is observed (Fig. 5.9b). The ratios between free and clamped resonances follows the trend predicted by standard beam mechanical theory [41, 80], as reported in Tab. 5.2. In the PSD it is possible to observe the broadening of the resonances width. The Q factor of the oscillator, expressed as the relative Lorentzian broadening $Q = \Delta\omega/\omega$, is connected to the energy dissipated by the oscillator, the decrease in Q indicates an increase in dissipation processes.

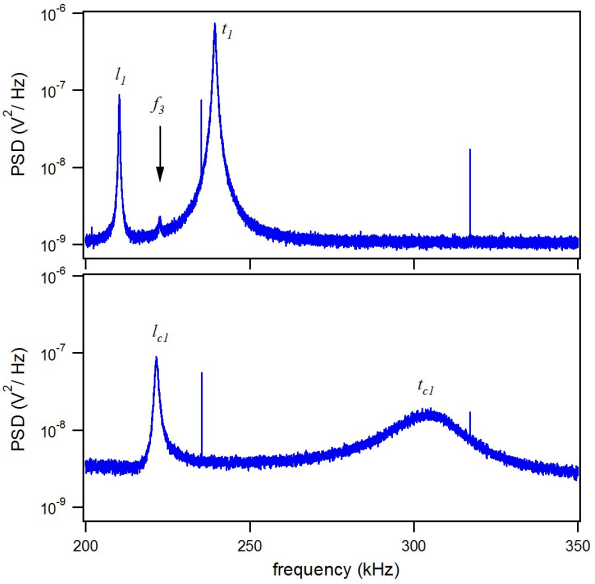

FIGURE 5.9: a) Thermal power spectral density of the cantilever torsional fluctuations zoomed on the first torsional (t_1) and first lateral (l_1) resonance peaks. The arrow points at the third flexural mode (f_3). b) Same as a) but with the tip in contact with the sample at constant negative load (F≈ -0.5nN)

5.4 Data acquisition

The experiments consists in acquiring the temporal evolution of the thermal noise as a function of the tip-sample distance. Then the data are off-line processed to provide the tip-sample interaction forces. We apply two different procedures of data collections depending on the method used to analyze the time signal.

In the FT approach (stationary regime), the oscillating cantilever is placed at a fixed distance from the surface so that the tip experiences the long-range forces of the sample surfaces. The time trace of the cantilever thermal fluctuations is collected by the digitizing oscilloscope. Then the tip is moved toward the sample at a lower distance from the surface and the new time signal acquired. The measurement is repeated at different tip-sample separations up to the jump-to-contact (JTC) distance. The complete data acquisition requires minutes. The time traces of the cantilever thermal fluctuations are off-line processed by three different routes

in order to calculate the long-range tip-sample interaction. The data analysis is performed exploiting programs implemented in MatLab code. Results provided by this approach are presented in Chap. 6.

The WT approach (dynamic or transient regime) consists on acquiring force spectroscopy curves by driving the z-piezo motion at constant velocity to move the tip toward the surface. The time signal i.e. the temporal evolution of the cantilever thermal oscillations as a function of the tip-sample distance (force curve or spectroscopy curve) is stored by the PicoScope PC oscilloscope. The time data are off-line processed using a wavelet transform (WT) analysis exploiting the routines from the WAVELAB library [83]. In this case both long- and short range tip-sample interactions are probed. The total data acquisition required approximately 150 ms, a time orders of magnitude lower than that required for the FT analysis. Moreover, lateral and vertical photodiode signals are collected providing the simultaneous analysis of the cantilever flexural and torsional eigenmodes presented in Chap. 7.

5.5 Summary

The experiments consists in measuring the tip-sample interaction through the analysis of the thermally excited cantilever fluctuations in the vicinity of the sample. The acquisition system relays on an AM-AFM [72] which monitors the cantilever bending by an optical beam deflection system. The photodiode signals feed a digitizing oscilloscope to detect and store the temporal evolution of the cantilever thermal vibrations. The data are off-line processed by two different routes (FT and WT analysis) to provide the tip-sample interaction. In this chapter we described the experimental set-up and the methods used to calibrate the cantilever stiffness. Moreover, we summarized the data acquisition procedures in both static FT and dynamic WT approaches whose results are presented in the next chapters.

Chapter 6

Tip-sample force in the stationary regime

Thermal noise is caused by random thermal excitations that result in positional fluctuations of the cantilever, thereby setting a lower limit on the force resolution of an atomic force microscope. However, thermal noise can also be used to probe the interaction between the AFM tip and the sample. In this chapter we present three different approaches to exploit the information contained in the cantilever thermal motion (frequency shift, Boltzmann distribution of the Brownian motion and thermal mean square displacement) and some results concerning the characterization of the tip-sample van der Waals force.

6.1 Introduction

A NC-AFM is able to detect small long-range forces acting between the AFM tip and the sample surface. Among the various options devised to operate a NC-AFM, the thermal oscillation regime has attracted attention because it provides insights into the fundamental mechanical properties of an AFM in a very direct way [10]. The analysis of the thermal motion of the cantilever is important to characterize both its mechanical properties and the performance of the AFM deflection sensor. The thermal motion (or Brownian motion) of the cantilevers tip is connected to the local mechanical compliance via the fluctuation-dissipation theorem. From the modification of the thermal motion of the cantilever due to the tip-surface interaction forces, it is possible to reconstruct the interaction potential and obtain information on various kinds of surface forces. In this chapter, we will use three different approaches to exploit the information contained in the cantilever thermal motion;

- to measure the shift of the cantilever resonances of the first and second flexural modes as the tip is brought near the surface to retrieve the gradient of the interaction forces [15, 11, 38];
- to analyze the probability distribution of the tips position during the Brownian motion and use the Boltzmann distribution to calculate the Helmholtz free energy of the tip interacting with the surface as a function of the tip-sample distance. From these data, it is possible to obtain the interaction force gradient from the second derivative of the Helmholtz free energy;
- to measure the mean square displacement of the tip subjected to thermal motion to estimate the interaction force gradient dependence on the tip-sample distance.

All the analyses are conducted on the same temporal trace of the tip thermal motion normal to the surface, recorded by sampling the thermally excited flexural modes of the cantilever with a fast digitizer connected to the deflection

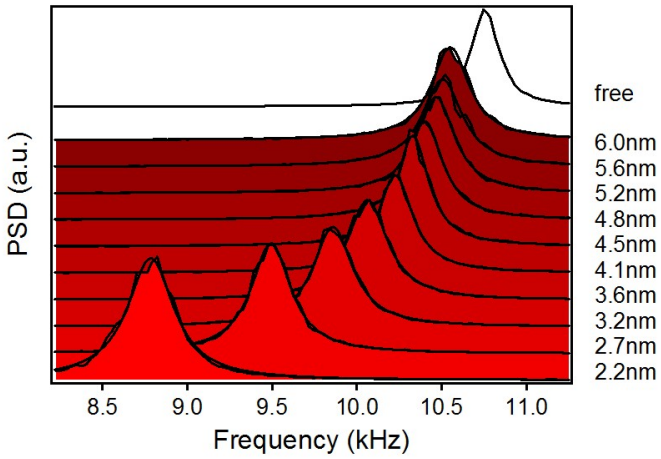

FIGURE 6.1: Power spectral density of cantilevers fluctuations acquired at different tip-sample separations zoomed on the first mode resonance peak. Each spectrum is the average of 20 spectra obtained by Fourier transforming data strings of 520 ksample each, acquired at sampling rate of 4 Msample/s. The resonant peaks are fitted with a Lorentzian.

sensor photodiode of a standard optical beam deflection apparatus. The time signal consists of 20 data strings of 520 ksample each, acquired at sampling rate of 4 Msample/s while the cantilever dwells at a fixed separation from the surface. The total time required to detect and store these data is approximately 3-4 s, by taking into account also the recovery time of the acquisition system. The measurement is repeated at decreasing distances in the range of the tip-sample interaction until the jump to contact occurs. This allows to reconstruct the long-range van der Waals force and to estimate the tip radius. All the data necessary to determine the force versus distance curve are collected in some minutes.

6.2 Frequency shift method

First we place the cantilever far from the surface (free cantilever). From the temporal trace of the thermal oscillations of the free cantilever, we obtain the power spectral density distribution. The first two resonances, at 10.757±0.002

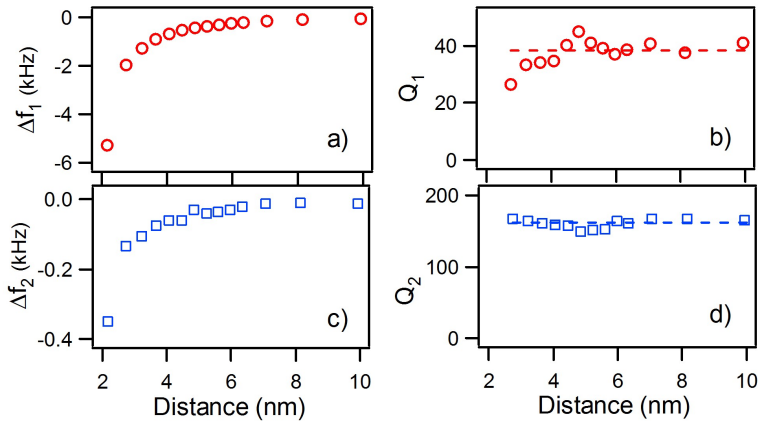

FIGURE 6.2: a) and b) Shift of the resonance frequency and Q factor of the first mode, respectively, as a function of the tip-sample distance. c) and d) Same as a) and b) for the second flexural mode.

and 74.276±0.004 kHz, respectively, are fitted with a simple damped harmonic oscillator model [16, 40], whose Lorentzian curve gives quality factors (Q factors) of about 58 and 170, respectively. (Tab. 5.1).

The analysis is repeated at various distances approaching the surface, up to the jump-to-contact event. Fig. 6.1 shows the thermal PSD at several tip-sample separations as obtained by averaging 20 spectra obtained by Fourier transforming 20 temporal traces collected from photodiode. The image zooms on the first eigenmode resonance peaks and also displays the Loretzian fitting functions. The spectra show a negative shift of the resonance frequency for the first and second modes due to the interaction of the tip with the force gradient near the surface 6.2. Considering each flexural mode equivalent to a mass-spring system, the tip-sample interaction elastic constant, $k_{ts} = -dF_{ts}/dz$ (where F_{ts} is the tip-sample interaction force, z is the tip-surface distance, positive along the surface normal direction), can be expressed as a function of the resonant frequency as

$$k_{ts} = k\left(\frac{(f_0' + f_0)(f_0' - f_0}{f_0^2}\right)$$

where f_0 is the resonant frequency of the free cantilever, f_0' is the resonant frequency of the cantilever that interacts with the surface force gradients, and k is the equivalent elastic constant of the mode under consideration (see also Sec. 3.3. This relation holds if k_{ts} remains constant for the whole range of displacements from the equilibrium position covered by the cantilever and this is assumed to be true in our case since we are dealing with small oscillations (the root mean square deflection of the free cantilever is less than 0.2 nm). If $|k_{ts}| << k$, one expects $f_0' \sim f_0$ and the frequency shift $\Delta f = f_0' - f_0$ becomes proportional to the force gradient $k_{ts} = 2k\Delta f/f_0$ [11, 8]. These approximations (constant k_{ts} and $|k_{ts}| << k$) are valid for the second flexural mode that has a higher equivalent elastic constant, but may break down for the first flexural mode near the jump-to-contact point. Near this point $|k_{ts}| \sim k$ and the effective spring constant experienced by the tip $k^* = k + k_{ts}$ [11, 15] tends to zero ($k_{ts} = -dF_{ts}/dz$ is negative because the tip-sample force is increasingly attractive approaching the surface). As a consequence, the displacement amplitude increases and the condition that k_{ts} remains constant for the whole range of displacements may not be satisfied. However, we experimentally verify that the cantilever can be treated as a mass-spring system up to the jump-to-contact distance by showing that the measured interaction potential (see Sec. 6.3) can be considered parabolic with a good approximation.

Along with the force gradient, it is possible to measure the Q factor, which is found to depend on the distance from the surface (Fig. 6.2b and Fig. 6.2d). Q is almost constant for both flexural modes up to the jump-to-contact distance of D ∼2.2 nm. It is interesting to note that the first flexural mode, but not the second, shows an evident decrease in the Q value before the jump-to-contact distance. This means that the interaction is conservative at distances greater than D and becomes increasingly dissipative on approach to this point. The fact that the second mode does not show a decrease in the Q value can be explained with a superposition principle argument. Since the equivalent stiffness of the second mode is much higher than that of the first, the oscillation amplitude of the second

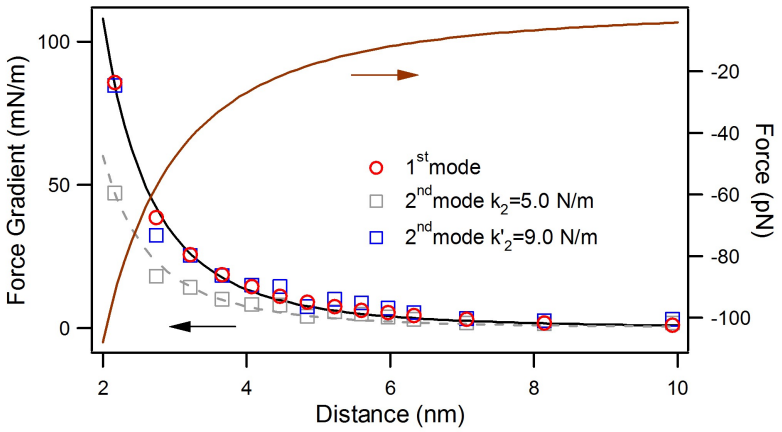

FIGURE 6.3: Force gradient between the tip and the sample resulting from the frequency shift of the first and second mode as a function of the tip-sample distance. For the second mode, data obtained by two different values of the spring constant k_2 are displayed. The line is the fitting power function Az^{-3}.

mode remains small even at distances where the first mode amplitude becomes substantially higher. As a consequence, the dissipation of the cantilever energy to the surface is channeled mainly through the first mode, not the second.

It is interesting to note that near the sample, the quality factors ($Q_1 \sim 40$ and $Q_2 \sim 160$) are lower than that of the free cantilever ($Q_1 = 58$ and $Q_2 = 170$, see Tab. 5.1). The decrease is due to the interaction of the rectangular beam with the sample surface. If the tip-sample separation is very small, the distance between the beam and the surface is about the tip height (nominal value $h = 20 - 25$ μm). When the cantilever oscillates in air or in a fluid close to a solid surface, due to a confinement effect, an increased damping is manifested as a decrease of the quality factor [84]. This effect is relevant for piezotube movements on the μm scale but not on the nm scale covered by the present measurements, where the effect of the tip-sample interaction dominates.

The measured force gradient versus distance is shown in Fig. 6.3 (circles) for the first flexural mode. The dependence of the force gradient on the tip-surface distance z is well reproduced by a simple power function, describing a van der

Waals-like tip-sample interaction $dF_{ts}/dz = Az^{-3}$ [51, 56], where A is a constant, up to the jump-to-contact distance. All cantilevers we used display the same dependence of the force gradient on the tip-sample spacing, i.e., measurements are reproducible.

The same procedures are applied to the frequency shift of the second flexural mode. In this case, we obtain a much stiffer equivalent elastic constant of $k_2 = 42k = 5.0$ N/m by the Sader method and, as a consequence, the frequency shift of the second mode is smaller by almost one order of magnitude with respect to the first mode. When we compare the force gradient calculated from the frequency shift of the second mode Fig. 6.3 with that from the first mode, a clear discrepancy is evidenced. Since the explored physical potential is obviously the same for both flexural modes, this discrepancy must hint to some problems inherent to the method used to determine k_2. It is known that the mass of the tip shifts the node of the cantilever second flexural toward its free end, causing a reduction in its effective length and thus a higher equivalent stiffness [29, 85]. Since the Sader calculation does not take into account this mass loading effect, a stiffer equivalent elastic constant k_2 is expected for the second flexural mode. On this basis, we increased the k_2 value until a satisfactory fit to the $dF_{ts}(z)/dz$ retrieved with the first mode was obtained, finding on physical grounds that the equivalent stiffness of the second mode is $k_2 = (75 \pm 10)k$.

6.3 Potential from Boltzmann distribution

The temporal trace of the free thermal oscillations normal to the surface of the cantilever has been digitized at 4 Msample/s for a time span much longer than the average vibration period of the cantilever. During its motion, the cantilever is thermally sampling the accessible deflections according to a Boltzmann probability distribution

$$p(s) = p_0 \exp\left(-\frac{V(s)}{k_B T}\right)$$

where $p(s)$ is the probability of observing the tip at a deflection s from the equilibrium position, p_0 is a normalization constant, $V(s)$ is the position dependent potential, k_B is the Boltzmann constant, and T is the absolute temperature. Inverting the relation gives

$$V(s) = -k_B T \ln \frac{p(s)}{p_0}$$

which connects the potential (within an additive constant) to the probability to find the cantilever at a certain deflection s, measured as the number of counts observed at a certain deflection divided by the total number of counts in the entire temporal trace. Since the actual thermal oscillation is influenced by the cantilever static deflection due to F_{ts}, the potential will depend also on the equilibrium tip-surface distance z_0, i.e. $V = V(s, z_0)$. Following Ref. [86] we consider two contributions to the total potential V, the cantilever potential V_c and the tip-sample interaction potential V_{ts}, so that $V = V_c + V_{ts}$. This relation is formally valid for an instrument with an infinite acquisition bandwidth and without electronic noise. Since real instruments have electronic noise that cannot be completely filtered out, the amplitude of the random oscillations of the cantilever is overestimated. As a consequence, an apparent larger curvature of the retrieved potential is detected. This effect is not present in the other two proposed methods because in one case only frequency measurements are required to retrieve forces (frequency shift) and in the other the electronic noise can be easily separated from the signal in the Fourier domain. The effects due to electronic noise are taken into account by a multiplicative correction factor ϵ in the potential relation $V = \epsilon(V_c + V_{ts})$. The correction factor is experimentally found by measuring the free cantilever thermal oscillation $V_c(s, \infty)$ and comparing the measured cantilever spring constant (Sader method) with the apparent cantilever constant obtained by the second derivative of the potential $k_{app} = d^2/ds^2\,(V_c(s, \infty))$, i.e., $\epsilon = k_c/k_{app}$. In the present case, the correction factor is $\epsilon = 1.2$.

Since we are interested in measuring $V_{ts}(s, z_0)$, the cantilever potential is subtracted from the total potential and the result is shown in Fig. 6.4. We note

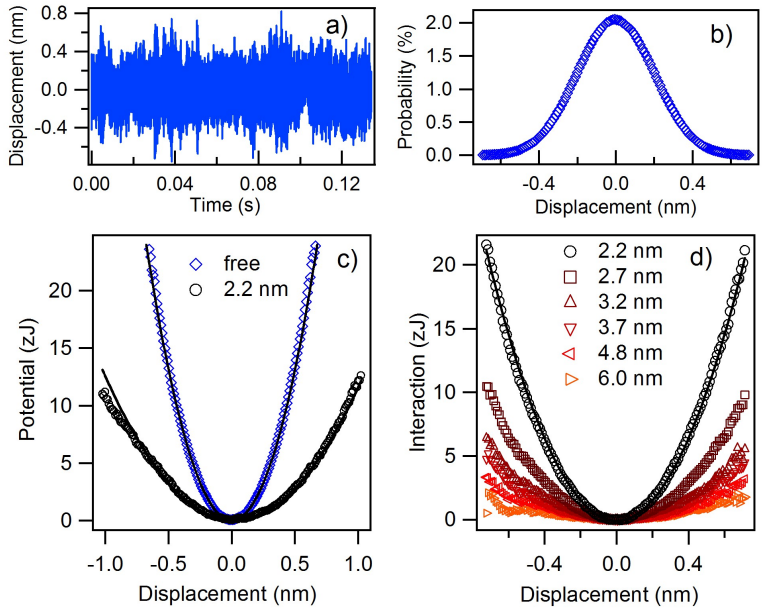

FIGURE 6.4: Results obtained by the potential analysis. a) Fluctuations of the free cantilever as a function of time retrieved by off-line bandpass filtering (50 Hz-100 kHz) of the photodiode signal. b) Probability distribution of the free cantilever deflections. The plot is the average of the probability curves calculated from 20 time signals like the one in a). The distribution is Gaussian. c) Apparent potentials of the free cantilever at 2.2 nm and far from the surface. These potentials are fitted with parabolas. d) Tip-sample interaction potentials obtained subtracting the free cantilever potential to the total potentials. The 2.2 nm interaction potential is fitted with a parabola.

that the data corresponding to $V_{ts}(s, z_0 = 2.2 \text{ nm})$ in Fig. 6.4 are well described by a parabolic fit, confirming that the cantilever in interaction moves in a quasiharmonic potential and thus can be described as a mass-spring system. To give an estimate of the expected anharmonicity, consider the interaction potential at an equilibrium position z_0, obtained after the expansion of the van der Waals potential up to the third order and subtraction of the harmonic cantilever contribution,

$$V - \frac{1}{2}k_c s^2 = \text{const.} - \frac{HRs^2}{6z_0^3}\left(1 - \frac{s}{z_0}\right)$$

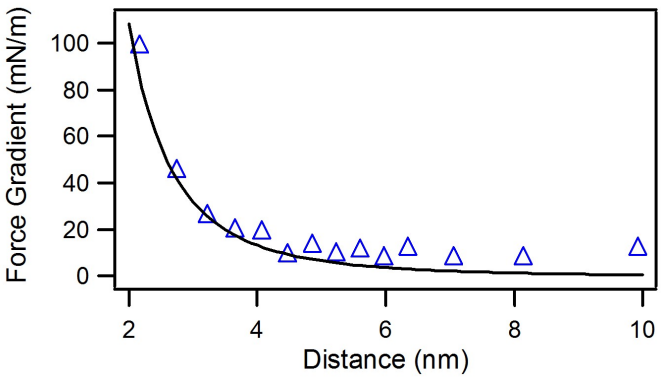

FIGURE 6.5: Force gradient between the tip and the sample calculated by the second derivative of the potentials. The line is the power function Az^{-3} resulting from the fitting of the frequency shift data.

see Fig. 6.4d, where s is the displacement from the equilibrium position z_0, positive along the surface normal direction. The anharmonic third order term at z_0=2.2 nm and for a displacement s=0.2 nm is estimated to be roughly 1/10 of the quadratic term. From the fitting procedure, using a quadratic function of s, we obtain residuals of the same order of magnitude. However, the noise and the resolution of our analog-to-digital converter do not allow a quantitative estimation of the anharmonic term.

The force gradient between the tip and the sample is calculated by the second derivative of the potentials $dF_{ts}/dz = d^2/dz^2 V_{ts}$. As shown in Fig. 6.5, the force gradient delivered by the potential method is in good agreement with the one measured by the frequency shift method.

6.4 Mean-square displacement from power spectral density

The cantilever in thermal equilibrium with the molecules of the gas or liquid in which it is immersed fluctuates in response to stochastic forces due to molecular

motion that is connected to the temperature of the thermal bath. The equipartition theorem states that the mean square displacement of the tip from its neutral position is described by $1/2k_BT = 1/2k\left\langle s^2\right\rangle$. $\left\langle s^2\right\rangle$ is the mean square displacement of the cantilever caused by the thermal motion in the direction normal to the surface, k_B is the Boltzmann constant, T is the temperature of the surrounding heat bath, and k is the cantilever spring constant. Measuring the mean square fluctuations of a freely vibrating cantilever allows one to estimate the cantilever spring constant. This estimation is performed by taking into account a) that all vibration modes contribute to the mean square displacement and b) that with the optical lever technique the slope at the cantilever end is detected instead of the deflection itself [41].

The temporal trace of the free thermal oscillations is affected by various noise sources, which tend to mask the thermal thermal contribution. In order to isolate the thermal oscillations, the data are examined in the frequency domain [79, 78, 47]. First, we collect photodiode signal of the free cantilever. The temporal trace is composed of 20 time signals acquired at 4 MHz for about 0.13 s (520 ksamples). The PSD is calculated off-line and then averaged over the 20 traces. In the absence of additional noise sources, the power spectral density of the cantilever fluctuations has a Lorentzian line shape. White noise adds a background floor to this thermal response. Subtracting this background, the area below the remaining peak is the estimation of the power of the cantilever fluctuations, see Fig. 6.6a. The integral over all frequencies of the power spectrum equals the mean square of the displacements in the time domain. Then, for the first flexural mode, the spring constant is directly evaluated by (see also Eq. 5.2):

$$k = 0.82\frac{k_BT}{P'}$$

where P' is the area of the power spectrum of the thermal virtual deflections alone (the superscript ' means that the optical lever measures the slope at the cantilever end, i.e., the virtual deflection, instead of the deflection itself) [41, 50].

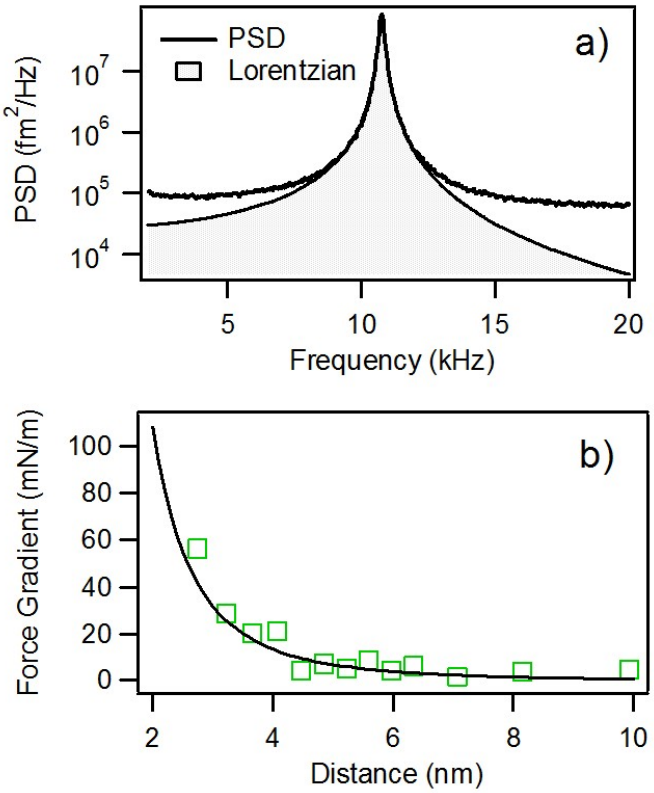

FIGURE 6.6: Results from mean square displacements analysis. a) Power spectral density of the free cantilever fluctuations. The shaded area is the contribution of the simple harmonic oscillator (Lorentzian function), that is the fit minus the white-noise background. The mean square of the cantilever displacement in the time-series data equals this area. b) Force gradient between the tip and the sample calculated by the reduced effective spring constant k^*. The line is the power function Az^{-3} resulting from the fitting of the frequency shift data.

The analysis we already performed for the free cantilever is repeated at various tip-sample distances approaching the surface until the jump-to-contact occurs. As pointed out in Sec. 6.2, since we are dealing with small oscillations, the tip-sample force gradient can be considered constant for the whole range of displacements from the equilibrium position covered by the cantilever at each tip-sample distance. This interaction causes an additional spring-type force F_{ts}. The interac-

tion elastic constant retrieved from the gradient along the normal to the surface $k_{ts} = -dF_{ts}/dz$ is negative and reduces the effective spring constant $k^* = k + k_{ts}$ (see Eq. 3.10) where the superscript * indicates that the elastic constant refers to an effective mean square displacement increased by the tip-sample interaction. The cantilever mean square fluctuations increase due to the lower spring constant. Measurements of the cantilevers mean square virtual displacement $\langle s'^2 \rangle = P'^*$ at several distances approaching the surface allow to estimate the reduced effective spring constant

$$k^* = 0.82 \frac{k_B T}{P'^*}$$

The force gradient is easily deduced by the relation

$$\frac{dF_{ts}}{dz} = -k_{ts} = k - k^*$$

As in the previous analyses, the force gradient displays a van der Waals-type dependence $dF_{ts}/dz = Az^{-3}$ on tip-sample distance z, see Fig. 6.6b.

Finally, it is worthwhile to note that in all cases, the tip-sample separation z is determined by both the piezotube position and the cantilever static deflection.

6.5 Discussion on the static regime results

The flexural mode resonances calculated for a cantilever with a rectangular section (without tip, the so-called diving board mode [10]) agree, within a systematic $10\% - 15\%$ underestimation, with the experimental values, as reported in Tab. 5.1. According to the equivalent stiffness model [85] the elastic constant associated with the first and second flexural modes of such cantilever are $k_1 = 1.03k$ and $k_2 = 40.2k$, where

$$k = 0.25 \frac{Ewh^3}{L^3}$$

(here, L is the length of a cantilever with a rectangular cross section of width w and thickness h and E is the modulus of elasticity). Since the correct equivalent stiffness for different eigenmodes can be approximately determined experimentally

			Theoretical	
	k_2	k_2'		tip 10%
k=0.12 N/m	Sader method	From fit to k_{ts}	no tip	CL
k_2 N/m	5.0	9.0		
k_2/k	42	75	40.2	74.9

TABLE 6.1: Experimental evaluation of the second mode equivalent spring constant obtained by the Sader method and retrieved by the fit to the first mode force gradient curve. Theoretical prediction without and with mass loading obtained from finite elements calculations in [85].

using Saders method [75] the discrepancy pointed out in Sec. 6.2 must be reconciled by invoking a mass loading effect. According to the calculations reported in [85], a 10% tip mass is sufficient to modify the equivalent stiffness to $k_1' = 1.01k$ and $k_2' = 74.9k$. Therefore, while the tip mass does not influence significantly the equivalent stiffness of the first eigenmode, it can have a dramatic effect on the equivalent stiffness of the second. Similar results have been reported in [29]. Tab. 6.1 shows a comparison of the theoretical values without and with mass loading with the experimental results based on the Sader method and the results based on the fitting procedure explained in Sec. 6.2. It can be seen that the experimental value of k_2' which reconciles the gradient force calculated from the frequency shift of the second mode to the gradient force retrieved from the first mode frequency shift, is comparable with the theoretical value calculated with a 10% tip mass loading.

We would like to point out the fundamental differences in considering the actual elastic constant of the cantilever, k, and the equivalent elastic constants associated with each mode, k_1 and k_2. The elastic constant k is specified by the elastic properties of the material and the dimensions of the cantilever and can be retrieved using the *thermal tune* method by measuring the mean square tip displacement and applying the equipartition theorem from the resonance shape of the first or the

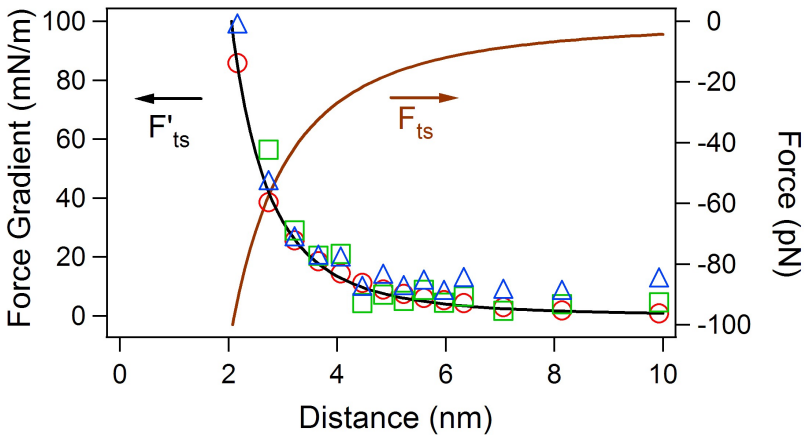

FIGURE 6.7: Force gradient provided by (red circles) the frequency shift method, (blue triangles) the potential from Boltzmann distribution method, and (green squares) the mean square displacement from power spectral density method. The line is the power function Az^{-3} resulting from the fitting of the frequency shift data in Fig. 6.3. The force is the analytic integral of the this fitting function $(-A/(3z^2))$.

second mode. It can also be retrieved from the Sader method applied to the first flexural mode and, as stated in Sec. 5.3, all these methods give an elastic constant value within 5%. Instead, the equivalent constant of each mode, k_1 and k_2, gives a different information, not linked only to the elastic constants of the material, but taking into account the modal shape in connection to the tip displacement. Since each mode is viewed as equivalent to a mass-spring system, to have the same actual tip displacement Δz needs different interaction forces for different flexural shapes and, consequently, at each mode is assigned a different equivalent elastic constant $k_i = F_i/\Delta z_i$, i=1,2.

The gradient of the interaction force between the tip and the surface obtained by the three methods discussed above are reported in Fig. 6.7 to demonstrate their consistency. Force gradients of the order of tens of mN/m and interaction forces of the order of tens of piconewton are easily accessible with a standard AFM.

When the proximity between material objects becomes of the order of a few

microns down to nanometers, van der Waals and Casimir forces, which are quantum mechanical in nature, become operative [28]. In the present case, the force gradient data are well reproduced by a nonretarded van der Waals function in the form (see Sec. 3.4):

$$\frac{dF_{ts}}{dz} = \frac{HR}{3z^3}$$

with $HR = 3 \cdot 10^{-27}$ Jm, from which it is possible to extract the Hamaker constant H if the radius of curvature of the cantilever R is known. Since we have not directly measured R, no measure of H is possible. However, from the typical values of H in graphite (H=0.1 aJ [56, 57, 58]), it is possible to infer R=30 nm, which is compatible with the radius of curvature given by the manufacturer. The interaction force F_{ts}, reported in Fig. 6.7, is obtained by the analytic integration of the interaction force gradient, giving a dependence as $-HR/6z^2$.

Finally, we note that approaching the surface, the jump-to-contact occurs before the tip-sample distance corresponding to the interaction instability (see Eq. 3.12) $d/dzF_{ts}(z_{jtc}) = k$. Therefore, the jump to contact we observe is mainly due to capillary force of the liquid meniscus linking the tip and the surface, as explained in Sec. 3.4. These mechanisms justify that the reduction in the Q factor has an extremely sharp distance dependence, indicating that the underlying dissipation mechanism is very local due to some interaction of the very end of the tip with the wetting layer on the surface.

6.6 Summary

In this chapter we reconstruct the tip-sample interaction potential from the modification of the thermal motion of the cantilever due to the tip-surface interaction forces. The analysis is performed in stationary regime by applying three different approaches to exploit the information contained in the cantilever thermal motion: frequency shift, Boltzmann distribution of the Brownian motion and thermal mean square displacement methods. All the analyses are conducted on the same tempo-

ral trace of the tip thermal motion normal to the surface, providing aa estimation of non retarded van der Waals interaction forces. We also estimated the tip mass loading effect on the cantilever elastic behavior by comparing the results provided by the frequency shift of the two lower flexural eigenmodes.

Although the methods employed are well established, their simultaneous use in the same experimental session allows one to fully calibrate the instrument in terms of frequency response, temporal response, and sampling rate of the optical lever deflection system and the associated electronics. The main limitation of the stationary regime analysis is that it requires long acquisition time since it takes minutes to perform a complete force versus distance curve. In order to prevent thermal drift effects and especially to allow Dinamical Force Spectroscopy imaging, the experimental conditions and data analysis should be improved to shorten the acquisition time as it is described in the next chapter.

Chapter 7

Wavelet analysis in dynamical force spectroscopy

Time-frequency analysis by wavelet transform is an effective tool to characterize the spectral content of signals rapidly varying in time. Wavelet transform analysis is applied to a thermally excited dynamic force spectroscopy to get insights into fundamental thermodynamical properties of the cantilever Brownian motion as well as giving a meaningful and intuitive representation of the cantilever dynamics in time and frequency caused by the tip-sample interaction forces. It is remarkable the possibility to carry out measurements across the jump-to-contact transition without interruption, providing information on the long- and short-range adhesion surface forces. Information on tip-sample van der Waals interaction, adhesion forces, friction and elastic properties of the surface are acquired in approximately 100 ms, a time compatible with practical Dynamic Force Spectroscopy imaging.

7.1 Introduction

Atomic force microscopy (AFM) delivers not only topographical images with submolecular resolution but provides also sensitive force measurements on the nanometer and atomic scale [16, 6, 8, 10]. The use of AFM in force measurements is commonly referred to as *force spectroscopy*. The simplest technique used for quantitative force measurements involves directly monitoring the static deflection of the cantilever, from which the force is determined using Hooke's law [79, 27, 28].

More refined techniques rely on the measurements of the cantilever dynamical parameter while it is excited at or near its resonant frequency and interacting with the force field provided by a sample surface. The interactions of the tip with the sample surface perturbs the amplitude, frequency, phase or damping of the cantilever oscillation. The measurement of these parameter modifications provides a sensitive estimation of both long-range and short-range interaction force [29, 30, 25, 31, 32, 33, 34].

The cantilever can be excited and the response recorded over a band of frequencies simultaneously, rather than at a single frequency. The full spectral response allows to reconstruct force-distance spectroscopy and enables to directly measure the energy dissipation through the determination of the Q-factor of the cantilever-sample system. The simultaneous analysis at all frequencies within the excited band (parallel detection) reduces the acquisition time. Broad band excitation can be achieved by external driving force [37] or by thermal excitation [38, 39].

In both cases the spectral analysis is usually provided by the Fourier transform of the cantilever amplitude response, to represent it in the frequency domain and obtain the power spectral density of the cantilever oscillations. However, Fourier analysis is correctly interpreted only in the case of stationary systems, i.e. the frequency spectrum must be correlated with a temporally invariant physical system. If the spectral content of the signal changes during the data collection, this change is not revealed in the Fourier transform description which only displays an average

over the time period and prevents from correlating the frequency spectrum with the signal modification in time.

Non-stationary signals require a mathematical tool that combines time domain and frequency domain analysis, the wavelet transform (WT) approach. WT converts one-dimensional time signal into two-dimensional time-frequency representation, which displays the time and frequency information of the signal in a time-frequency plane. This is particularly useful to study transitory regimes i.e. signal with a frequency spectrum changing during the data collection. One such example is the jump-to-contact (JTC) transition, which occurs when the attractive interaction force gradient exceeds the cantilever spring constant [8].

In the following, we apply the wavelet transform approach to study the tip-sample interactions across the JTC transition in the thermal driving regime and to characterize the adhesion surface forces after JTC. In studying transients it is also necessary to improve the temporal resolution and reduce the acquisition time to values compatible with practical dynamical force spectroscopy imaging.

The measurement is performed on HOPG in ambient condition. The cantilever deflections are detected by an optical beam deflection system and a four quadrant photodiode. The differential voltage output from the photodiode sectors (up-down for the flexural modes and right-left for the torsional modes) are simultaneously collected by a digitizing oscilloscope. Force spectroscopy curves are collected driving the z-piezo motion at constant velocity of 225 nm/s. Since the sampling time is 240ns, the signal string is composed of 4.166×10^6 sampling points every second. The time signal i.e. the temporal evolution of the cantilever thermal oscillations as a function of the tip-sample distance (force curve or spectroscopy curve) is off-line processed by wavelet transform (WT) analysis exploiting the routines from the WAVELAB library [83].

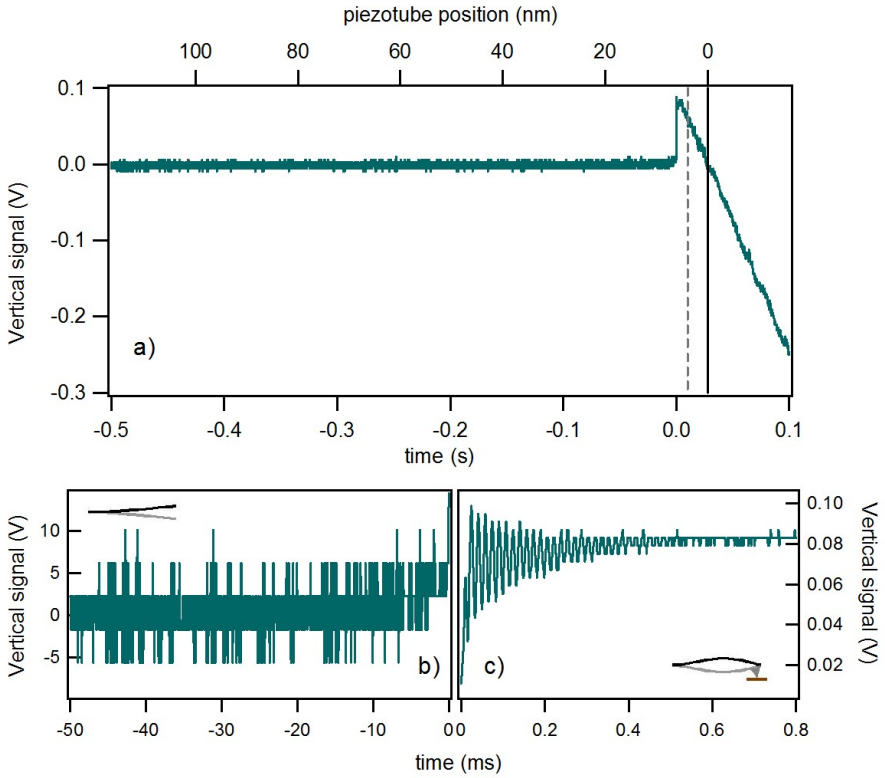

FIGURE 7.1: a) Force spectroscopy curve showing the signal collected by the optical lever detector as a function of time and piezoscanner position. The origin of the time corresponds to the onset of the jump-to-contact (JTC), the origin of the piezotube position to the surface position. b) Zoom on the cantilever oscillation just before the JTC. c) Oscillations of the pinned cantilever immediately after the JTC.

7.2 Tip-sample interaction by flexural modes

To study the tip-sample interaction, the cantilever Brownian motion and its static deflection are detected while the tip approaches the sample, to obtain a *spectroscopy curve*, as shown in Fig. 7.1a. The spectroscopy curve contains a measurement of the temporal evolution of both the static deflection and the frequency distribution of the thermally excited vibration modes of the cantilever up to the cut frequency of the optical beam detection system. The static deflection in approaching the sample (Fig. 7.1b) is caused by long-range electrostatic forces, that

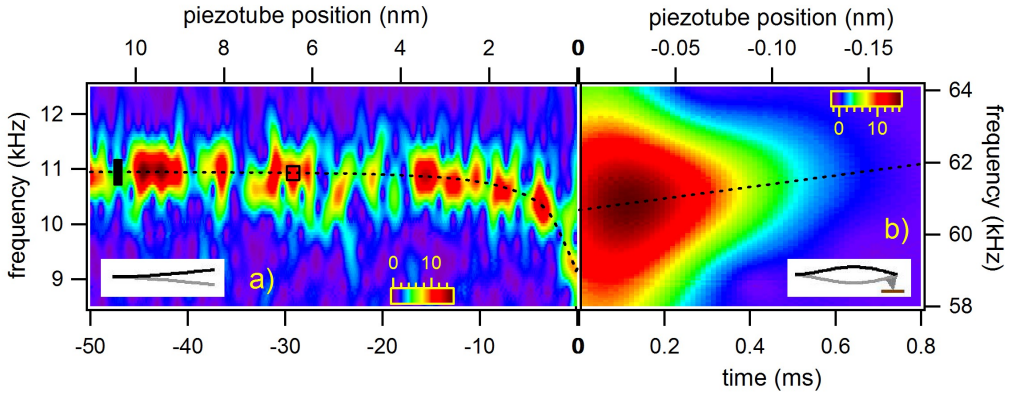

FIGURE 7.2: a) Wavelet transform of the spectroscopy data before the JTC. The black box is the Heisenberg box at the respective frequency. The open box delimited by black lines represents the damped oscillator box. A marked frequency decrease is observed just before the JTC as indicated by the dashed line, that is a guide to the eye. b) Time-frequency representation of the cantilever thermal fluctuation immediately after the JTC. The big bump is the clamped cantilever oscillation due to the tip impact with the surface. The dashed line is a guide to the eye to show the frequency increase.

affect also the resonant frequencies of the cantilever thermally driven eigenmodes until the JTC transition occurs. The JTC transition is accompanied by a high-amplitude damped oscillation of the clamped cantilever started by the impact of the tip on the surface, visible immediately after the transition (Fig. 7.1b). After the JTC transition, the cantilever is still thermally excited, vibrating with different boundary conditions and mode resonances due to the clamped end.

The wavelet transform analysis provides a time-frequency representation of the temporal evolution of the spectral content of the thermally excited cantilever across the JTC transition, as shown in Fig. 7.2 and Fig. 7.3 for the flexural modes. The time-frequency representations display structures centered around the eigenmode frequencies. The discontinuous appearance of the signal will be discussed in Sec. 7.2.3. Despite of the smaller mean square displacements of the higher flexural modes, their thermal spectra are still visible above the background mechanical

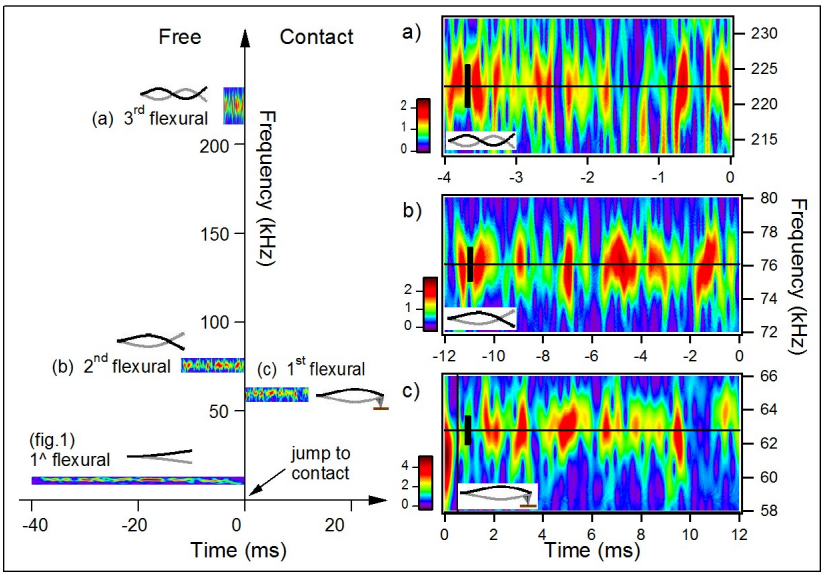

FIGURE 7.3: Time-frequency representation of the cantilever thermal motion across the JTC transition, showing the first three flexural modes and the first contact mode provided by the same temporal trace of Fig. 7.1a. a), b) and c) Wavelet transform of the third and second free modes and of the first contact mode, respectively. The black boxes represent the Heisenberg boxes. The black lines correspond to the resonant frequencies from power spectral density fitting by Lorentzian function. The bump in c) has been rescaled by a factor of 0.2 for graphical reasons. The high mode stiffness prevent the observation of the frequency shift near the surface.

noise, as shown in Figure 7.3. The frequency shift due to the (weak) surface forces before the JTC is visible only in the first flexural mode and negligible in the higher modes because of their much higher equivalent stiffness [85, 39, 29]. The frequency shift due to the JTC transition is followed seamlessly by the wavelet transform, that allows to characterize the very moment of the cantilever jump within the wavelet time resolution. From the temporal traces we estimate that the cantilever takes around 10 μs to collapse into the new state with a clamped end, a duration shorter than the system oscillation period and that can be considered as instantaneous on the cantilever typical timescales.

In the following, we first discuss the analysis of the static and dynamic force spectroscopy data, to confirm their quantitative agreement and discuss the advantages of wavelet analysis. Then we concentrate on the analysis of the spectral transient immediately after the cantilever jump to the surface, that gives information on the adhesion forces.

7.2.1 Static vs dynamic force spectroscopy

In the static deflection analysis the photodiode signal is converted into cantilever deflections trough the detection system sensitivity. The tip sample distance is calculated from the piezotube position taking into account the cantilever static deflection itself. As the tip is moved closer to the surface, the cantilever bends because of the long-range tip-sample interaction but still thermally vibrates around the equilibrium position, see Fig. 7.4. The deflecting force is retrieved multiplying the cantilever static bending by its elastic constant k. The deflection signal is denoised with a Daubechies wavelet basis [61] to remove additive noise like electrical noise or thermal fluctuations.

Since the sample is electrically neutral, the only long-range force is the van der Waals attraction, which for a spherical tip interacting with a flat sample has the form $F_{ts} = HR/6z^2$, see Sec. 3.4. Here H is the Hamaker constant, R the tip radius and z the tip sample separation, positive along the surface normal direction. We fitted the denoised static bending force curve by the Hamaker interaction as suggested in [79], providing an estimation of $HR = 1.1 \times 10^{-27}$ Jm. Due to the weakness of the interaction force, the signal from the optical beam deflection system due to the static bending is few times the minimum resolution of the analog to digital converter, i.e. few times its least significant bit (2.5 Å), represented as vertical gray lines in Figure 7.4. After averaging and denoising, the maximum static deflection (3.5 Å) is comparable to the free cantilever mean square thermal vibrations (2 Å) so that changes of HR by $\pm 50\%$ still gives a van der Waals function consistent with the measured static deflections, as evidenced by the dashed

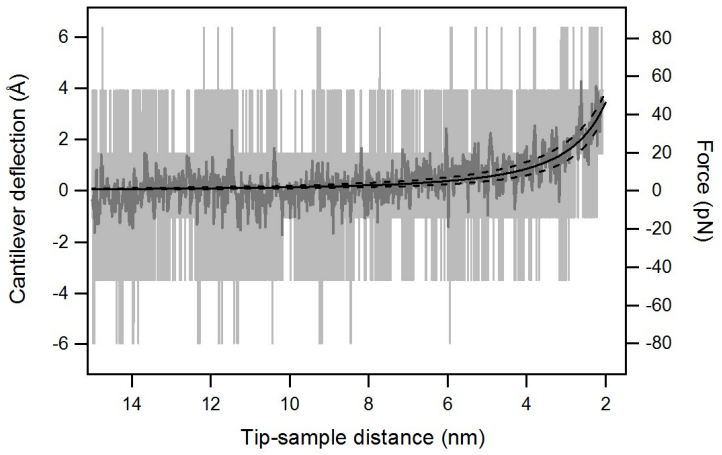

FIGURE 7.4: In light gray the cantilever deflection versus tip-sample distance as sampled from the optical beam deflection system. The resolution bits from the analog to digital converter are clearly visible. In gray the previous signal after wavelet denoising. The line is the fitting by an Hamaker-like force of the denoised signal. The dashed line are provided by an Hamaker constant ±50% of the fitted one. The origin of the distance axis (corresponding to the dashed vertical line in Fig. 7.1a) is determined as a fitting parameter.

lines in Fig. 7.4. This gives an estimation of $HR = (1.1 \pm 0.5) \times 10^{-27}$ Jm. It is remarkable that wavelets can extract information from a temporal signal with an amplitude of just five bits. We verified that the same results can be obtained with signals sampled with better resolution.

The same signal used for the static deflection analysis has been processed by wavelet transform analysis, providing the time-frequency representation for the first flexural mode shown in Fig. 7.2a. Before the tip JTC, the time-frequency representation displays a negative frequency shift of the first free flexural mode caused by the tip-surface force gradients due to the long-range forces. The instantaneous frequency is calculated by the wavelet ridges, the maxima points of the normalized scalogram. In order to reduce noise effects, only maxima above a threshold are considered. From the instantaneous frequency the gradient of the tip-sample interaction force is directly retrieved (Sec. 3.3) to obtain a tip-sample

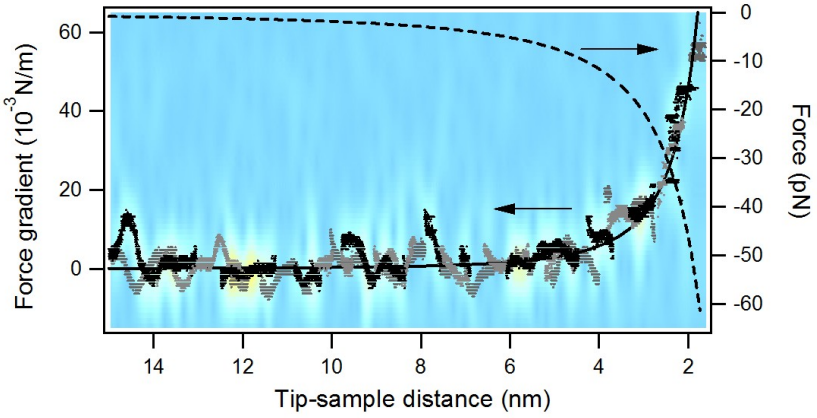

FIGURE 7.5: Force gradient vs tip-sample distance near JTC using wavelet ridges, showing the instantaneous frequencies within the limits of the scalogram resolution. The WT of Fig. 7.2a) is represented in color scale on the background together with its ridges (black points). Gray points are ridges corresponding to other two measurements to show reproducibility. The continuous black line is an Hamaker-like force gradient function fitted to the wavelet ridges. The origin of the distance axis (corresponding to the dashed vertical line in Fig. 7.1a) is determined as a fitting parameter. The dashed line is the force calculated by mathematical integration.

distance vs force gradient image (Fig. 7.5). The analysis is repeated with other two spectroscopy force curves in order to demonstrate reproducibility and to improve results accuracy. The gradient data from WT ridges of the three measurements together are well fitted by a van der Waals function, with $HR = 1.1 \times 10^{-27}$ Jm. The uncertainty of the HR measurement is evaluated by repeating the fitting procedure to each of the three wavelet frequency data separately. The values obtained (HR=1.2, 1.2, 0.96 $\times 10^{-27}$) give an uncertainty of 10%. Thus wavelet transform analysis provides $HR = (1.1 \pm 0.1) \times 10^{-27}$ Jm, an estimation more precise than that released by the static deflection method. Using the the nominal radius of curvature given by the manufacturer ($R = 10$ nm), the measured Hamaker constant agrees with typical values of H in air ($H = 0.1$ aJ, [10, 56]). The interaction force is provided by analytical integration of the fitted force gradient function. This

means that WT analysis allows a precise estimation of the tip-sample van der Waals interaction with a single force curve acquired in less than 40ms, a time significantly lower than that usually needed for force versus distance measurements.

An important point in measuring the tip-sample interaction is to fix the surface position of the graphite sample in the spectroscopy curve. We have described three kind of spectroscopy curves: 1) static bending, non-contact mode, long-range forces; 2) dynamical force spectroscopy, frequency shift, long-range forces; 3) static bending, contact mode, short-range forces. The "true" surface position is determined from the static bending in contact mode by tracing a line extending the horizontal trace of the non interacting cantilever to intersect the contact line after JTC. The intersection relates the position of the surface to the piezo scanner position, i.e. the position where the cantilever is not deflected while the tip is in contact with the surface. The surface position is represented by the continuous vertical line in Fig. 7.1.

In the van der Waals force fit of both the static bending and the frequency-shift analysis, the position of the vertical force barrier is a fitting parameter. In Fig. 7.4 and Fig. 7.5 the vertical force barrier is located at $z = 0$ to appreciate the spatial range of these long-range forces, however this must not be regarded as the true surface position. In fact, taking the surface position obtained from the contact deflection curve as a reference, both the static bending and the frequency-shift analysis fitted with the van der Waals long-range force function place the vertical force barrier very nearly in the same place, about 4 nm above the true surface position. From the fitting procedure, we obtain 4 ± 1 nm from the static bending analysis and 4.0 ± 0.1 nm from the frequency shift analysis. This vertical force barrier is indicated by a vertical dashed line in Fig. 7.1. This behavior is reproduced in all the measurements we performed. The wavelet frequency analysis using the wavelet ridges is thus independently validated against the static bending analysis. Similar results have been reported also by [53] and explained as a wetting layer effect. In ambient condition a water layer can deposit on the tip and/or on the

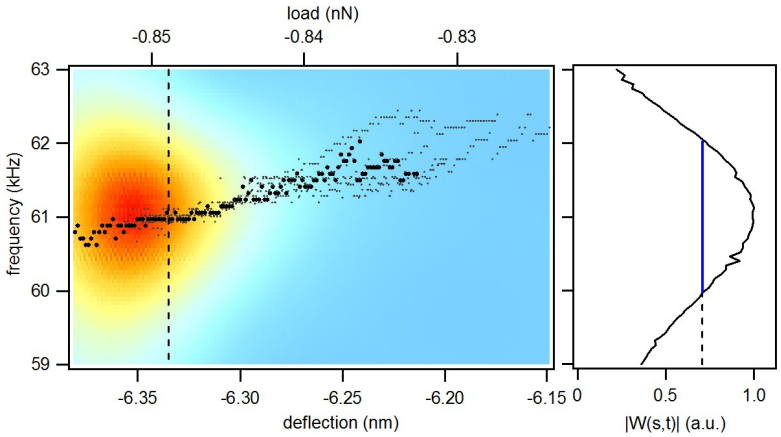

FIGURE 7.6: a) Temporal evolution of the resonant frequency for the first contact eigenmode immediately after the jump-to-contact. The WT of Fig. 7.1c) is represented on the background together with its ridges (black points). The instantaneous frequency increases as the cantilever is moved toward the sample. Ridges corresponding to different measurements (gray points) display similar behavior. b) Normalized wavelet coefficient $|W(s,t)|$ along the dashed line in a).

sample. Then the tip-sample distance, calculated from the long-range force data of both static bending and frequency-shift analysis, is from the liquid-vapor interface. The true surface position, as explained above, is deduced from the contact deflection vs distance curve since in this case the tip is pulled through the liquid film (solid-liquid interface).

7.2.2 Contact dynamic force spectroscopy

The JTC transition is accompanied by a high-amplitude damped oscillation of the clamped cantilever started by the impact of the tip on the surface, visible immediately after the transition (Fig. 7.1c). In this case the tip, attracted by the short-range adhesion forces, behaves like a nano-hammer. The wavelet transform can be carried out across the JTC transition without interruption (Fig. 7.2c). The changed boundary condition (from free to clamped cantilever end) produces a sudden variation of the flexural resonant frequencies. The oscillations induced by the

JTC event are shown in the wavelet representation as a big bump in the time-frequency space (Fig. 7.6). The time scale is converted to cantilever deflection scale taking in account the piezotube movement and the position of the surface deduced by the deflection vs distance curve (the $z = 0$ position corresponds to the solid-liquid interface). Negative deflection means that the beam is bent toward the sample. The load of the tip on the sample is directly calculated as $F_{load} = kd$ where k and d are the cantilever elastic constant and static deflection, respectively. In this case the loading is negative since adhesion forces on tip oppose to the elastic force of the bent cantilever. The transient frequency analysis allows to retrieve the Q factor of the oscillator by measuring the ratio of the frequency width to the oscillation frequency of the initial high-amplitude damped oscillation. The time-frequency resolution defined by the Heisenberg box dimension of the analyzing wavelet is 0.27 ms $\times$ 1.2 kHz whereas the WT frequency width is of the order of $\Delta f = 2$kHz. Therefore, the frequency width is not limited by the wavelet transform resolution but is associated to the Q factor of the damped oscillator that model the dynamic response of the supported cantilever. With a central frequency of about 60 kHz, the Q factor is obtained as $Q = f/\Delta f$=60kHz/(2kHz)=30. This estimate is quite consistent with the Q factor found using the power spectral density analysis of the stationary cantilever oscillations in contact (see Table 5.1).

The resonant frequency has an evident raise caused by the decrease in the adhesion forces due to cantilever moving towards the surface at constant velocity, a behavior reproducible in all our measurements. The frequency shift is related to the total force (adhesion minus elastic force) that decreases as the cantilever negative deflection approaches the zero value. This transient behavior could not be captured with standard or non-dynamical technihn ques. It is possible to continue the contact mode WT analysis (Fig. 7.3c) increasing the load up to high positive values. Using the wavelet ridges analysis, the time-frequency representation is transformed into a contact-interaction-force vs instantaneous-frequency representation after JTC. Fig. 7.7a shows the ridges analysis of the entire spectroscopy

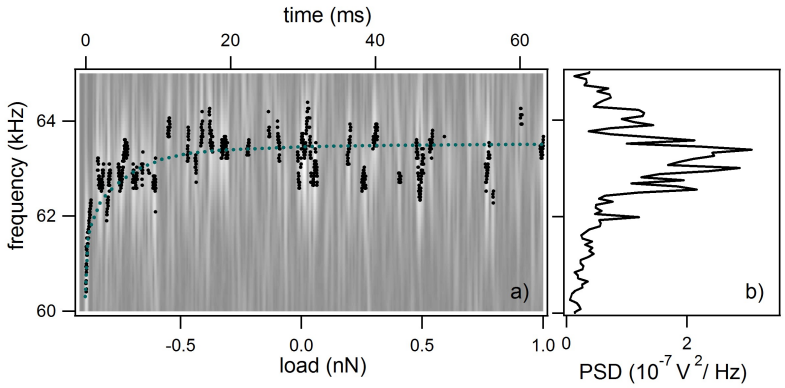

FIGURE 7.7: a) Evolution of the first contact mode resonant frequency as the cantilever moves toward the sample. The wavelet transform is represented on the background in gray scale together with its ridges (black points). The bump immediately after the jump to contact has been rescaled by a factor of 0.2 for graphical reasons. The line is a guide to the eye. b) Power Spectral Density calculated by the same temporal trace used for the wavelet transform in a).

curve. The frequency shift can be followed starting from the very beginning of cantilever interaction with the surface and with good resolution. After the transient at negative loading described above, the cantilever passes through the zero-load neutral point, where it is not deflected, and then continues with increasing positive load on the surface. Traditional frequency domain analysis is not suitable to describe the rapid evolution of the signal spectral content. The same temporal trace used for the wavelet analysis is Fourier transformed giving the PSD in Fig. 7.7b. Only an average of the time dependent frequency spectrum is observed and the instantaneous frequency changes are revealed as an asymmetry in the PSD not useful to extract any information on tip-sample short-range forces. On the contrary, by applying the wavelet analysis the shift of the resonance frequency can be followed starting from the very beginning of cantilever interaction with the surface and with good resolution.

The results reproducibility is demonstrated by repeating the analysis to other two force spectroscopy curves, as shown in Fig. 7.8. There are several analyti-

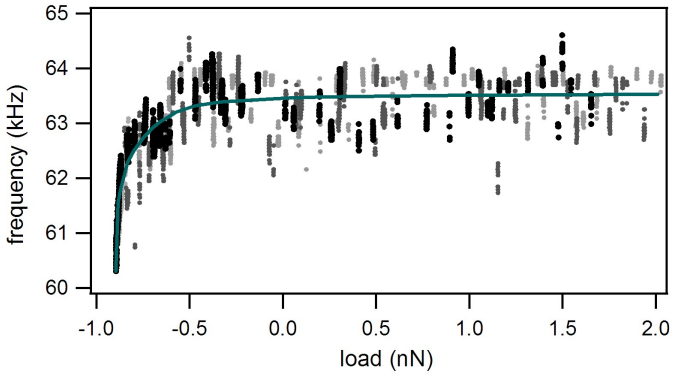

FIGURE 7.8: Instantaneous frequency versus load provided by wavelet ridges analysis. Three different measurements (black, gray and light grey points) are shown to demonstrate reproducibility. The line is a guide to the eye.

cal models [87, 88, 89, 90] and finite element analysis [80] able to quantitatively extract the adhesion forces and/or the elasticity parameters (e.g the Young's modulus) from the spectral response of the cantilever in contact with the surface (Hertz contact dynamics). Applying these models to measure the tip-sample short-range force is the main goal of our work for the future. Finally it is worthwhile to note that the single measure is taken in approximately 100 ms, a time significantly shorter than the usual force spectroscopy techniques probing the short-range interaction 2.6. As a final comment to this section, we stress that the wavelet transform approach could provide quantitative information on the surface elastic properties especially when low force regimes are need, i.e. on softer samples such as biological or polymer surfaces [88].

7.2.3 The oscillator box

Fig. 7.9a-c are the time-frequency representation of the thermal noise signal coming from the AFM photodiode. WT for the three eigenmodes refers to the same time interval i.e. the same trace contains the temporal evolution of all the flexural modes whose oscillation frequencies are below the cutting frequency of the optical lever position detector. WT is performed on the same temporal traces processed

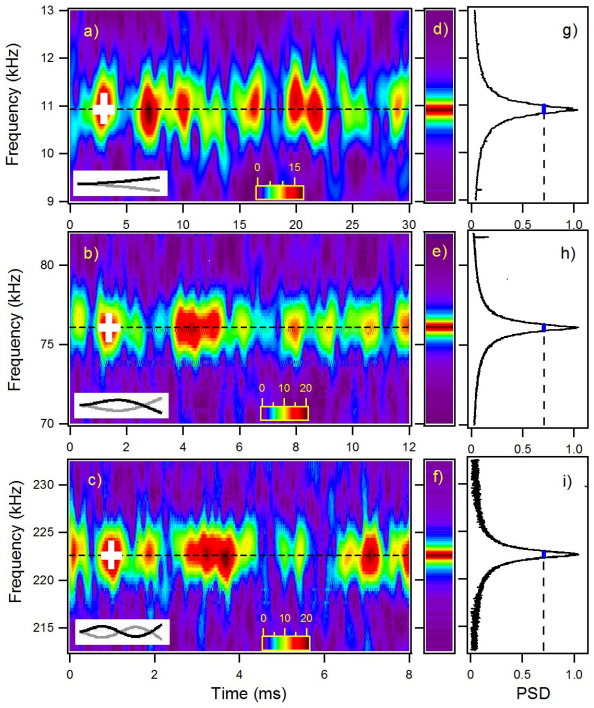

FIGURE 7.9: a)-c) Wavelet transform of the free cantilever thermal vibrations for the three lower flexural eigenmodes. The wavelet coefficients $|Wf(s,t)|$ are coded in colorscale. The horizontal white rectangles represent the damped oscillator boxes, the vertical rectangles the Heisenberg boxes at the respective frequencies. The time range is approximately proportional to the viscous time decay (τ_γ), the frequency range to the power spectral density linewidth. The dashed lines correspond to the resonant frequencies from power spectral density fitting by Lorentzian function. g)-i) Square root of the normalized power spectral density of the free cantilever Brownian motion zoomed on the first three resonant frequency. The blue line is the frequency linewidth $\Delta f = f_0/Q$. The corresponding colorscale plots are displayed in d)-f).

for the PSD calculations but considering a reduced sampling time of a few milliseconds. The Gabor mother wavelets used have G_S= 25, 61, 109, for the first, second and third mode, respectively, so that the time resolution in the Heisenberg box is approximately one eighth of the viscous relaxation time.

The time-frequency representation displays structures centered around the

eigenmode frequencies. The discontinuous appearance of the signal is due to the statistical nature of the cantilever thermal excitation F_{ext}. Microscopically this force can be regarded as the action of random thermal kicks (i.e. uncorrelated impulsive forces), a driving force with white frequency spectrum. This thermal force induces cantilever displacements from the equilibrium position, that show a marked amplitude enhancement in correspondence of the flexural eigenfrequencies. Since the cantilever is subjected also to dissipative friction forces, the amplitude response of the cantilever around a flexural resonant frequency is not delta-like, but has a finite linewidth.

It is interesting to clarify the origin of the "bumps" observed in the time-frequency representation. When the cantilever has a thermally activated fluctuation, each flexural mode responds as a damped harmonic oscillator, see Eq. 3.2 that we rewrite herein:

$$m\ddot{x}(t) + \gamma\dot{x}(t) = -kx(t) + F_{ext}(t) \tag{7.1}$$

Considering for simplicity the initial conditions $x(0) = x_0$, $\dot{x}(0) = 0$ and assuming $Q \gg 1$, the solution is an exponentially decaying amplitude oscillating at the resonance frequency: $x = x_0 e^{-\omega_0 t/(2Q)} cos(\omega_0 t)$. The energy associated to the oscillator $E(t)$ is proportional to $\dot{x}^2$ and from the above relations we see that the associated exponential energy decay time is $\tau = Q/\omega_0$ (viscous relaxation time). The spectral energy density of the damped oscillator ($L(\omega)$) is proportional to the square modulus of the Fourier transform of $x(t)$, $L(\omega) = |\mathrm{FT}(x(t))|^2$. Under the assumption $Q \gg 1$, $L(\omega)$ is well approximated by a Lorentzian with a full width at maximum height of $\Delta\omega = 2\pi\Delta f = 1/\tau$.Since the cantilever is first thermally excited and then damped to steady state by random forces that act on a much smaller time scale than its oscillation period, the characteristic response time for an isolated excitation/decay event cannot be smaller than 2τ, with an associated Lorentzian full width at half maximum of $\Delta\omega$.

From the above reasoning, it is natural to introduce the *damped oscillator box*,

a geometrical representation of the extension in the time-frequency plane of the wavelet coefficients associated to a single excitation/decay event, centered at time t and frequency ω, defined as

$$[t-\tau, t+\tau] \times [\omega - \Delta\omega/2, \omega + \Delta\omega/2]$$

The damped oscillator box, contrary to the Heisenberg box (Sec. 4.4), does not represent a limitation in resolution due to the wavelet choice, but a physical representation of the damped oscillator time-frequency characteristics. It is important to note that the ultimate resolution limitations imposed by the Heisenberg box associated with the analyzing wavelet could prevent the observation of the true dimensions of the damped oscillator box.

Due to their different definitions, a comment on the the sizes of the Heisenberg box and the damped oscillator box is useful. The Heisenberg box dimensions are the root-mean-square extensions of the Gabor wavelet envelope (i.e. its modulus) in time and frequency. Since the Gabor wavelet evelope is a gaussian in time and frequency, its root-mean-square extension is by definition the gaussian standard deviation, i.e. the half width at $1/\sqrt{e} \approx 0.606$ of the maximum. The damped oscillator box dimension in frequency is the full width at half maximum of $L(\omega)$. In terms of the wavelet envelope (proportional to $\sqrt{L(\omega)}$), it is the full width at $1/\sqrt{2} \approx 0.707$ of the maximum. The damped oscillator box dimension in time is 2τ, where τ is the full width at $1/e \approx 0.368$ of the maximum of the exponentially decaying oscillator amplitude. We did not attempt to correct the sizes of the boxes using a single common definition because the comparisons with the experimental data in the present work are mainly qualitative.

In our case the viscous relaxation time provided by f_0 and Q in Tab. 5.1 for the first, second and third eigenmodes is τ =0.93, 0.38, 0.23 ms, respectively. It is important to note that the temporal width of many discrete time-frequency small structures seen in the CWT of the cantilever thermal signal in Fig. 7.9 are of the same temporal dimensions of the damped oscillator box 2τ, corresponding to

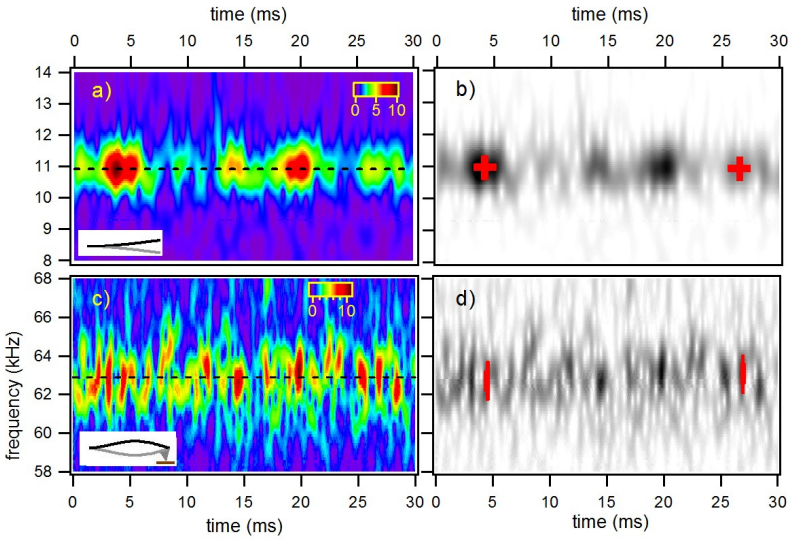

FIGURE 7.10: a-b) Wavelet transform of the free cantilever thermal vibrations for the first flexural eigenmode using a Gabor mother wavelet with shaping factor $G_S = 22$. The wavelet coefficients $|Wf(s,t)|$ are coded in colorscale in a), in gray scale in b). The dashed line is the resonant frequency. The horizontal and vertical red rectangles are the damped oscillator box and the Heisenberg box, respectively. The two boxes are overlapped and compared with the discrete structures in the time-frequency representation. c)-d) Same as a) and b) but for the first contact mode with a tip load of approximately -0.6 nN. The Gabor mother wavelet shaping factor is $G_S = 87$. In d) the vertical red rectangles represent the damped oscillator box. The other rectangles represent the Heisenberg box.

the cantilever excitation and decay to steady state after a single thermal fluctuation event. This can be regard as a representation of the fluctuation-dissipation theorem at the microscopic scale (Sec. 3.2). The observation in time domain is possible because the Heisenberg box has smaller time width than the damped oscillator box. Besides the frequency spread of the bumps is determined by the frequency resolution of the WT i.e. by the frequency dimension of the Heisenberg box which is larger than the damped oscillator frequency linewidth.

Fig. 7.10 compares the wavelet transform of the thermal noise signal for the free cantilever flexural fluctuations and for the cantilever pinned to the surface

(contact mode) with a constant tip load of approximately -0.6 nN (negative load means that the cantilever is bent toward the sample). We choose the first free and first contact modes as model systems with high and low Q factors, respectively, in order to underline how viscous effects are revealed by WT analysis. The tip-sample contact increases dissipation effect which are revealed by comparing the Q factor of eighenmodes with similar oscillation shape (Tab. 5.1). For instance, first flexural contact mode is correctly associated to the second free mode since they display similarity (they have both one node and similar oscillation shape). In this case tip-sample contact dissipation reduces the value of Q by a factor of ten.

A lower Q factor allows to analyze the oscillator dissipation in the frequency domain, by choosing an analyzing wavelet with Heisenberg box (0.31 ms $\times$ 1.0 kHz) whose frequency resolution is lower than the width of the oscillator box (0.16 ms $\times$ 1.9 kHz). Then the frequency spread of the bumps is now defined by the damped oscillator frequency linewidth which is larger than the frequency resolution of the Heisenberg box, while the damping time decay is too short to be analyzed by WT. Since the frequency width of the trace in the time-frequency plane is roughly 2 kHz, the quality factor $Q = f/\Delta f$=63kHz/(2kHz)=31. This value agrees with the analysis made on the high-amplitude transient bump and with the power spectral density analysis (Table 5.1), confirming that the physical oscillator (the cantilever) has the same damped harmonic oscillator dynamics in the various interaction-force regimes after JTC.

The WT analysis of the thermal oscillations of the free and supported cantilever demonstrate how the WT describes more easily a single thermal excitation event time decay in high-Q environments and measures its frequency linewidth in low-Q environments. In both cases, WT allows the instantaneous mapping of energy dissipation effects.

7.3 Torsional modes

The WT analysis can be extended to left-right photodiode signal that describes the torsional oscillation of the cantilever. In torsional modes the cantilever oscillates along its long axis and the tip moves parallel to the surface, see Fig. 5.5. Therefore the probe tip is sensitive to in-plane forces and the eigenfrequency of the torsional modes only depends on the lateral stiffness of the sample. Indeed torsional modes are useful as shear stiffness sensors. An increasing shear stiffness increases the lateral spring constant and consequently the resonant frequency of the system [91]. Moreover, since the torsional modes are stiffer than the flexural modes, a higher quality factor Q and greater sensitivity is obtained. We study the spectra of thermally excited torsional modes of the cantilever as the tip approaches a graphite surface. The left-right photodiode signal is acquired simultaneously to the top-bottom signal exploited to study the flexural modes, we are able to describe the effects of the tip-sample interaction also on the torsional modes.

The wavelet transform of the free thermally excited oscillations of the cantilever detected by the left-rigth sections of the quadrant photodiode shows the evolution in time of the first torsional mode and the lateral mode coupled to a torsional oscillation (see Fig. 7.11). The discontinuous appearance of the traces in the time-frequency plane (the bumps) is due to the intrinsic statistical nature of the thermal excitation, see Sec. 7.2.3. The time-frequency box $2\tau \times \Delta\omega$ represents the damped oscillator box, characteristic of a thermally excited damped oscillator response. When the Q factor of a mode is high, the mechanical resonance is strongly peaked around the resonance frequency, and the corresponding frequency linewidth is small. In this case the frequency resolution of a wavelet may be not sufficient to resolve the intrinsic linewidth of the mechanical resonance. Thus the frequency width of the time-frequency distribution is limited by the wavelet resolution i.e. by the frequency width of the Heisenberg box which is higher than the frequency width of the oscillator box (see Fig. 7.11). On the

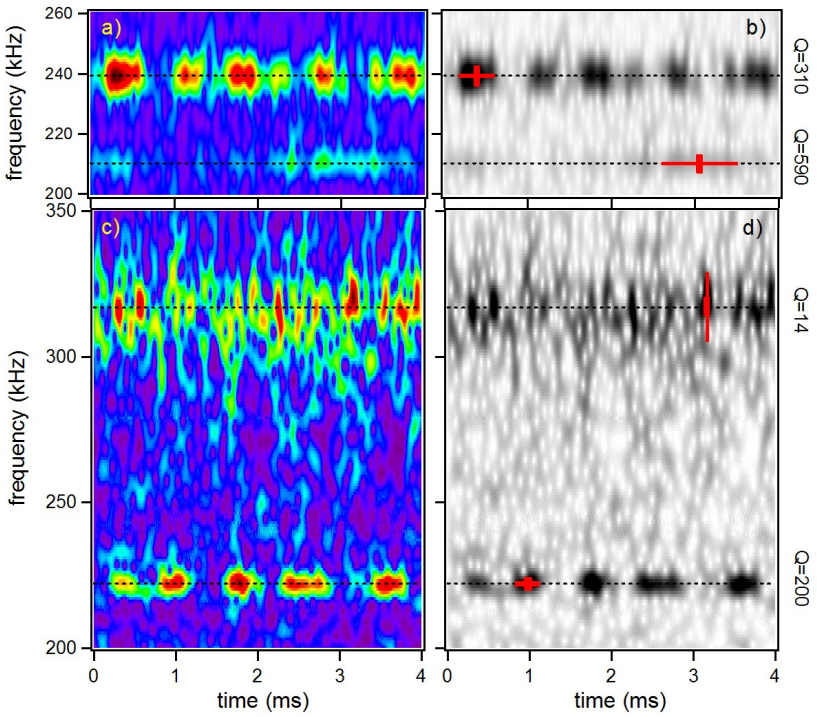

FIGURE 7.11: a)-b) Wavelet transform of the cantilever thermal fluctuations far from the surface, referred to the first lateral (l_1) and first torsional (t_1) mode. The wavelet coefficients $|Wf(s,d)|$ are coded in color scale and gray scale, respectively. In b) the vertical oblong red rectangle represents the damping oscillator box. The horizontal oblong red rectangle represents the Heisenberg box. The two boxes are overlapped to appreciate the comparison with the features in the time-frequency representation. c) - d) same as a) - b) but with the tip in contact with the surface, at constant positive load of approximately 1.6 nN.

other hand, a high Q implies a long decay time associated to the oscillator energy. In this case the time associated to the damped oscillator box is larger than the temporal wavelet resolution, i.e. the time width of the oscillator box is larger than the time width of the Heisemberg box. In Fig. 7.11 the oscillator box and the Heisemberg box, represented as red boxes, have been superposed on the time-

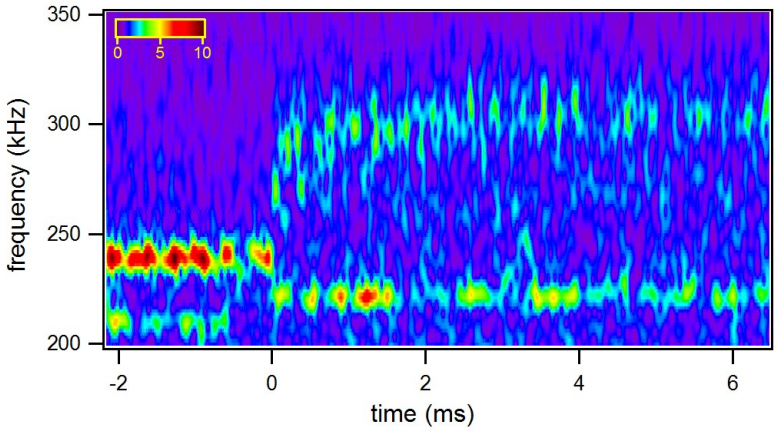

FIGURE 7.12: Wavelet transform of the cantilever thermal torsional oscillation across the jump-to-contact transition, showing the evolution of the first torsional and lateral resonance frequency. The wavelet coefficients $|Wf(s,d)|$ are coded in color scale. The origin of the time axis is at the jump-to-contact onset. Both modes have an evident shift as the tip is attracted on the surface.

frequency representation of the wavelet coefficients. On the basis of the precedent discussion, the size of the thermally activated fluctuations in time or frequency are, in a statistical sense, comparable to that of the bigger dimension between the two boxes (Heisenberg box, frequency width; oscillator box, time width). Such structures can be interpreted as the cantilever excitation and decay to steady state after a single thermal fluctuation event. Across the JTC transition the Q factor of the first torsional mode decreases rapidly and the oscillator box re-shapes accordingly, reducing the damping time of the oscillator and increasing its frequency bandwidth (Fig. 7.11d). In this case, the frequency resolution of the wavelet is sufficient to reconstruct the linewidth profile of the time-frequency trace since the Heisenberg box frequency dimension is smaller than the frequency width of the oscillator box. Nevertheless, now the time resolution of the wavelet does not allow to follow the evolution of the activated thermal events, because the time width of the oscillator box is smaller than the corresponding Heisenberg box dimension. The torsional resonance shift can be followed through the JTC transition with the

wavelet transforms. The JTC transition is conventionally located at time zero, separating the negative times of the free cantilever evolution, from the positive times of the clamped cantilever evolution. In Fig. 7.12 the increase of the torsional frequency oscillation and that of the lateral mode across the JTC transition are shown. The lateral mode frequency immediately after JTC is fairly constant but higher than that of the free cantilever. Instead, the torsional mode shows an increasing frequency after JTC (that evolves in a time interval of the order of 10μs) during several ms. The frequency evolution is provided by the wavelet ridges that show the instantaneous frequencies within the transform resolution limits [61]. The time axis of the time-frequency representation has a different meaning before and after JTC. Before JTC the time is connected to the tip displacement towards the surface. Taking into account both the scanner piezo vertical velocity and the static deflection, it is possible to map time to tip-sample distance. Immediately after JTC the force acting on the cantilever is negative (negative loading). In this case the tip is acted on by adhesion forces that attracts the tip towards the surface. The piezo displacement is connected with the contact interaction force between the tip and the surface. In this case it is possible to map the time to contact interaction force (as shown in Fig. 7.13). Using the wavelet ridges, the time-frequency representation is thus transformed into a contact-interaction-force vs frequency shift representation after JTC. The frequency shift is thus caused by the decrease in strength of adhesion forces, a transient that could not be captured with standard or non-dynamical techniques. With a suitable model this technique could allow to measure the properties of adhesion forces in detail [80, 32, 87].

7.4 Summary

We applied wavelet transform analysis to the thermal oscillations of a free cantilever and to an interacting cantilever with a graphite surface. Both flexural and torsional modes are analyzed. The time-frequency representation shows the

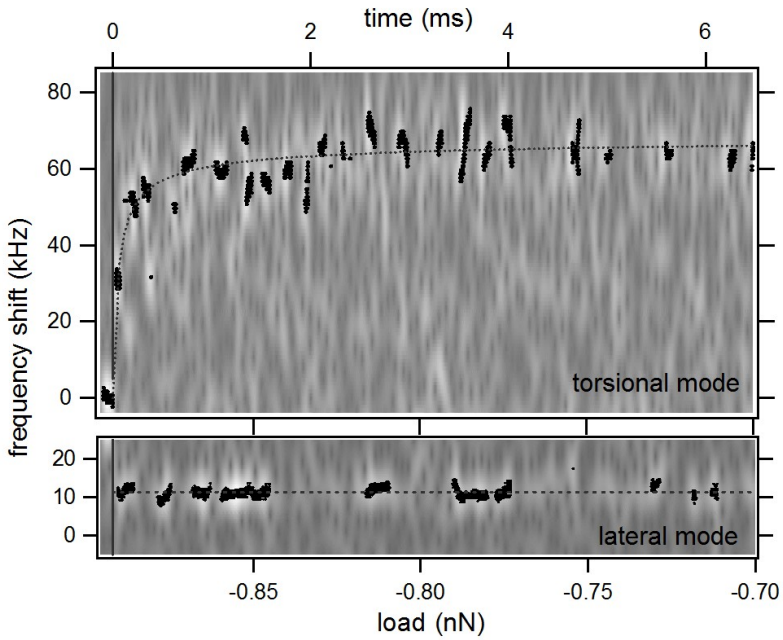

FIGURE 7.13: a) Frequency shift of the first torsional mode versus the tip load. The wavelet ridges (black points) provide the instantaneous frequency within the limit of the scalogram resolution. The wavelet in Fig. 7.12 is represented in gray scale on the background. The continuous vertical line corresponds to the jump-to-contact onset. The dashed horizontal line is a guide to the eye. b) Same as a) for the lower lateral mode. The dashed line is the contact resonance frequency.

viscous dynamics of the cantilever deflection activated by thermal fluctuations. The wavelet transform is able to analyze the instantaneous spectral content of a rapidly varying signal such as the response of a thermally excited cantilever to the tip interaction with the sample surface. The wavelet transform technique is a very promising tool to probe the tip sample interaction since the analysis applies simultaneously to the flexural and torsional eigenmodes and the analyses are carried out across the JTC transition without interruption. The measure is taken in approximately 100 ms. With an optimization of the electronics and reduction of dead times in the detection process, it would be possible to acquire images in which a complete information on force gradients, adhesion forces, elastic response

and topography is compatible with data acquisition times required for practical DFS imaging.

Chapter 8

Conclusions and perspectives

In this thesis, we study the dynamic response of an atomic force microscopy cantilever thermally driven in order to probe short- and long-range interaction forces between the tip and the graphite sample surface. We made use of two different approaches.

In stationary regime the cantilever thermal fluctuations are analyzed by applying three different methods, frequency shift, Boltzmann distribution of the Brownian motion and thermal mean square displacement methods. This allows to estimate the non retarded van der Waals interaction force and to discuss the tip mass loading effect on the cantilever elastic behavior. The main limitation of the stationary regime analysis is that it requires long acquisition time.

An improvement of the experimental conditions and data analysis is provided by the wavelet transform approach (dynamic regime, Chapter 7). The time-frequency representation of wavelet analysis shows the viscous dynamics of the cantilever deflection activated by thermal fluctuations. The wavelet transform analysis performed when the tip is near the sample surface allows to quantitative measure tip-sample van der Waals interaction force and to estimate the Hamaker constant. The wavelet analysis of the cantilever fluctuations in contact with the surface provides qualitative information on adhesion forces, friction and elastic re-

sponse. The measurement is performed in short acquisition times.

The main perspective of this work is to apply suitable analytical models [87, 88, 89, 90] or finite element analysis [80] to quantitatively extract the adhesion forces and/or the elasticity parameters (e.g the Young's modulus) from the spectral response of the cantilever in contact (Hertz contact dynamics). In the present work we choose a graphite sample to test the validity of the technique in measuring short-range force. In the future the wavelet analysis will be applied to characterize friction and elastic response of both organic and inorganic materials.

Here we exploited only the amplitude of the complex wavelet transform. Nevertheless, information on other properties such as viscoelasticity could be extract by studying the evolution of the phase [6] provided by the wavelet transform coefficients.

The technique can be improved by driving the cantilever motion with impulsive broad band excitation [37]. The wavelet analysis would provide the full spectral response of the interacting cantilever reducing the acquisition time required to reconstruct force-distance spectroscopy. Moreover the dissipation energy could be simultaneously measured by estimating the Q-factor of the cantilever-sample system.

The wavelet transform analysis could be adopted in AFM dynamic force spectroscopy performed in all cases where a rapid quantitative measurement of the spectral evolution of the system is needed. In order to apply the wavelet transform to real time analysis, the data processing has to be sped up. The goal can be reached by using discrete wavelet transform (DWT) instead of continuous wavelet transform (CWT). DWT adopts an orthonormal set of basis atoms which eliminates redundant calculations due to non orthogonality of the CWT basis [61, 67]. Thus signals could be processed in times as short as required by on-line measurements.

Bibliography

[1] G. Binnig, H. Rohrer, C. Gerber, and E. Weibel, Phys. Rev. Lett. **49**, 57 (1982).

[2] G. Binnig, C. Gerber, and C. Quate, Phys. Rev. Lett. **56**, 930 (1986).

[3] K. D. Jandt, Surf. Sci. **491**, 303 (2001).

[4] P. C. Braga and D. Ricci, *Atomic Force Microscopy: Biomedical Methods and Applications (Methods in Molecular Biology)* (Humana Press, Totowa, NJ, 2004).

[5] B. P. Jena and J. K. H. Hörber, *Atomic Force Microscopy in Cell Biology (Methods in Cell Biology, vol. 68)* (Academic Press, San Diego (CA), London (UK), 2002).

[6] R. Garcia and R. Perez, Surf. Sci. Rep. **47**, 197 (2002).

[7] A. Yacoot and L. Koenders, J. Phys. D: Appl. Phys. **41**, 103001 (2008).

[8] F. J. Giessibl, Rev. Mod. Phys. **75**, 949 (2003).

[9] J. Kopniczky, *Nanostructures Studied by Atomic Force Microscopy* (Acta Universitatis Upsaliensis, Uppsala, Sweden, 2003).

[10] H. J. Butt, B. Cappell, and M. Kappl, Surf. Sci. Rep. **59**, 1 (2005).

[11] Y. Martin, C. C. Williams, and H. K. Wickramasinghe, J. Appl. Phys. **61**, 4723 (1987).

[12] The dynamic of the oscillating tip is analyzed in detail in Chap. 3. A complete analysis can be found in [6, 40].

[13] R. W. Stark, N. Naujoks, and A. Stemmer, Nanotechnology **18**, 065502 (2007).

[14] J. R. Lozano and R. Garcia, Phys. Rev. Lett. **100**, 076102 (2008).

[15] T. R. Albrecht, P. Grütter, D. Horne, and D. Rugar, J. Appl. Phys. **69**, 668 (1991).

[16] S. Morita, R. Wiesendanger, and E. Meyer, *Noncontact Atomic Force Microscopy* (Springer, Berlin, 2002).

[17] F. J. Giessibl and G. Binnig, Ultramicroscopy **42-44**, 281 (1992).

[18] R. Erlandsson, L. Olsson, and P. Martensson, Phys. Rev. B **54**, (1997).

[19] F. J. Giessibl, S. Hembacher, H. Bielefeld, and J. Mannhart, Science **289**, 422 (2000).

[20] A. S. Paulo and R. Garcia, Biophysical J. **78**, 1599 (2000).

[21] S. Patil, N. F. Martinez, J. R. Lozano, and R. Garcia, J. Mol. Recognit. **20**, 516 (2007).

[22] F. J. Giessibl, Science **267**, 68 (1995).

[23] Y. Sugawara, M. Otha, H. Ueyama, and S. Morita, Science **270**, 1646 (1995).

[24] Y. Sugimoto, P. Pou, M. Abe, P. Jelinek, R. Pérez, S. Morita, and O. Custance, Nature **446**, 05530 (2007).

[25] L. Gross, F. Mohn, N. Moll, P. Liljeroth, and G. Meyer, Science **325**, 1110 (2009).

[26] J. L. Hutter, Langmuir **21**, 2630 (2005).

[27] S. Das, P. A. Sreeram, and A. K. Raychaudhuri, Nanotechnology **18**, 035501 (2007).

[28] G. Palasantzas, P. J. van Zwol, and J. T. M. D. Hosson, Appl. Phys. Lett. **93**, 121912 (2008).

[29] Sugimoto, S. Innami, M. Abe, O. Custance, and S. Morita, apl **91**, 093120 (2007).

[30] E. Palacios-Lidón and J. Colchero, nt **17**, 5491 (2006).

[31] M. A. Lantz, H. J. Hug, R. Hoffmann, P. J. A. van Schendel, P. Kappenberger, S. Martin, A. Baratoff, and H. J. Güntherodt, Science **291**, 2580 (2001).

[32] M. Stark, R. W. Stark, W. M. Heckle, and R. Guckenberger, Proc. Natl. Acad. Sci. U S A **99**, 8473 (2002).

[33] S. Crittenden, A. Raman, and R. Reifenberger, Phys. Rev. B **72**, 235422 (2005).

[34] H. Hölsher, W. Allers, U. D. Schwarz, A. Schwarz, and R. Wiesendanger, prl **83**, 4780 (1999).

[35] A. Schirmeisen, D. Weiner, and H. Fuchs, Phys. Rev. Lett. **97**, 136101 (2006).

[36] M. Abe, Y. Sugimoto, T. Namikawa, K. Morita, N. Oyabu, and S. Morita, Appl. Phys. Lett. **90**, 203103 (2007).

[37] S. Jesse, S. V. Kalinin, R. Proksch, A. P. Baddorf, and B. J. Rodriguez, Nanotechnology **18**, 435503 (2007).

[38] A. Roters and D. Johannsmann, J. Phys.: Condens. Matter **8**, 7561 (1996).

[39] G. Malegori and G. Ferrini, J. Vac. Sci. Technol. B **28**, (2010).

[40] V. L. Mironov, *Fundamentals of scanning probe microscopy* (The Russian Academy of Sciences, Nizhniy Novgorod, Russia, 2004).

[41] H. Butt and M. Jaschke, Nanotechnology **6**, 1 (1995).

[42] P. Paolino, B. Tiribilli, and L. Bellon, J. Appl. Phys. **106**, 094313 (2009).

[43] H. B. Callen and R. F. Greene, Phys. Rev. **86**, 702 (1952).

[44] D. T. Gillespie, Am. J. Phys. **61**, 1077 (1993).

[45] Here we use two sided power spectrum density functions of frequency f, such that $\langle x^2 \rangle = \int_{-\infty}^{+\infty} S_x(f) df$. Comparison to experiment requires the one side power spectral density function provided by $2S_x(f)$. Instead, the response functions G is given as a function of the pulsation ω.

[46] P. Paolino and L. Bellon, Nanotechnology **20**, 405705 (2009).

[47] M. Shusteff, T. P. Burg, and S. R. Manalisa, Am. J. Phys. **74**, 873 (2006).

[48] D. T. Gillespie, Am. J. Phys. **64**, 225 (1996).

[49] P. Paolino *Bruit thermique et dissipation d'un microlevier*, PhD Thesis, École Normale Supérieure de Lyon, France 2008.

[50] R. Lévy and M. Maaloum, Nanotechnology **13**, 33 (2002).

[51] D. T. Giessibl, Phys. Rev. B **56**, 16010 (1997).

[52] M. Luna, J. Colchero, and A. M. Barò, J. Phys. Chem. B **103**, 9576 (1999).

[53] J. Colchero, A. Storch, M. Luna, J. G. Herrero, and M. Baró, Langmuir **14**, 2230 (1998).

[54] H. C. Hamaker, Physica (Amsterdam) **4**, 1058 (1937).

[55] J. Israelachvili, *Intermolecular and Surface Forces* (Academic Press, London, 1991).

[56] B. Cappella and G. Dietler, Surf. Sci. Rep. **34**, 1 (1999).

[57] R. H. French, J. Am. Ceram. Soc. **83**, 2117 (2000).

[58] J. M. Fernández-Verea and R. Garcia-Molina, J. Colloid Interface Sci. **179**, 637 (1996).

[59] E. Sahagún, P. Garcia-Mochales, G. M. Sacha, and J. J. Sáenz, Phys. Rev. Lett. **98**, 176106 (2007).

[60] C. K. Chui, *An Introduction to Wavelets* (Academic Press, London, 1992).

[61] S. G. Mallat, *A Wavelet Tour of Signal Processing* (Academic Press, San Diego, CA, 1999).

[62] T. Torrence and G. Compo, Bull. Am. Meteorological Soc. **79**, 61 (1998).

[63] Y. Deng, C. Wang, L. Chai, and Z. Zhang, App. Phys. B **81**, 1107 (2005).

[64] Image credit: André Mouraux, Faculté de Médecine, Univ. Catholique de Louvain, Belgium.

[65] J. C. Hong and Y. Y. Kim, Exp. Mechanics **44**, 387 (2004).

[66] Y. Deng, W. Yang, C. Zhou, X. Wang, J. Tao, W. Kong, and Z. Zhang, **17**, 6038 (2009).

[67] A. L. Graps, IEEE Computational Science and Engineering **2**, 50 (1995).

[68] M. Carmichael, R. Vidu, A. Maksumov, A. Palazoglu, and P. Stroeve, Langmuir **20**, 11557 (2004).

[69] C. Gackenheimer, L. Cayon, and R. Reifenberger, Ultramicroscopy **106**, 389 (2009).

[70] C. Junsheng, Y. Dejie, and Y. Yu, NDT & E International **38**, 569 (2005).

[71] D. Reolon, M. Jacquot, I. Verrier, G. Brun, and C. Veillas, Optics Express **14**, 12744 (2006).

[72] A.P.E. Research Trieste www.aperesearch.com.

[73] PicoScope 5204 www.picotech.com.

[74] $\mu-$masch series CSC17, www.spmtips.com.

[75] J. E. Sader, Rev. Sci. Instrum. **70**, 3967 (1999).

[76] www.ampc.ms.unimelb.edu.au/afm/index.html.

[77] www.mathworks.com.

[78] N. A. Burnham, X. Chen, C. S. Hodges, G. A. Matei, E. J. Thoreson, C. J. Roberts, M. C. Davies, and S. J. B. Tendler, Nanotechnology **14**, 1 (2003).

[79] J. L. Hutter and J. Bechhoefer, Rev. Sci. Instrum. **64**, 1868 (1993).

[80] F. J. Espinosa-Beltrán, K. Geng, J. M. M. noz Saladaña, U. Rabe, S. Hirsekorn, and W. Arnold, New J. Phys. **11**, 083034 (2009).

[81] M. Reinstaedtler, U. Rabe, V. Scherer, J. A. Turner, and W. Arnold, Surf. Sci **532-535**, 1152 (2003).

[82] C. P. Green, H. Lioe, J. P. Cleveland, R. Proksch, P. Mulvaney, and J. E. Sader, Rev. Sci. Instrum. **75**, 1988 (2004).

[83] http://www-stat.stanford.edu/∼wavelab.

[84] A. Siria, A. Drezet, F. Marchi, F. Comin, S. Huant, and J. Chevrier, Phys. Rev. Lett. **102**, 254503 (2009).

[85] J. Melcher, Appl. Phys. Lett. **91**, 053101 (2007).

[86] W. F. Heinz, M. D. Antonik, and J. H. Hoh, J. Phys. Chem. B **104**, 622 (2000).

[87] K. Yamanaka and S. Nakano, Appl. Phys. A **66**, (1998).

[88] U. Rabe, K. Janser, and W. Arnold, Rev. Sci. Instrum. **67**, 3281 (1996).

[89] E. Dupas, G. Gremaud, A. Kulik, and J. Loubet, Rev. Sci. Instrum. **72**, 3891 (2001).

[90] P. Vairac, B. Cretin, and A. J. Kulik, Appl. Phys. Lett. **83**, 3824 (2003).

[91] T. Drobek, R. W. Stark, M. Gräber, and W. M. Heckl, New J. Phys. **1**, 15 (1999).

List of publications

Tip-sample interactions on graphite studied in the thermal oscillation regime

G. Malegori and G. Ferrini, *J. Vac. Sci. Technol. B* 28, C4B18 (2010)

Cantilever thermal uctuations in contact mode analyzed by the wavelet transform: preliminary results

G. Malegori and G. Ferrini, *Beilstein J. Nanotechnol.*(accepted)

Wavelet transforms and thermally excited cantilevers near the jump-to-contact transition: preliminary results

G. Malegori and G. Ferrini, *e-J. Surf. Sci. Nanotechnol.* (submitted)

Cantilever thermal fluctuations in contact mode analyzed by the wavelet transform: preliminary results

G. Malegori and G. Ferrini, *Meas. Sci. Technol.* (submitted)

Wavelet transform to probe long and short-range forces in graphite by thermally excited dynamical force spectroscopy

G. Malegori and G. Ferrini, *Nanotechnol.* (submitted)

Conferences

Oral presentation: N. Andreeva, G. Ferrini, V. Spreafico, S. Prato and *G. Malegori**

Developments of combined scanning near-field optical microscopy and atomic force microscopy applied to biological system,

International School of Biophysics - Multidimensional Optical Fluorescence Microscopy towards Nanoscopy, "Ettore Majorana" Foundation and Center for Scientific Culture, Erice (Italy) April 19-27, 2008

Poster contribution: Giovanna Malegori and *Gabriele Ferrini**,

Resonance frequency shift due to tip-sample interaction in the thermal oscillations regime, 12th International Conference on Noncontact Atomic Force Microscopy, NC-AFM 2009, Yale University, New Haven (USA), August 10-14, 2009.

Oral presentation: *Giovanna Malegori** and Gabriele Ferrini,

Resonance frequency shift due to tip-sample interaction in the thermal oscillations regime, European Conference on Surface Science ECOSS26, Parma (I) August 30 - September 04, 2009

Oral presentation: Giovanna Malegori and *Gabriele Ferrini**,

Resonance frequency shift due to tip-sample interaction in the thermal oscillation regime, Energy Dissipation In NAnocontacts and Molecular bonds, EDINAM 09 - Dresden (D), September 28 - October 1, 2009.

Poster contribution: Giovanna Malegori and *Gabriele Ferrini**,

Frequency shift in the thermal oscillation regime to retrieve force-

distance curves in graphite, International Workshop on Advanced Atomic Force Microscopy Techniques - Karlsruhe (D), March 1-2, 2010.

ORAL PRESENTATION: *Giovanna Malegori** and Gabriele Ferrini,
Tip-sample interaction on graphite studied in the thermal oscillations regime, Forum de Microscopies á sonde locale Forum 2010, Mittelwihr (F) March 15-18, 2010

ORAL PRESENTATION: Giovanna Malegori and *Gabriele Ferrini**,
Visualizing the jump-to-contact transition to describe the tip-sample energy exchange, 1st European Nanomanipulation Workshop - Cascais (P), May 17-19, 2010.

ORAL PRESENTATION: Giovanna Malegori and *Gabriele Ferrini**,
Force mapping and quantitative elasticity evaluation using the Brownian Motion of an AFM tip, 13th International Conference on Non-Contact Atomic Force Microscopy- NC-AFM 2010, Kanazawa (J), July 31- August 5, 2010

POSTER CONTRIBUTION: *Giovanna Malegori** and Gabriele Ferrini
Force mapping and quantitative elasticity evaluation using the Brownian Motion of an AFM tip, European Conference on Surface Science ECOSS 27, Groningen (NL) August 29- September 3, 2010

POSTER CONTRIBUTION: *G. Malegori**, V. Spreafico, S. Prato and G. Ferrini,
Measuring the tip-sample interaction on graphite in the thermal oscillations regime, Nanoscale 2010 (9th Seminar on Quantitative Microscopy (QM) and 5th Seminar on Nanoscale Calibration Standards and Methods), Brno (CZ) October 27-29, 2010

Oral presentation: *Giovanna Malegori** and Gabriele Ferrini,

Force mapping and elasticity evaluation by wavelet analysis of the AFM tip Brownian motion, Nanoscale 2010 (9th Seminar on Quantitative Microscopy (QM) and 5th Seminar on Nanoscale Calibration Standards and Methods), Brno (CZ) October 27-29, 2010.

Acknowledgments

This thesis is the outcome of a wonderful three years experience, and I wish to conclude with a few acknowledgments. I am grateful to Prof. Gabriele Ferrini, who has been great supervisors for this thesis work and who made this experience possible. I thank him for his help and advices. He was able to effectively support and encourage me on scientific and psychologic issues. It was really a pleasure to collaborate with him.

I want to acknowledge all the people who gave me scientific support, with their experience and interests in the subject. I thank Prof. Massimiliano Labardi for his comments and for his help as referee in the review process. I also acknowledge Vittorio Spreafico and Stefano Prato for technical support in setting-up the experiment. A huge thanks goes to Natalia Andreeva for her friendship and scientific advices. I wish to thank Prof. Alessandro Podestá for useful suggestions during planning the present research work. A particular thanks goes to Emanuele Cavaliere and Damiano Nardi, always available to help and support me with software issues.

Finally, I thank all the people who made my staying at the Universitá Cattolica a wonderful experience: Natalia Andreeva, Francesco Banfi, Luca Bignardi, Davide Bossini, Patrizia Borghetti, Emanuele Cavaliere, Luca Celardi, Federico Cilento, Stefano Dal Conte, Giovanni Drera, Gianluca Galimberti, Claudio Giannetti, Matteo Montagnese, Damiano Nardi, Stefania Pagliara, Stefano Ponzoni, Marco Travagliati. La vostra naturalezza e spontaneitá hanno colmato il divario generazionale che ci separa facendo sí che la mia vita di tutti i giorni in universitá, in ufficio, in mensa fosse straodinariamente piacevole.

A Massimo, Luca, Stefano e Guido devo piú di ogni altra cosa. Le parole non sono sufficienti per descrivere la forza e la serenitá che la vostra presenza mi trasmette.